SLAC-R-809

Principles of X-ray Navigation

John Eric Hanson

Stanford Linear Accelerator Center
Stanford University
Stanford, CA 94309

SLAC-Report-809

Prepared for the Department of Energy
under contract number DE-AC02-76SF00515

Printed in the United States of America. Available from the National Technical Information Service, U.S. Department of Commerce, 5285 Port Royal Road, Springfield, VA 22161.

SLAC-R-809

Principles of X-ray Navigation

John Eric Hanson

Stanford Linear Accelerator Center
Stanford University
Stanford, CA 94309

SLAC-Report-809

Prepared for the Department of Energy
under contract number DE-AC02-76SF00515

Printed in the United States of America. Available from the National Technical Information Service, U.S. Department of Commerce, 5285 Port Royal Road, Springfield, VA 22161.

PRINCIPLES OF X-RAY NAVIGATION

A DISSERTATION SUBMITTED TO THE
DEPARTMENT OF AERONAUTICS AND ASTRONAUTICS
AND THE COMMITTEE ON GRADUATE STUDIES
OF STANFORD UNIVERSITY
IN PARTIAL FULFILLMENT OF THE REQUIREMENTS
FOR THE DEGREE OF
DOCTOR OF PHILOSOPHY

By
John Eric Hanson
March, 1996

Abstract

X-ray navigation is a new concept in satellite navigation in which orientation, position and time are measured by observing stellar emissions in x-ray wavelengths. X-ray navigation offers the opportunity for a single instrument to be used to measure these parameters autonomously. Furthermore, this concept is not limited to missions in close proximity to the earth. X-ray navigation can be used on a variety of missions from satellites in low earth orbit to spacecraft on interplanetary missions.

In 1997 the Unconventional Stellar Aspect Experiment (USA) will be launched as part of the Advanced Research and Global Observation Satellite (ARGOS). USA will provide the first platform for real-time experimentation in the field of x-ray navigation and also serves as an excellent case study for the design and manufacturing of space qualified systems in small, autonomous groups.

Current techniques for determining the orientation of a satellite rely on observations of the earth, sun and stars in infrared, visible or ultraviolet wavelengths. It is possible to use x-ray imaging devices to provide arcsecond level measurement of attitude based on star patterns in the x-ray sky. This technique is explored with a simple simulation.

Collimated x-ray detectors can be used on spinning satellites to provide a cheap and reliable measure of orientation. This is demonstrated using observations of the Crab Pulsar taken by the High Energy Astronomy Observatory (HEAO-1) in 1977. A single instrument concept is shown to be effective, but dependent on an a priori estimate of the guide star intensity and thus susceptible to errors in that estimate. A star scanner based on a differential measurement from two x-ray detectors eliminates the need for an a priori estimate of the guide star intensity. A first order model and a second order model of the two star scanner concepts are considered.

Many of the stars that emit in the x-ray regime are also x-ray pulsars with frequency stability approaching a part in 10^9. By observing these pulsations, a satellite can keep accurate time autonomously. We have demonstrated the acquisition and tracking of the Crab nebula pulsar by simulating the operation of a phase-locked loop.

Acknowledgments

As I put the finishing touches on this dissertation, I should take a moment to thank the myriad of people who have made this possible.

First, I would like to thank my two advisors, Professor Dan DeBra and Professor Elliott Bloom, for their guidance and understanding during my stay here. I have been fortunate to work with both of their groups simultaneously and have learned more about engineering in the past three years than I ever thought possible. I thank Chris Lages and Han Wen both for their friendship and for the endless and far ranging discussions - some about work and some not.

I want to thank Professor Steve Rock for serving on my oral committee and my reading committee with Professor DeBra and Professor Bloom, and Professor Peter Michelson for chairing my oral committee. Their insights and suggestions have improved this work immeasurably.

I want to thank all of the members of the USA team for their friendship and help these past three years - Gary, John, Andrew and Linda Lee. I have enjoyed working with the entire USA team (SLAC and NRL contingents) immensely. The USA experiment and this thesis certainly would not have been possible without the tireless efforts of Dr. Kent Wood and Dr. Michael Lovellette and to them both I am grateful. I also want to thank Dr. Wood for allowing me to base this thesis on some of his original ideas for x-ray navigation.

Much of this dissertation is made possible by the availability of data from the HEAO-A1 mission. This has been maintained by Dr. Lynn Cominsky, Han Wen and Andrew Lee. I thank them all for their help in both getting the data I needed and in understanding it.

I would like to thank my parents, Jack and Judy Hanson, and my sisters Lori and Lisa for their support and encouragement over the past six years. Contrary to popular belief, life at Stanford is not always beautiful weather and wonderful scenery. It helps to

have family and friends close by to take the edge off. To this end, I have been blessed with many old and new friends from the east coast to the west coast. Darren, Audrey and Kara have kept me generally sane, moderately cultured and occasionally well fed. Mark, Rob, Ed, Theresa, Jerry and Steve added much needed humor with every e-mail and were there for some of our less cultured (but nonetheless important) endeavors.

And last, but certainly not least, I want to thank all of the new friends I have made at Stanford (the aforementioned Chris, and the here-mentioned Bob, Steve, Phil, Ed and Susan) for a wonderful six years.

Table of Contents

List of Figures

List of Tables

List of Abbreviations

ADACS	Attitude Determination and Control System
ADB	Aluminum Dip Braze Corporation
ARGOS	Advanced Research and Global Observation Satellite
CAD	Computer Aided Design
CAEDS	Computer Aided Engineering and Design Software
CE Box	Central Electronics Box
CXE	Cosmic X-ray Experiment
FEM	Finite Element Model
FOS	Factor of Safety
FOV	Field of View
GP-A	Gravity Probe A
GPS	Global Positioning System
HEAO-1	High Energy Astronomical Observatory 1
HEAO-A1	High Energy Astronomical Observatory 1, Experiment A
ICD	Interface Control Document
IDL	Interactive Data Language
LASS	Large Area Sky Survey
LEO	Low Earth Orbit
MC	Modulation Collimator
Mod 3	Module 3 of HEAO-A1
Mod 5	Module 5 of HEAO-A1
MOS	Margin of Safety
NRL	Naval Research Laboratory
OSO-3	Orbiting Solar Observatory 3
PLL	Phase Locked Loop

SIXI	Silicon Imaging X-ray Instrument
SLAC	Stanford Linear Accelerator Center
SNR	Signal to Noise Ratio
USA	Unconventional Stellar Aspect Experiment
VCO	Voltage Controlled Oscillator

List of Symbols

Pointing Feasibility Study

t_0	time of initial attitude estimate
t_1	time of updated attitude estimate
Δt	x-ray star mapper sample period
t_e	x-ray star mapper exposure time
X	number of photons from bin containing x-ray background
Y_i	number of photons from bin containing x-ray guide star
μ_s	mean guide star count rate (counts/sec*m2)
A	instrument effective collecting area
P(S)	probability of successful attitude update
μ_b	mean background count rate (counts/sec*m2)

X-ray Star Scanners - Instrument Fundamentals

α	x-ray photon angle of incidence - one dimensional
L_0	geometric length of detector
L	effective length of detector
T_c	collimator transmission
α_0	collimator half-cone angle - one dimensional
h_0	collimator height
ρ	x-ray photon angle of incidence - two dimensional
ρ_0	collimator half-cone angle - two dimensional

X-ray Star Scanner Models

(X_c, Y_c, Z_c)	celestial coordinate system basis
RA	right ascension of guide star in celestial coordinates
DEC	declination of guide star in celestial coordinates
(X, Y, Z)	guide star coordinate system basis

(x, y, z)	spacecraft body coordinate system basis
$(\delta_x, \delta_y, \delta_z)$	instrument in spacecraft body frame (body123 rotation)
$\hat{R}_S$	spacecraft to guide star unit vector
(x_i, y_i, z_i)	instrument coordinate system basis
(T_x, T_y, T_z)	external torques in body frame
$(\omega_x, \omega_y, \omega_z)$	angular velocity in body frame
$(\dot{\omega}_x, \dot{\omega}_y, \dot{\omega}_z)$	angular acceleration in body frame
(I_{xx}, I_{yy}, I_{zz})	principal moments of inertia
Ω	spin rate about axis of maximum moment of inertia
t	time
$\theta(0)$	pitch angle
B_i	background photons in bin i
R	guide star intensity
t_i	time at center of bin i
A	instrument geometric area
$(\varepsilon_x, \varepsilon_y, \varepsilon_z)$	misalignment of instrument (body123 rotation)
(ψ, θ, ϕ)	spacecraft body in guide star coordinates (body213 rotation)
$\dot{\theta}(0)$	nutation rate

X-ray Star Scanners - Differential Detectors

S	instrument signal
N	instrument noise
B	background intensity
ρ_0	instrument half cone angle in roll
A	instrument geometric area
R	guide star intensity
l	collimator packing factor

HEAO Data and Model Fitting

C_{jr}	raw counts from module j
C_j	counts from module j corrected for instrument dead time
τ_d	dead time
τ_b	bin size
Y_{ji}	model counts in bin i, module j
B_{ji}	model background counts in bin i, module j
T_{ji}	collimator transmission in bin i, module j
B_{j0}, B_{jf}	linear background fit, module j
B_{j0}, B_{jf}	linear background fit, module j
B_{ji}	model background counts in bin i, module j
R	model guide star intensity
N	number of bins in scan
i	bin number
$T_{\alpha i}$	transmission in pitch at bin i
$T_{\rho i}$	transmission in roll at bin i
t_i	time at center of bin i
i_p	model bin number where roll angle is zero
μ	total intensity
δ_{jx}	collimator pitch offset, module j
δ_{jz}	collimator roll offset, module j
ε_y	collimator yaw misalignment

X-ray Time Keeping

u_0	raw pulsar signal
ω_1	prefiltered pulsar fundamental frequency
u_1	prefiltered pulsar signal
u_d	phase detector signal
ω_2	VCO output frequency

u_2	VCO output signal
ω_0	VCO center frequency
u_f	loop filter output signal
θ_e	PLL phase error
θ_1	prefiltered pulsar phase
θ_2	VCO output phase
$F_{lf}(s)$	loop filter transfer function
K_f	loop filter gain
τ_1, τ_2	loop filter pole/zero locations
s	LaPlace operator
ω_{vco}	VCO center frequency
Θ_2	VCO output phase, LaPlace domain
$U_f(s)$	loop filter output signal, LaPlace domain
$U_0(s)$	pulsar raw signal, LaPlace domain
$U_1(s)$	pulsar prefiltered signal, LaPlace domain
$U_d(s)$	phase detector output signal, LaPlace domain
$F_{pf}(s)$	prefilter transfer function
H(s)	PLL linear transfer function
ω_n	PLL natural frequency
ζ	PLL damping ratio
$\Delta\omega_H$	hold range
$\Delta\omega_P$	pull-in range
$\Delta\omega_L$	lock-in range
T_L	lock time
$\Delta\omega_{PO}$	pull-out range
Δt	time error
Δx	position error
c	speed of light
Δf	frequency offset

v_{los}	instrument velocity in the direction of the line of sight to the pulsar
f_{pulsar}	pulsar fundamental frequency
C_i	total photons in bin i
B_i	photons in bin i due to background
N_i	photons in bin i due to Poisson noise
S_i	photons in bin i due to steady part of pulsar
P_i	photons in bin i due to pulsar oscillations
$a_1 \ldots a_4, b_1 \ldots b_4$	Crab pulsar fit parameters
i	bin number
P_{1i}	mean rate in bin i from first pulse
P_{2i}	mean rate in bin i from second pulse
η_c	normalizing parameter
σ_i	standard deviation of noise in bin i
K_{vco}	VCO gain
K_{loop}	PLL loop gain
K_{pd}	phase detector gain
h_{inp}	amplitude of prefiltered pulsar fundamental

Chapter 1: Introduction

1.1 Problem Statement

Since the discovery in 1962 that many stars emit x-rays, the scientific community has invested a great deal of time and effort in characterizing and understanding the x-ray sky. This knowledge has reached a level of maturity that will now allow x-ray sources to be used as a set of inertial references to measure the attitude, time and position of a satellite. First proposed by Dr. Kent Wood in a 1993 paper (Wood, 93), the process of using x-ray sources as references for measuring the state of a spacecraft is referred to as "x-ray navigation."

Currently available instrumentation makes it possible to determine the attitude, time and position of a satellite in an autonomous or semi-autonomous fashion. In fact, technology such as GPS may soon make it possible, in some instances, to measure these parameters with a single, integrated instrument. X-ray navigation is another tool that will ultimately make it possible to determine the state of a spacecraft with a single, integrated instrument. Moreover, x-ray navigation can be used on satellites on interplanetary missions as well as those in low earth orbit. This new concept will also make it possible

to use the payloads of satellites dedicated to x-ray science to track the satellite time, attitude and position thus obviating the need for instruments specifically dedicated to measuring these parameters. In this thesis, the feasibility of x-ray navigation will be explored. This feasibility is demonstrated through a combination of simulation and experimentation.

The launch of the Unconventional Stellar Aspect Experiment (USA) aboard the Advanced Research and Global Observation Satellite (ARGOS) in late 1996 will be the first step in developing this new class of sensors. Simulations of x-ray timing concepts were performed with this platform in mind. Furthermore, extensive design, analysis and manufacturing work on USA was done to support the experiment. This design work serves as an excellent case study in the design of satellite systems and will be described in detail.

The High Energy Astronomical Observer (HEAO-1) was a satellite launched in 1977 and dedicated to making observations of the sky in the x-ray regime. Data from this mission is available from a database at SLAC and was used to demonstrate the feasibility of attitude determination of a spinning spacecraft from observations of x-ray sources.

1.2 History of X-ray Missions

The growth in the field of x-ray astronomy coincides directly with the development of launch vehicles capable of placing instruments sufficiently above the atmosphere of the earth to detect x-rays (Table 1.1). This is due to the fact that the atmosphere is opaque to light in the x-ray regime (~0.1 keV to ~ 1 MeV). The first detection of x-rays from a nonterrestrial source came in 1949 when Geiger counters flown on a sounding rocket showed that the sun emits x-rays (Bradt et al 1992). In 1962 another sounding rocket experiment detected x-rays from Sco-X1, the first indication that x-rays are emitted by bodies outside the solar system (Ibid). Early experiments were also performed using high altitude balloons to carry larger detectors to lower altitudes than the sounding rockets, but for much longer periods of time. These experiments typically

looked for the higher energy photons that could penetrate the remaining atmosphere above the balloons.

The first satellite to make observations of the x-ray sky was the Orbiting Solar Observatory 3 (OSO-3) launched in 1967. Among other things, it produced an all-sky map of the diffuse x-ray background in the 10-40 keV range (Ibid). The Vela series of satellites launched by the Department of Defense also detected celestial x-ray sources in this time period.

With its launch in 1970, Uhuru became the first satellite to be dedicated entirely to celestial X-ray astronomy (Ibid). Uhuru was a spinning satellite with a spin period of about 12 minutes that was placed into a nearly equatorial orbit. Using a set of proportional counters sensitive to 2-20 keV x-rays fitted with 1° x 10° collimators (full width half maximum), Uhuru produced the first detailed x-ray catalog, a catalog that contains 339 objects with intensities as low as about 10^{-3} of the intensity of the Crab nebula (Ibid). This map showed the clustering of sources in the galactic plane as well as a large number of extragalactic sources spread isotropically in the sky (Ibid). Towards the end of its mission, Uhuru would be the first satellite to use x-ray sources as an attitude reference.

Launched in 1972, Copernicus (OAO-3) was the first mission to provide detailed (~10 arc-minute) resolution of an extended x-ray source. The Skylab missions of 1973-1974 used two grazing incidence telescopes to take an image of the sun in x-rays with 2 arc-second resolution (Ibid). Using a coded aperture mask to image the sun in x-rays was first proposed by Dicke in 1961 (Dicke, 1968). This foreshadowed wide-field pin-hole cameras flown on Ariel-5 in 1976 and the first use of a coded mask to image the galactic center in 1978 (Bradt et al, 1992). The Ariel-5 mission also found several x-ray pulsars with periods of minutes.

Between 1977 and 1981 NASA operated two large scientific satellites dedicated to x-ray astronomy. These were the High Energy Astronomy Observatories, HEAO-1 and HEAO-2 (Einstein). HEAO-1 was a spinning survey mission while HEAO-2 was a pointed imaging mission. The third satellite in the series, HEAO-3, was a cosmic ray and gamma-ray mission.

Mission	Lifetime	Mission Class	Science
OSO-3	1967-1968	Spinning	Diffuse Background
OSO-5	1969-1972	Spinning	Diffuse Background
Vela Series	1969-1979		X-ray Bursts
Uhuru	1970-1973	Spinning	Catalog
OSO-7	1971-1973	Spinning	Catalog
Copernicus	1972-1981	Pointed	SNR Mapping
ANS	1974-1976	Pointed	X-ray Bursts
Salyut-4	1974-1975	Pointed	Cyg X-1, Her X-1
Ariel-5	1974-1980	Spinning	Catalog
Apollo-Soyuz	1975	Pointed	SMC X-1 Pulsations
SAS-3	1975-1979	Spinning/Pointed	Precise Positions
OSO-8	1975-1978	Spinning	
HEAO-1	1977-1979	Spinning/Pointed	All-sky Catalog
Einstein	1978-1981	Pointed, Imaging	Imaging
Ariel-6	1979-1981		GX 1+4 Position
Hakucho	1979-1984	Spinning	X-ray Bursts
Astron	1983-1988	Pointed	Her X-1 Low State
Tenma	1983-1984	Spinning	
EXOSAT	1983-1986	Pointed	QPO's
Ginga	1987-1991	Pointed	AGN's
Kvant/Mir	1987-		
Granat	1989-	Pointed, Imaging	Galactic Center
ROSAT	1990-	Pointed	Catalog
Astro-1	1990	Pointed	Spectra
Spartan		Pointed	

Table 1.1: X-ray Missions (Bradt et al, 1992)

The HEAO-1 mission was a spinning platform consisting of four primary experiments (Ibid):

1. Large Area Sky Survey (LASS or HEAO-A1): Four proportional chambers totaling 1.0 m^2 that were sensitive to x-rays in the 1-20 keV range. Each detector had a collimator and was designed to use the spinning action of the satellite to survey the entire x-ray sky. The HEAO-A1 experiment produced a catalog of sources with intensities as low as 10^{-3} the intensity of the Crab that included 842 x-ray sources. The raw data from these surveys was used in the attitude determination experiments described later. The HEAO-A1 data also had excellent time resolution which may allow for future experiments in x-ray time determination studies.

2. Cosmic X-ray Experiment (CXE): An array of proportional chambers 0.4 m^2 in area designed to study the diffuse x-ray background in the 0.2 keV to 60 keV range.

3. Modulation Collimator (MC): This experiment was designed to determine the position of x-ray sources to about one arc-minute accuracy.
4. A high energy experiment for observations up to ~10 MeV.

The Einstein spacecraft was a powerful x-ray imaging mission that employed grazing-incidence focusing optics for the first time in celestial x-ray astronomy. This system was sensitive to energy in the range of 0.1-4 keV and could resolve sources as dim as 10^{-7} the intensity of the Crab (Ibid).

The 1980's saw several satellites that extended the knowledge of the x-ray sky in a variety of ways. These included EXOSAT, Hakucho, Tenma and Ginga (Ibid).

These missions of the past three decades have led to a body of knowledge in x-ray astronomy that will enable the x-ray navigation concept. Some of the important characteristics of the x-ray sky are summarized below:

1. There are a relatively small number of bright sources in the x-ray sky. The 842 sources in the HEAO all-sky catalog vary by 4 orders of magnitude in intensity from brightest to dimmest.
2. Many sources reside in the galactic plane, but there are significant sources in other areas of the sky.
3. There is a faint diffuse x-ray background whose origin is not well defined at this time.
4. The sources and background tend to be fairly faint and observations of them may be modeled as Poisson processes.
5. Many of the sources have been identified as x-ray pulsars and have periods that range from tens of milliseconds to months.

1.3 Satellite Navigation Principles

1.3.1 Attitude Determination

The sensors designed to measure the attitude of a spacecraft can be grouped according to their reference objects. Sun-sensors measure the pointing angles of the spacecraft relative to the sun, horizon-sensors use the limb of the earth as a reference, and star trackers use optical or ultraviolet measurements of the locations of guide stars. Recently, it has been shown that the GPS system can be used to determine the attitude of LEO satellites by measuring the relative distances to the individual GPS satellites (Cohen, 1991). With the exception of GPS, all of these sensors are sensitive to emissions from celestial bodies in the infra-red, optical, or ultraviolet wavelengths.

Many of the celestial objects visible in optical wavelengths have significant radiant signatures in other wavelengths. In particular recent studies of the sky in x-ray

wavelengths indicate that a sensor designed to detect such objects would make an excellent star tracker. In fact, the Uhuru satellite was the first satellite to act as an x-ray star tracker. In December of 1972 the optical star trackers used to provide one arc-minute level orientation measurements failed. In order to superpose the count rates from successive scans the aspect data from the magnetometers and sun sensor were used. This was supplemented by using the locations of bright x-ray sources to synchronize the scans (Forman et al 1978).

Dr. Wood proposed two basic designs of an x-ray star tracker (Wood, 1993). The first employs a coded aperture mask and a pixelated detector to image the sky directly. The image is then correlated with a map of the x-ray sky using any of the methods developed for more traditional star trackers. The second method would use a collimated detector (non-pixelated) and a mechanical scanning device to scan over a known source repeatedly. This is similar to traditional star scanners that search the sky either mechanically or electronically to keep a guide star in the field of view. If a collimated x-ray detector is placed on a spinning spacecraft, the scanning mechanism is supplied by the spacecraft and a separate scanning mechanism is not necessary.

There are several advantages to measuring attitude by reference to x-ray emitting objects:

1. The sparsity of the x-ray sky simplifies the pattern recognition problem.
2. The periodicity associated with some sources could be an excellent way of identifying guide stars and thereby reducing the scope of the pattern recognition problem.
3. X-ray detectors are robust and do not require any optics or special cooling.
4. The measurement of attitude is done in an inertial frame and is, in principle, capable of accuracies comparable to conventional star trackers.
5. The measurement of time, attitude and position can be done autonomously by a single integrated instrument.

1.3.2 Time Keeping

Time on spacecraft has typically been kept by a local crystal oscillator with periodic corrections from the ground. A quartz crystal oscillator can be made stable to a part in 10^6 without much effort. The Transit Navigation Satellites had a requirement for a very stable frequency source over short periods of time. These used a double dewar system to isolate an oscillator thermally, thus achieving a local frequency stability of a part in 10^9 (Black, 1990).

The Gravity Probe A (GP-A) experiments flow by Bob Vessot used hydrogen masers to get a time reference that was stable to a part in 10^{14} over integration periods from one minute to one hour. Launched on a sounding rocket, the payload clock was compared to the time kept by a ground based hydrogen maser as a test of the Theory of Relativity (Vessot, 1995).

While these examples show that it is possible to fly extremely stable local clocks on satellites, they also show that it is very difficult and very costly to do so. Future missions that require accurate local timing will have to use new methods. With the advent of GPS, spacecraft in low earth orbit can now keep accurate local time semi-autonomously (Hoech, et al, 1994).

A more flexible and potentially more accurate method of keeping accurate local time on satellites in any orbit would use the many x-ray emitting objects that are also x-ray pulsars. These pulsars have been shown to have periods with stability equivalent to atomic clocks and can be used as a completely autonomous absolute time reference (Wood, 93). By observing an x-ray pulsar over an extended period of time, an inexpensive local crystal oscillator can be corrected for long term drift by using a phase-locked loop to lock it in frequency and phase to the pulsar. By extension, several local oscillators, each with a different center frequency, can be locked to several different pulsars simultaneously. This will provide an autonomous measure of time from scales of milliseconds to months allowing for autonomous initialization as well as a redundancy in the time measurement. This technology will enable missions to be flown that require accurate time information to be delivered without ground intervention.

1.3.3 Position Determination

The position of a satellite in orbit has traditionally been determined by ground based tracking stations. After estimating the ephemeris of the orbit, these parameters are uplinked so that the satellite can estimate its position as a function of time. Methods of determining the position of a spacecraft autonomously have been suggested, but have yet to be implemented on operational satellites. A great deal of research was performed in the late 1960's and early 1970's to perfect some of these techniques. These included tracking known landmarks on the earth, but this method was hindered at times when cloud cover obscured landmarks (White, 1975). The TRIAD-1 satellite used its drag-free reference to improve the accuracy of ephemeris predictions by removing the uncertainty in the propagation of the orbit parameters caused by unmodelled and random disturbances. By using the drag free system to cancel these disturbances, the satellite position could be projected 15 days into the future with an along track navigation error of 100 m and a slant range navigation error of 100 m (Staff of the Space Department, 1974).

Other methods involved measuring the time of occultation of a guide star by the earth or the moon. One interesting proposal would measure the atmospheric refraction from a known star as that star sets behind the earth (White et al, 1985). Recent studies suggest that such an approach can pinpoint the position of a satellite to hundreds of meters.

With the GPS system coming on line, it will be possible to determine the position of a satellite in low earth orbit semi-autonomously. That is, the satellite will not need any direct interference from ground controllers, but will be dependent on the GPS system for its position updates. The GPS system is, in turn, dependent on ground control for its proper operation.

The position of a satellite in orbit can be determined by observing the occultation of an x-ray guide star by the earth or the moon (Wood, 1993). By measuring the occultation of several sources in different directions, a position fix can be made

autonomously. This would require some sort of x-ray imaging system (coded mask, grazing incidence mirrors or scanning collimator).

1.4 USA Experiment Design Issues

The Stanford Linear Accelerator Center (SLAC) and the Naval Research Laboratory (NRL) are cooperating on the design, manufacturing and operation of the Unconventional Stellar Aspect Experiment (USA). USA is an x-ray telescope schedule to be launched into low earth orbit aboard ARGOS, a satellite funded as part of the Air Force STEP Program and built by Rockwell International for launch in early 1997. This experiment involves mounting two large x-ray detectors in a gimbaled structure. SLAC was responsible for the design, manufacturing and test of the support structure as well as the thermal design of the entire experiment. Additionally, SLAC was responsible for the design, manufacturing and testing of three collimators (two flight, one spare) used in the experiment as well as various flight and ground software issues. In order to build this experiment on the short timescale and limited budget it was afforded, it was necessary to work closely with other team members at the Naval Research Laboratory, Rockwell, the Air Force, and the Aerospace Corporation. This work offers an excellent case study for designing satellite systems in small semi-autonomous groups.

1.5 USA/HEAO Navigation Experiments

The Unconventional Stellar Aspect Experiment will provide a unique platform for the demonstration of x-ray navigation (Wood et al USA). Two RS-6000 class (20 Mips) computers will have real-time access to the data from the two USA detectors. This data can then be used to determine the state of the spacecraft. A truth measurement of time and position will be available from a GPS receiver on board the spacecraft while the attitude of the spacecraft will be available from the ADACS system. The time and

attitude truth measurements will be available in real time while the position measurement will be available in post-processing.

USA will be used as an experimental scanning collimator system, thus demonstrating an operational x-ray attitude determination system. By scanning over a small section of the sky where a guide star is known to reside, an "image" of that section of the sky can be formed. The location of the guide star within this image is then used to determine the attitude of the satellite in real time.

USA can also be used to track the local time using x-ray pulsars. A simple timing experiment would involve programming the RS-6000 computer to run as a digital phase-locked loop with the stream of scientific x-ray data as its input. The performance of this loop can then be compared to the truth measurement and a simple performance measure sent down in the data stream.

USA will also make measurements of the position of the ARGOS satellite by observing the occultation of known guide stars by the earth and the moon.

Fortunately, the data from previous x-ray missions can be used to prove some of these navigation concepts now. As previously discussed, the High Energy Astronomical Observatory is a satellite that flew in the late 1970's and mapped the sky in the x-ray regime. The data from this experiment are still available and have been used to demonstrate the feasibility of x-ray attitude determination on spinning spacecraft.

1.6 Contributions

This thesis is dedicated entirely to exploring the possibilities of x-ray navigation. To this end a great deal of effort was expended to test the ideas developed here through simulation or experimentation. Furthermore, the USA Experiment is seen as a critical tool for exploring these concepts in the future. The main contributions of this thesis are as follows:

1. Designed, manufactured and tested the structural components of the Unconventional Stellar Aspect Experiment. This demonstrated that dip brazing can be

used as a cost efficient manufacturing method for large space structures whose design is driven by stiffness considerations and not strength considerations.

2. Explored the use of x-ray imaging devices (star mapper) on inertially pointed and/or slowly rotating vehicles as an attitude measurement instrument, showing that measurement update rates in the 100 Hz range are feasible.

3. Explored the use of simple collimated x-ray detectors on spinning spacecraft as an attitude measurement instrument (star scanner). A theoretical framework for the design of both single detector and differential detector instruments was provided including a discussion of error sources. Errors due to the polhode motion of a spinning body and manufacturing misalignments of the instrument were described and models for their estimation were suggested.

4. Demonstrated the operation of single detector and differential detector star scanners using data from the High Energy Astronomical Observatory, a spinning satellite launched in 1978. Four different detector schemes were demonstrated: single detector, differential detector, single detector with a second order model and differential detector with a second order model.

5. Explored the use of an x-ray pulsar as a stable, autonomous frequency reference by simulating the performance of a phase locked loop in acquiring and locking onto the Crab Nebula pulsar. A discussion of potential error sources present in such an application was included.

1.7 Thesis Outline

When I first joined the SLAC/NRL team, it was with the understanding that I would be responsible for the structural and thermal analysis necessary to verify the design of the Unconventional Stellar Aspect Experiment. That responsibility soon grew to include the design, manufacturing and testing of the USA gimbal structure. This required a close working relationship with both those physicists building the experiment and those who would be the end-users of the data generated by USA. This relationship led to my appreciation for the possibilities of x-ray navigation - the subject of this work. For this

reason, I have arranged this thesis in two sections, starting with the design of the Unconventional Stellar Aspect Experiment and then moving on to discuss methods for using the x-ray sky to measure the orientation of a spacecraft and to provide it with a stable frequency reference.

Chapter 2 covers the design, manufacturing and testing of the Unconventional Stellar Aspect Experiment. This begins with a general description of the mission and experiment and the design requirements. An integrated design and analysis process is discussed in which a finite element model of various structural design options was used. This lead to a novel design for such a large structure as USA that was made possible by using a process called dip brazing. A complete discussion of the dip brazing process and the USA Structural Test Program is included. Finally, Chapter 2 ends with a summary of the USA thermal analysis, including a description of the thermal design and the various operational modes that are important considerations in a thermal design.

The concept of x-ray attitude determination is introduced in Chapter 3. First, a feasibility study that suggests x-ray imagers can be used as precision pointing devices (star mappers) on inertially pointed or slowly spinning spacecraft is presented. The second part of Chapter 3 develops the idea of using collimated x-ray detectors on a spinning spacecraft to determine its orientation (star scanners). This begins with a description of the signal generated by such an instrument given the general rotational motion of the spacecraft. Two models for the operation of x-ray star scanners are presented - a first order model that assumes the spin axis is properly aligned with the instrument axes and a second order model that includes misalignment effects. Three general instruments are described - a single detector/collimator system, a differential detector/collimator system using two detectors and a differential detector/collimator system using a single detector and two collimators.

In Chapter 4 the concept of x-ray attitude determination is demonstrated by using archival data from the HEAO-1 mission. Four different cases are described and their results presented:

1. Single detector, single collimator with first order model
2. Dual detector, dual collimator differential instrument with first order model

3. Single detector, single collimator with second order model

4. Dual detector, dual collimator differential instrument with second order model

The concept of autonomous x-ray timing is discussed in Chapter 5. A simulation of a phase locked loop used to lock onto the Crab Nebula pulsar is described. This includes a general discussion of phase locked loops as well as some of the errors to be anticipated in using an x-ray pulsar as an autonomous frequency reference.

Chapter 6 provides an overview of the thesis and an extensive list of suggestions for future research.

Chapter 2: Design Aspects of the Unconventional Stellar Aspect Experiment

2.1 USA Mission

The Unconventional Stellar Aspect Experiment (USA) will provide a unique platform for experiments in the area of x-ray navigation. Concurrently, USA is tasked to provide large quantities of high resolution x-ray timing data on 30 of the most x-ray luminous stellar objects known. Observations for each object will be made with timing resolution on the order of 10^{-6} sec (1 μsec) for about one month of total elapsed time. As previously described, USA is an experiment that will be flown as one of several on an Air Force satellite called the Advanced Research and Global Observation Satellite (ARGOS). USA will be mounted on the aft or antivelocity face of ARGOS (Figure 2.1). From this position USA will be able to slew its x-ray detectors to track any target in its field of regard continuously for about 20 minutes per orbit. ARGOS is in a sun-synchronous orbit at an altitude of 450 n.mi. (Figure 2.2, Table 2.1). This will allow USA to observe

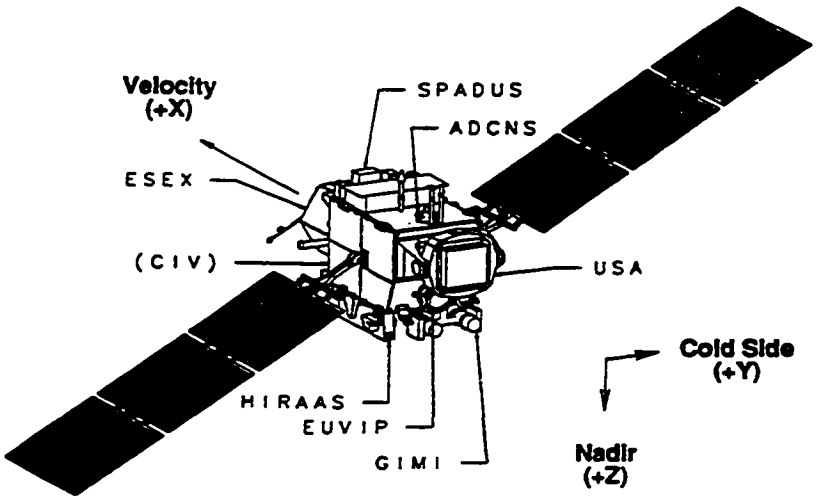

Figure 2.1: Advanced Research and Global Observation Satellite

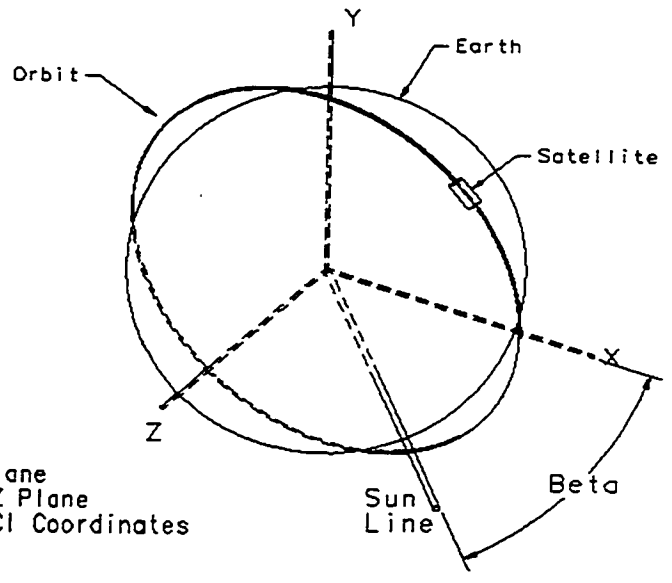

Notes:

1. Orbit in XY Plane
2. Sun Line in XZ Plane
3. (X,Y,Z) are ECI Coordinates

Figure 2.2: Advanced Research and Global Observation Satellite Orbit

the entire celestial sphere over its lifetime as the precession of the orbit brings targets into the instrument field of regard.

Orbit Apogee	450 +/- 10 n. mi.
Orbit Perigee	450 +/- 10 n. mi.
Orbit Inclination	98.7 +/- 0.06 degrees
Beta Angle (BOL)	36 +/- 3 degrees
Beta Angle (EOL Min)	15 degrees
Beta Angle (EOL Max)	54 degrees
Orbit Period	101.6 min (nominal)

Table 2.1: USA Orbit Parameters

2.2 USA General Description

The Unconventional Stellar Aspect Experiment (Figure 2.3) consists of two proportional chambers in a two-axis gimbal system. This gimbal system allows for full movement of the detectors in pitch and yaw so that any source in the field of regard can be tracked during an orbit (+70°/-110 ° pitch, +/-90 ° yaw). The proportional chambers were refurbished after a previous mission on the shuttle called Spartan. Combined they weigh approximately 210 lb. This includes the two 12 in spherical gas tanks carried on the backs of the detectors. A complete description of the mass properties of the USA experiment is given in Table 2.2. Each proportional chamber consists of the following components (see Figure 2.4):

1. One aluminum proportional chamber made from the detector body and detector backplane. The detector backplane is bolted to the body with a viton o-ring between them to provide a vacuum tight seal. The detector electronics are located on the outside of the detector backplane. The proportional chamber is filled with P-10 gas (90% Argon,

10% Methane at 14.7 psi. This is supplied by a spherical titanium gas tank and pressure regulation system.

2. One aluminum detector cover bolted to the detector backplane and covering the electronics package. This protects the electronics package and provides a common radiator for all of the electronics.

3. One 12 in diameter spherical titanium gas bottle containing P-10 gas at 2700 psi. This is bolted to the detector backplane. The gas bottle contains no internal heat generation and is connected to the proportional chamber via a small bolted surface.

4. One 2.5 micron thick mylar window held between the detector body and the collimator frame. This window provides containment for the P-10 gas while absorbing a minimum of the incoming x-rays. This is particularly important for x-rays with energies of about 1 keV since the presence of the mylar window defines the lower end of the detector energy acceptance.

5. One aluminum collimator frame holding two collimator modules against the mylar window. The frame is bolted against the detector body with another viton o-ring between the two, making a seal that prevents the loss of chamber gas.

6. Two collimator modules made from copper hex-cell. The modules are held within the collimator frame by an interference fit and provide support to the mylar window. A fine wire mesh is placed between the window and the collimator modules for additional support and to protect the window from any small burs on the collimators.

7. One heat shield and aluminum heat shield frame. The heat shield is made from 2.5 micron thick second surface aluminized mylar and is suspended 0.25 in above the collimator modules by the heat shield frame. This keeps the sun heat input through the face of the collimator to a minimum.

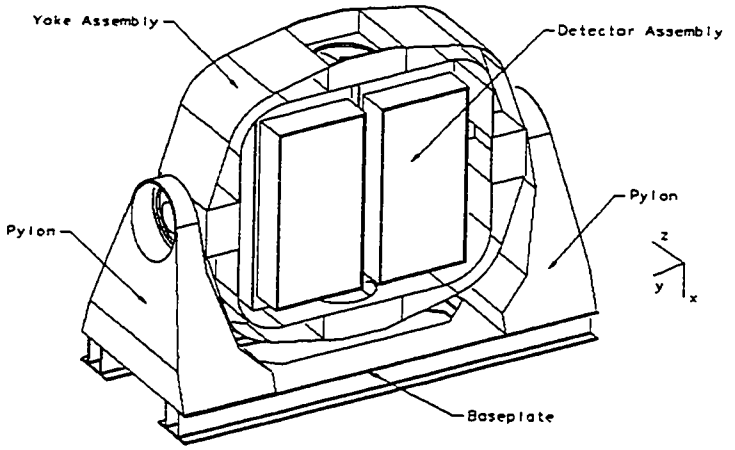

Figure 2.3: Unconventional Stellar Aspect Experiment

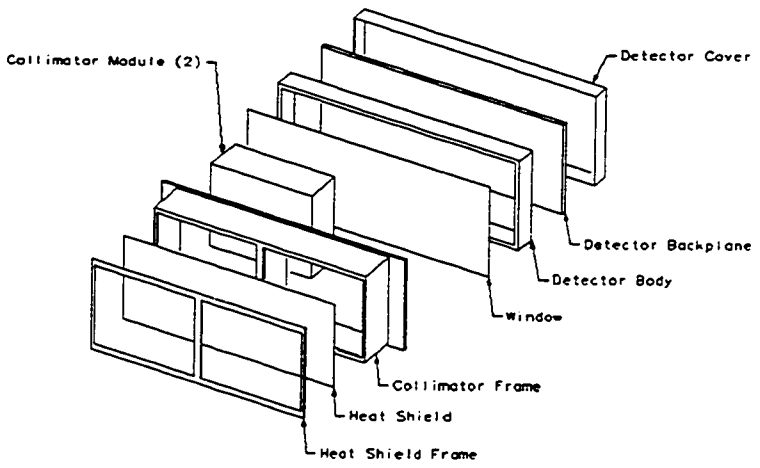

Figure 2.4: Unconventional Stellar Aspect Experiment Proportional Chamber

Component	System	Quantity	Mass (each) (lb)
Collimator	Detector	2	15.1
Collimator Frame	Detector	2	10.3
Heat Shield Frame	Detector	2	6
Proportional Chamber	Detector	2	10
Detector Backplane & Electronics	Detector	2	39.8
Gas Tank	Detector	2	24.1
Detector Subtotal	*Detector*	*1*	*210.6*
Pylon	Gimbal	2	32
Motor	Gimbal	2	22
Encoder	Gimbal	2	22
Baseplate	Gimbal	1	51
Central Electronics	Gimbal	1	20
Yoke	Yoke	1	64
Wire Harnesses	Yoke/Gimbal	1	43
USA Total	*USA*	*1*	*540.6*

Table 2.2: USA Mass Properties

The two detectors are mounted in an aluminum frame which is suspended inside of an aluminum yoke assembly by an encoder assembly on one end and a motor assembly on the other. A launch lock that constrains the motion of the detector about the yaw axis during ascent is mounted to the inside of the yoke and attaches to a flange that is mounted on one of the detectors. The yoke is suspended between two aluminum pylons by another pair of motor/encoders. The pylons are bolted to an aluminum I-beam baseplate. The baseplate is attached to the spacecraft with eight 3/8 in titanium bolts (four on each side). Pointing of the detectors is achieved through the two motor/encoder assemblies. The yaw motor/encoder assembly pivots the detector inside of the yoke while the pitch

motor/encoder assembly pivots the yoke assembly between the two pylons. The pylon/baseplate system (Figure 2.5, Table 2.2) consists of four primary components:

1. Two pylons constructed from 0.25 in 6061/T6 aluminum plate forming a box structure. Each pylon is bolted to the baseplate with six 5/16 in stainless steel bolts and two flange assemblies. The flange assemblies tie the pylon outside plate to the baseplate in two locations.

2. One baseplate constructed from 6061/T6 aluminum I-beams. The baseplate is bolted to the space vehicle through eight 3/8 in titanium bolts. The launch lock that constrains the yoke in motion about the pitch axis during ascent is mounted in the center of the baseplate.

3. One central electronic box radiator (CE Box) that is integrally attached to the +Y side pylon. The CE Box is bolted to the baseplate and the radiator. The radiator, in turn, is bolted to the pylon.

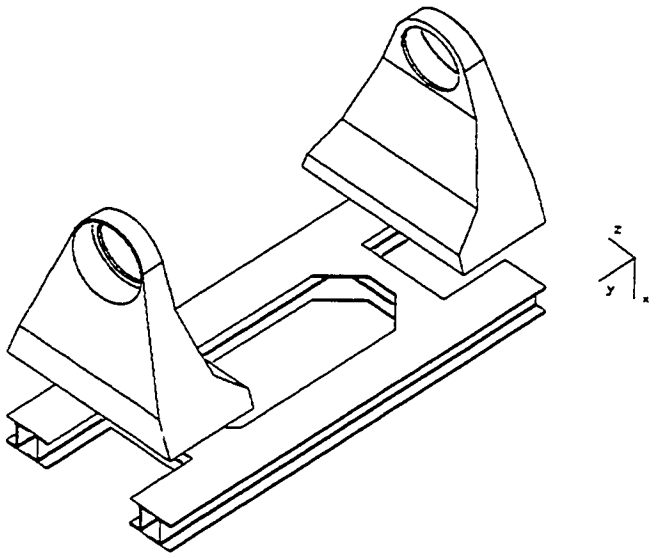

Figure 2.5: Unconventional Stellar Aspect Experiment Pylon/Baseplate Assembly

2.3 USA Structural Design and Analysis

The design of the USA gimbal structure is governed by the P91-1/USA Interface Control Document (ICD, included in Appendix A). This document specifies the design environment in terms of expected external loads and sets the design performance requirements. The following is a list of design issues pertinent to the USA structure:

1. The lowest vibration mode of the structure in the launch condition must be greater than 50 Hz in frequency. This allowed the spacecraft design to proceed by modeling the experiments as rigid bodies, thus alleviating the need for the experimenters to deliver extensive finite element models early in the program.
2. All structural members must be designed with a Factor of Safety (FOS) of 2.0 if no static load testing is performed. Members that are to be static load tested must be designed with a FOS of 1.25. (See Tables 2.3 and 2.4)
3. A positive margin of safety under launch loads must exist on all structural members. This must be demonstrated through analysis and/or testing.
4. Clearance between the detector and yoke and between the yoke and pylons and baseplate must be maintained throughout their motion.
5. Launch locks must be positioned to provide high stiffness at launch while allowing full motion of the assemblies after their retraction.
6. The central electronics box must be positioned inside one of the pylons.
7. The structure must fit inside the envelope specified in the USA ICD.
8. Access to the central electronics box, the motors, encoders and feed-throughs must be provided.
9. Final assembly of the structure should be made simple as possible.
10. Each motor/ encoder pair should be co-aligned and the lines of action of the two pair should be normal to each other in the assembled system.
11. Weight and cost of the structure should be kept to a minimum.

	Axial (g's)	Lateral (g's)
Lift Off	+3.25/-0.26	4.0
Main Engine Cut Off	+7.1	0.13

Table 2.3: USA ICD Static Flight Accelerations

	Axial (g's)	Lateral (g's)
Lift Off	+6.5/-0.52	8.0
Main Engine Cut Off	+14.2	0.26

Table 2.4: USA Design Flight Accelerations

A preliminary structural design for the USA experiment was performed at NRL using design techniques that are standard in the aerospace community. This called for machining the yoke and pylons from solid pieces of 6061/T6 aluminum plate. This design was accompanied by a finite element model run on NASTRAN that verified its acceptability as a preliminary design. The model was transferred to SLAC (along with the responsibility for the analysis and design of the supporting structure) and ported into CAEDS. CAEDS is a standard CAD package written by SDRC Corporation and supported on IBM RS6000 machines. It provides an excellent platform for both finite element modeling (FEM), solid modeling and drafting. The solid modeling and drafting capabilities would later prove to be critical to the manufacturing of USA.

An initial analysis of this model indicated that the primary design driver is the minimum natural frequency requirement (>50 Hz). Additionally, the primary static load is due to the axial component of the acceleration (in the Z direction, along the direction of launch) of the detector in the yoke. This load causes a bending load in the yoke and is passed to the pylons through the motor and encoder to the pylons. The pylons are then subject to a combination of compression and bending. The lateral component of acceleration can act in any direction in the YZ plane. This will cause a combination of bending and twisting of the yoke and a bending and twisting of the pylon depending on the direction of the acceleration.

Several different yoke cross-sections were modeled. These included the baseline C-section (NRL), a T-section and an I-section. Each design was kept to a constant total weight. The performance of the design in terms of the static load and natural frequency were compared to the baseline design. It should be noted that the NRL designed yoke was limited to a C-section with external access by machining requirements. The depth of cut necessary to machine an I-beam cross-section (~5 in) was not feasible at a reasonable price. Furthermore, a C-section opening to the inside of the yoke would make machine tool access very difficult, driving up the manufacturing costs. However, the design survey indicated that the most efficient cross section for the yoke was an I-beam with the web lying in the XY-plane. Furthermore, it was found that by closing the I-beam section at the four corners of yoke, the box structure formed would greatly increase the torsional stiffness of the structure (Figure 2.6). This could be done by placing two additional webs between the inner and outer flanges at each corner. This additional stiffness was not necessary for the preliminary design to meet the specifications set in the ICD.

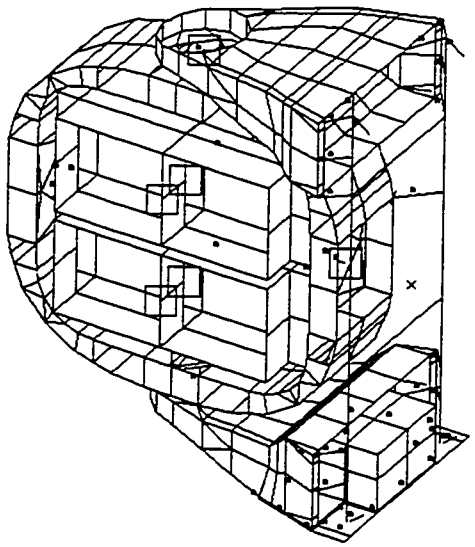

Figure 2.6: Unconventional Stellar Aspect Experiment Finite Element Model

As the overall USA design became better defined, we suffered a weight growth of approximately 25% from the estimated masses to the as-manufactured masses. It then

became necessary to include the box structure in the design to meet the natural frequency requirement. This closed box structure made machining the yoke from a solid block of aluminum even more impractical. Three alternate methods were devised to manufacture the yoke: bolted structure, welded structure, and a dip-brazed structure. The approach of using several small pieces bolted together was rejected for three reasons: such structures would be difficult to analyze, inefficient in their use of weight and would make it difficult to maintain close tolerances on the motor mount locations without expensive jigging. The fact that this structure contained precisely aligned motors and encoders acting along common axes meant that the locations and alignments of the motor and encoder mounts had to be placed as accurately as possible. The thermal deformations associated with a welded structure were deemed to be too great to use this technique. Welding also requires extensive testing and qualification for use in manufacturing space qualified structures.

It was decided to manufacture the support assembly with a process called dip-brazing (Figure 2.7). Dip brazing has been used for 30 years to bond fairly small parts together where a direct contact is necessary, but has not been used extensively to manufacture space qualified structural components (Altshuller, et al, 1990). With this technique a bond is formed between two pieces of aluminum as follows:

1. The bond surfaces of the joints are cleaned and prepared.
2. Braze material is inserted into the joints and the joints are held together by tack welds. The braze material has a melting point that is typically 50 ^{o}F lower than the parent material.
3. The assembly is preheated.
4. The assembly is dipped in a bath of molten salt. This heats the joints to a level that melts the braze material and causes it flow, forming the bond.
5. The assembly is removed from the bath and quenched.
6. The assembly is heat-treated.

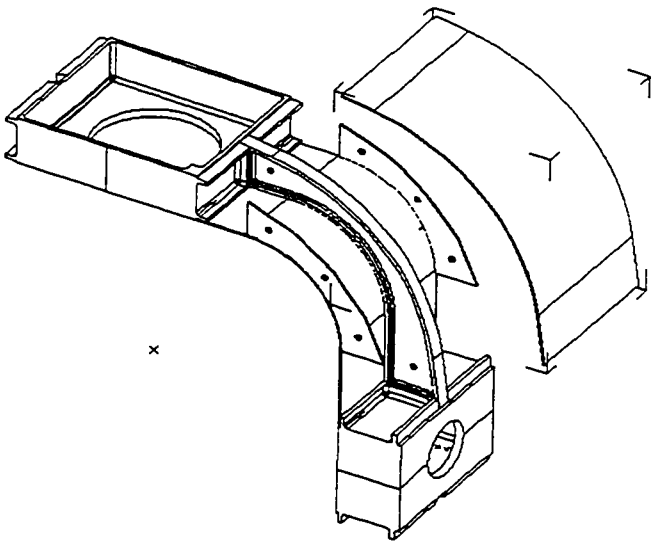

Figure 2.7: Unconventional Stellar Aspect Experiment Yoke Assembly

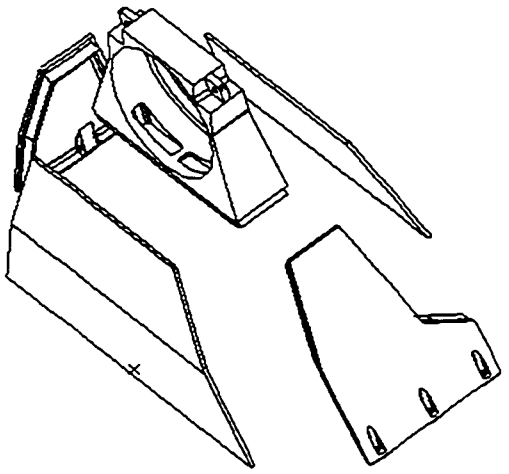

Figure 2.8: Unconventional Stellar Aspect Experiment Pylon Manufacturing Assembly

Because the dip-brazing process is fairly new to the aerospace community and no one within the collaboration, at the Aerospace Corporation or at Rockwell had any

experience building large assemblies with it, a conservative approach to manufacturing was used. This included the following elements:

1. Large margins in the strength of the structure were maintained, especially at the beginning of the program.
2. The dip-brazing vendor was qualified before the flight articles were constructed.
3. A conservative approach to the design of the braze joints was employed by using large faying surfaces and interlocking parts at all critical joints.
4. A prototype pylon was constructed and static load tested to 125% of the expected worst-case flight load.
5. A structural test program was implemented that was integral to the manufacturing process (see below).

The pylons were also constructed by using the dip-brazing process (Figure 2.8). The design of the pylons was governed primarily by ease of manufacturing and ease of access questions. The +Y side pylon has to contain and support the central electronics box and its accompanying external radiator. Both pylons have wire harnesses that run up to the motor (+Y side) and encoder (-Y side). Therefore both pylons have to provide easy access during assembly and testing. In order to minimize the cost of the pylons and to allow easy access internally, a box construction was used. The side pieces were machined from 1 in (25 mm) aluminum plate stock while the front and back were made from 0.25 in (6 mm) aluminum plate. A bolted cover piece was provided on both pylons.

The dip-brazed design had a 20% reduction in structural weight over the original design and cost about $35,000 to manufacture and test compared with the $80,000 estimate for an integrally machined design.

2.4 USA Structural Test Program

The testing program that was applied to the USA experiment is summarized below:

1. Construction to established specifications:

All dip-brazing was done by Aluminum Dip Braze Co. (ADB) in Burbank, Ca. This work was done in accordance with Mil-B-7553-B Type V Grade B with quality standards per Mil-I-45208. All joint preparation was done to Mil-B-7553-B Type V Grade A specifications. Following the dip-brazing process, all parts were heat-treated to attain T6 conditions. All dip-brazed joints were then inspected by radiographic methods and the results interpreted to determine the fractional braze wetting of each joint (Appendix B). Certifications of Conformance are on file with radiographs for all parts. I was present to videotape the brazing of the prototype pylon and the yoke.

2. Manufacturing qualification:

A series of qualification test samples were built by ADB and tested to failure at SLAC. This work is described in detail in Appendix B.

3. Prototype pylon and flight articles:

After qualifying the manufacturing process, one prototype pylon was manufactured by ADB to prove the overall manufacturing concept. This pylon would later be subjected to a static load test. Only after visual and radiographic inspections of the prototype pylon were performed were the flight articles manufactured. The flight articles included two pylons and one yoke.

4. Quality assurance pull samples:

Each item dip-brazed by ADB was accompanied by five shear samples similar to those used in the manufacturing qualification process. These samples were prepared in the same manner and to the same specification as the prototype and flight articles and were brazed in the same bath and at the same time as their parent articles. The results of these tests are described in Appendix B.

5. Static Load Test

As a final test of the USA structure, the prototype pylon was used in a static load test that subjected the pylon to 125% of the USA ICD loads. This test is described in detail in Appendix B.

2.5 USA Thermal Analysis

An important aspect in the design of any satellite is its response to the thermal environment on orbit. Many components of a spacecraft (electronics, batteries, etc.) must be kept within strict temperature bounds in order to ensure their reliable operation. In order to keep the operating temperatures of these components below the design maximum, the heat generated internally must be given proper paths to flow to specially designed radiators that then radiate that heat to outer space. This is in addition to the significant heat from the sun and earth that is absorbed by all surfaces of the vehicle. To complicate matters, there are scenarios where the power to certain non-essential systems is turned off. In these survival modes, it is necessary to supply survival heat to sensitive components to keep them from getting too cold. The design of the thermal control system requires a detailed model of the spacecraft and simulations of its operation on orbit in all possible scenarios.

While several software packages exist that solve time varying thermal analysis problems, none of these were available to the USA project. So, preliminary thermal design studies were conducted using software that I wrote in MATLAB. The initial versions of this software solved the static case where all temperatures are constant and the thermal inputs are averaged over the orbit. By first considering the static case, I was able to get estimates for survival heat and radiator areas that were within 10% of the final design. The software package was later expanded to the time varying case by integrating the governing equations with time varying heat inputs. This complete package was used to finalize the USA thermal design.

The thermal control system for the USA experiment uses a combination of thermal radiators and survival heaters to maintain the temperature of critical components

within strict bounds (Figure 2.9). The only variables open to the designer are the area of the radiator, the amount of survival heat, and, to a lesser extent, the optical properties of the surfaces of the experiment. The basic thermal design is summarized in Table 2.3.

	Power Dissipation (W)		Design Temperature (C)		Radiator
Component	Operational	Survival	Minimum	Maximum	Area (m^2)
CE Box	35	23	-29	+50	0.15
Motors (2)	1 (ea)	0	-125	+125	0.00
Encoders (2)	0.5 (ea)	0	-125	+125	0.00
Detector Electronics (2)	10 (ea)	10 (ea)	-29	+45	0.05 (ea)
Viton Seal (2)	0	0	-10	+40	0.00
Heat Shield (2)	0	0	-50	+250	0.00

Table 2.5: USA Thermal Design

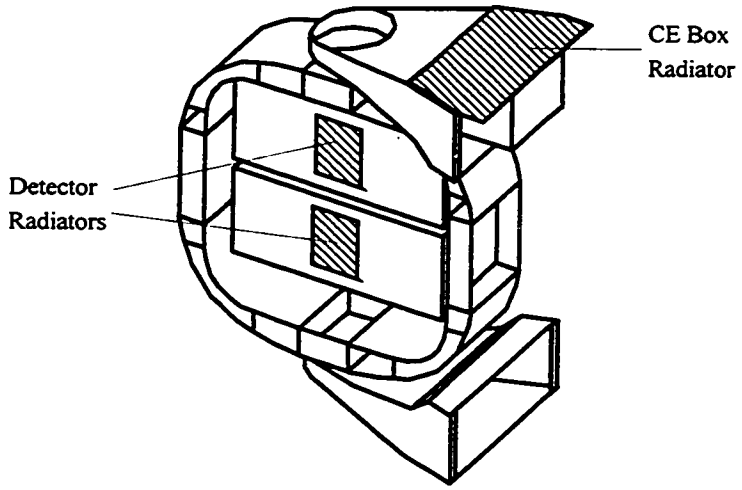

Figure 2.9: USA Thermal Control System

For the purpose of thermal analysis, the USA experiment can be broken into three independent models: the detector assembly, the yoke assembly and the pylon/baseplate assembly. The detector assembly consists of the two proportional chambers and their accompanying collimators, electronics, and gas systems and the detector frame to which they are mounted. This assembly is mounted inside the yoke via a stepper motor and encoder such that it can rotate freely about the local "yaw" axis. The yoke is an aluminum assembly that is in turn mounted between the pylons of the pylon/baseplate assembly via another stepper motor and encoder to provide rotational freedom about the spacecraft pitch axis. The conductive paths connecting the detector and pylon assemblies to the yoke travel a circuitous route through the motor and encoder assemblies. The thermal resistance along these paths is quite large and allows the three models to be considered independently. These models are described pictorially in Figures 2.10, 2.11 and 2.12.

All components of the USA experiment are covered completely in multi-layer insulation, with the exception of specific radiating areas and the detector aperture. This insulation has a blackened kapton outer sheet. The MLI is assumed to have an effective emissivity of 0.01. The effects of the external optical properties of the MLI on the heat leak through the insulation are negligible when compared with the effective emissivity. That is, while the optical properties of the blanket's outer sheet may reject 20% of the incident radiation, the layered properties of the MLI alone rejects 99%. The radiators are covered with a silver-teflon tape that provides a high emissivity in the infrared bands (~0.80) for efficient radiation of internal heat but a low absorptivity in optical bands (~0.20) for good rejection of incident radiation. There are three such radiators - one on the back of each detector and one on the central electronics box. The detector apertures are covered with second surface aluminized mylar heat shields. These insulate the detectors while absorbing a minimum of incident low energy x-rays.

Survival heater power is provided to the electronics of each detector and the central electronics box from the spacecraft main power bus. Each survival heater is governed by a thermostat.

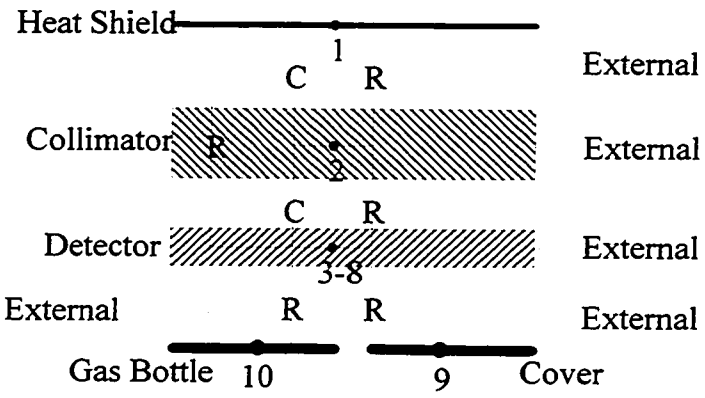

Figure 2.10: USA Detector System Thermal Model

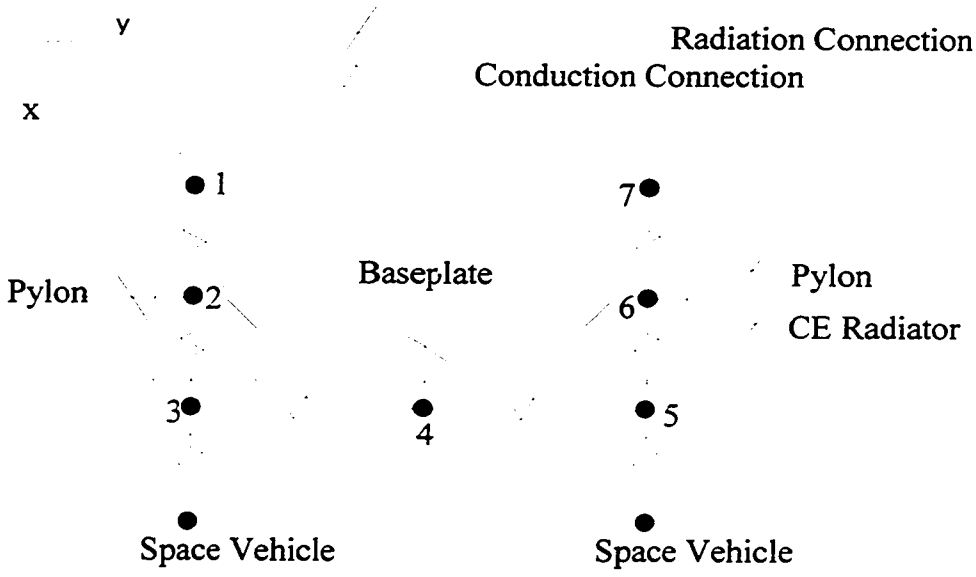

Figure 2.11: USA Pylon/Baseplate Thermal Model

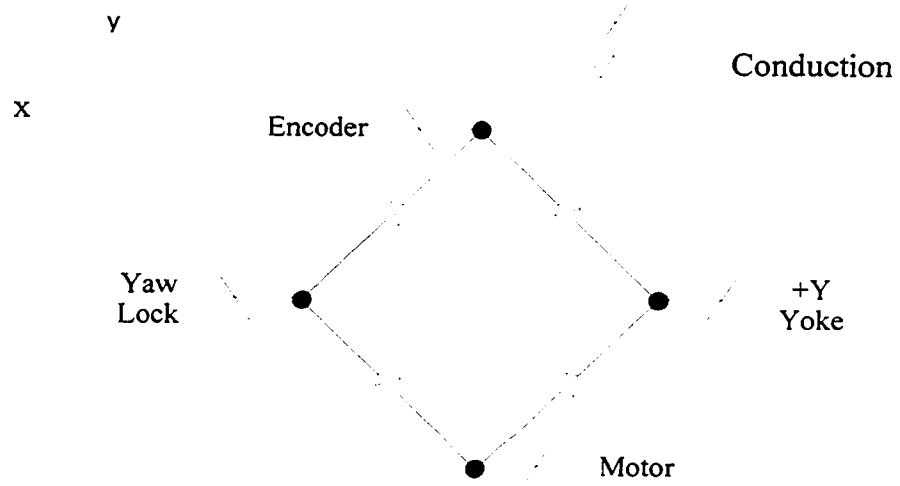

Figure 2.12: USA Yoke System Thermal Model

The pylon/baseplate system was modeled with the following assumptions:

1. The interface resistance between the pylons and the baseplate was neglected in this model. Both pylons are covered in multi-layer insulation with a blackened kapton outer surface.

2. The baseplate is bolted to the space vehicle through eight 3/8 in titanium bolts. The interface resistance of these bolts was modeled by two conductive elements, one on the +Y side of the experiment and one on the -Y side. The baseplate is covered in multi-layer insulation with a blackened kapton outer surface.

3. The central electronic box radiator (CE Box) is integrally attached to the +Y side pylon. Heat dissipated by the electronics in operational and survival modes is assumed to be dissipated directly into the radiator. The external radiator surface is covered with silver teflon tape. Radiative heat

transfer between the bottom of the CE Box and the spacecraft interface was neglected. These surfaces will be covered with low emissivity materials to eliminate such heat transfer. The thermal design for USA used the temperature of the radiator as the design goal for the central electronics box temperature.

4. The pylon/baseplate system is broken into three diffusion and 5 arithmetic nodes.

5. In the calculation of the conductivities between pylon nodes, the area used to calculate the conductivity between two nodes is the average cross-sectional area of the conduction path between those nodes.

A simple model was created to describe the yoke system. It consists of four diffusion nodes representing the four quadrants of the yoke. The entire yoke is covered in MLI and it has no radiators. Again, in order to calculate the conductivity of the yoke between nodes, the average cross-sectional area along the conduction path was used.

The USA detector system, consisting of two proportional chamber subsystems suspended in an aluminum frame, is modeled with the following assumptions:

1. All external surfaces of the proportional chamber and collimator frame are covered with MLI.

2. The aluminum detector cover covers the entire backplane of the detector. The external surfaces are covered with MLI, with the exception of a single patch of radiator area that is covered with silvered teflon tape. The inside of the cover is radiatively coupled to the detector backplane.

3. The gas bottle is completely covered in MLI and contains no internal heat generation. It is connected to the proportional chamber via a small bolted surface.

4. The conductive resistance of the mylar window and heat shield was neglected. All heat absorbed by the window is reradiated as a diffuse gray body.

5. The collimator frame and collimators were lumped together as a single diffuse node. They include a conductive path to the detector body as well as radiative paths between the heat shield and the window.

6. The heat shield was modeled as a second surface reflector with optical properties provided by Swales Associates.

7. The detector body is modeled with five diffusion nodes with conductive and radiative connections between them.

There are three operational modes on the ARGOS satellite - initial deployment, operational and sunsafe. Each of these modes presents a different set of heat inputs and boundary conditions to the USA experiment. In the initial deployment mode (Figure 2.13a), the satellite is in its nominal orbit configuration. The +Z axis is nadir pointed and the X axis is in the velocity direction. The USA detectors and electronics are turned off, but the survival heaters are turned on to keep the temperatures of sensitive components within specifications. Throughout initial deployment the +Y side of the vehicle never sees direct sunlight.

A few weeks into the mission the USA experiment will go from initial deployment mode to operational mode. In this mode the satellite is in the same nominal configuration as in initial deployment, but the experiment is free to rotate inside the pylons. Additionally, the detectors and electronics are turned on. While the power to the

survival heater buses is never turned off, the heaters are controlled by thermostats located on critical USA components. During USA operations, the experiment should never get cold enough for the survival heaters to be turned on.

A special survival or sunsafe mode has been provided on the ARGOS spacecraft (Figure 2.13b). In this mode the satellite configures itself for maximum power generation and minimum power consumption. The satellite is inertially stabilized with the solar arrays pointed directly at the sun. This places the -Z axis 30° off the sunline. The operational power to the experiments is turned off and the survival heaters are left on.

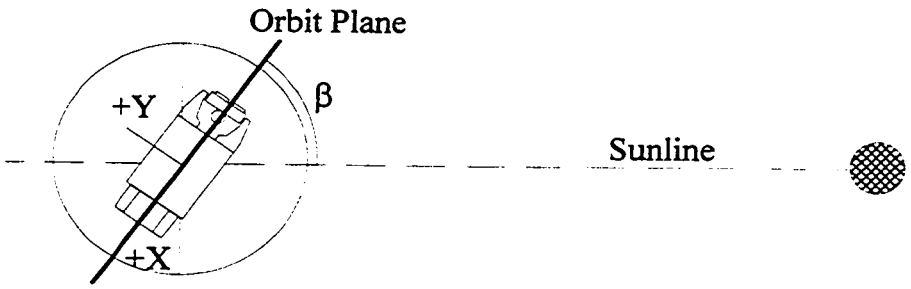

Figure 2.13a: USA Initial Deployment/ Operational Mode

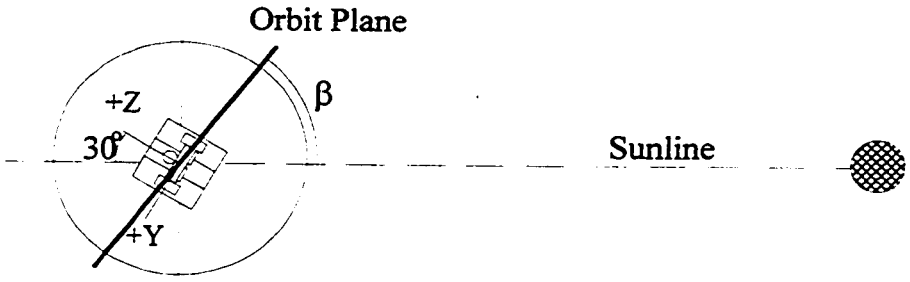

Figure 2.13b: USA Sunsafe Mode

Chapter 3: X-ray Attitude Determination

3.1 Introduction

The orientation of a spacecraft relative to an inertial frame commonly referred to as the celestial sphere can be determined by measuring the location of one or more guide stars in the spacecraft frame. It is common practice to make these observations using instruments sensitive to guide star emissions in the optical or ultraviolet light wavelengths. These measurements can also be made by using detectors sensitive to the x-ray light emitted by many of the same guide stars.

Two such instruments will be considered here. An x-ray star mapper takes a single image of a large portion of the sky and locates several guide stars in the image. The pattern of guide stars is compared to an on-board catalog to determine the spacecraft orientation. An x-ray star scanner measures the location of each guide star independently by scanning an x-ray detector over each star successively.

There are several advantages to using the x-ray sky as an inertial reference. The small number of bright sources emitting in the x-ray regime means that the number of stars in an on-board catalog need not be very large. This results in a reduction in the

instrument memory requirements needed to store the catalog. The instrument computing requirements are also reduced since the complexity of the image matching routine is lessened. The complexity of an x-ray star scanner is also reduced since fewer bright sources generally means less source confusion. Additionally, the temporal variabilities (pulsations) that are present in the intensities of many x-ray sources can be used during attitude initialization to identify a crude pointing direction. This can also be used during the image matching process to explicitly identify specific sources in an image, further reducing the complexity of the image matching process.

3.2 X-ray Star Mappers on Pointed Satellites

3.2.1 Missions and Methodologies

Star mappers have traditionally been used for missions where pointing knowledge requirements are very strict - as tight as arc-second resolution. Recent designs of these instruments have involved using a lens system and a planar CCD array to image the optical or ultraviolet star field in detector coordinates. A comparison of bright sources in the image to a catalog of guide stars by one of several image matching algorithms results in a measure of the inertial attitude of the spacecraft. A great deal of effort has been put into developing efficient image matching routines. These generally involve measuring the angular displacements in the image between pairs or triplets of guide stars. These measurements are then compared to the known angular displacements between a large number of guide stars to determine the orientation of the spacecraft (van Bezooijen, 1992). The high performance of these instruments is accompanied by several drawbacks. They tend to be expensive, heavy and require a lot of power when compared to other attitude sensors. Furthermore, bright sources other than the guide stars (sun, earth, moon) can introduce errors in the measurement process. The image system can even be damaged if care is not taken to keep such sources from shining directly on the collecting area of the instrument. This generally involves placing a large sun shield in front of the star mapper to limit its field of view and constraining the attitude motion of the vehicle to

keep bright sources from passing in front of the sensitive instrument. The detectors used to collect x-rays can operate effectively in such harsh environments and can withstand very high count rates (e.g. from the sun) without being permanently damaged (electronics sensitive to high count rates can be shut off before damage occurs). X-ray star mappers can be used without special constraints on the attitude motion of the spacecraft since they will not be damaged by viewing bright sources.

There are three ways to create an x-ray image:

1. By measuring the direction of each incoming photon directly.
2. By using a lens or mirror system with a position sensitive detector.
3. By using a coded mask with a position sensitive detector.

Detectors capable of measuring the direction of a photon directly are effective at detecting only high energy x-rays and γ-rays. The low count rates associated with sources at such energies makes them undesirable for use as an inertial pointing reference. The collecting area required for a reasonable signal-to-noise ratio and measurement bandwidth would be quite large (i.e. tens of square meters).

Grazing incidence mirrors have been used in conjunction with position sensitive x-ray detectors to image the x-ray sky. While an instrument with grazing incidence mirrors and a pixelated detector offers a direct and continuous image of the x-ray sky, these mirrors tend to be large, heavy and expensive.

Using coded masks to image the x-ray sky was first proposed by Dicke in 1961 (Dicke, 1961). These systems use a pixelated detector with a mask that has a pseudorandom pattern of holes in it. The image returned by the detector is then a convolution of the actual x-ray sky and the coded mask pattern. The literature on the design of these masks is quite extensive (Fenimore, 1978; Massen, 1987). A number of reconstruction schemes have been demonstrated for deconvolving the detector image into an image of the x-ray sky (Skinner, 1984). This image can then be compared to an on-board catalog of x-ray guide stars with the same methods as those developed for optical star mappers. While these instruments are relatively easy to manufacture, they do have

one drawback. The process of deconvolving the detector image introduces errors in the reconstructed image that would not be present when using direct imaging systems. Typically, these errors appear as ghost images and are due to the fact that there are an infinite number of solutions to the reconstruction problem.

3.2.2 Pointing Feasibility Study

In order to show that an x-ray star mapper can be used as a precision pointing instrument, a simple x-ray imaging system is considered. This instrument is based on a proposal by Dr. Kent Wood for an x-ray imaging system called the Silicon Imaging X-ray Instrument (SIXI) that will demonstrate the performance of an x-ray star mapper as a precision attitude reference. The resolution of this instrument is fairly moderate at 0.05° and its collecting area is roughly 0.36 m on a side. The SIXI mission will use a coded aperture system to generate the images. Assuming a coded mask that occludes 50% of the detector area, the effective collecting area of this instrument is reduced by a factor of two to 0.0648 m^2 (648 cm^2). Such an instrument could be used on an inertially pointed or slowly spinning (e.g. nadir pointing) spacecraft. The following assumptions are made in this analysis:

1. An x-ray imaging device is considered.
2. An image of the sky is taken in x-rays without imaging errors. In reality there will be errors (ghosts, blurring) in the image associated with imperfect lenses or the coded aperture reconstruction.
3. It is assumed that the jitter or spin of the satellite that occurs while taking an image is less than the resolution of the detector.
4. A simple attitude determination algorithm is used and will be discussed later.
5. The x-ray sources are assumed to be point sources. A few x-ray sources actually behave as diffuse sources several arc-seconds across.

6. The image is "taken" with an instrument with the same effective energy response as the HEAO-A1 instrument. That is, it is sensitive to photons with energies between 1 keV and 30 keV.

7. The HEAO-A1 catalog is assumed to be a complete and accurate representation of the x-ray sky. A map of the x-ray sky corresponding to the sources in this catalog is shown in Figure 3.1.

8. The number of counts in the image bin corresponding to a particular source are defined by a Poisson distribution with a mean corresponding to the source intensity as indicated in the HEAO-A1 catalog.

9. The instrument configuration is assumed to be similar to the SIXI mission. The relevant parameters are summarized in Table 3.1.

Field of View	Cone with 40° half angle
Attitude Solution Error Box	Cone with 2.5° half angle
Bin Resolution (Size)	0.05° x 0.05°
# Solution Bins (n)	10,000
Energy Range	Approximately HEAO-A1
Detector Area	648 cm^2
Background Rate	30 counts/(sec* cm^2) whole sky

Table 3.1: Ideal Detector Parameters

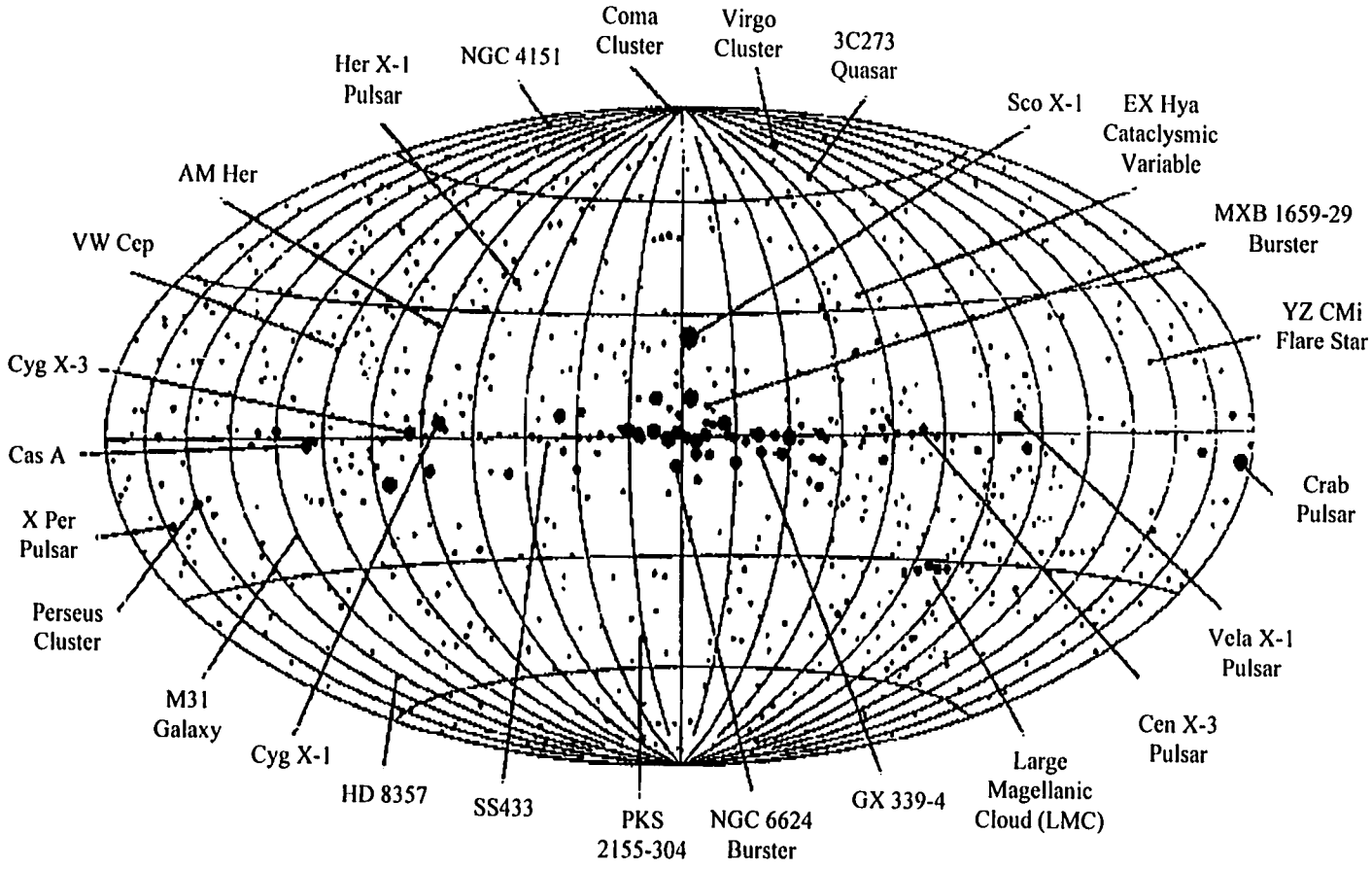

Figure 3.1: HEAO-A1 X-ray Sky Map

The attitude determination algorithm used in this study is as follows (see Figure 3.2):

1. Assume that an attitude fix has been made at time t_0.
2. Predict the attitude at time $t_1 = t_0 + \Delta t$ by some form of forward integration. This gives an expected field of view for the x-ray star mapper.
3. Search the on-board catalog for the brightest x-ray source in the expected field of view. This is the guide star.
4. Estimate the maximum possible error in the attitude prediction at time t_1. This gives the attitude solution error box that is centered about the guide star.
5. Collect x-ray photons for t_e seconds to create an image of the x-ray sky.
6. Search the region of the x-ray image corresponding to the attitude solution error box for the brightest source in that box. If the exposure time is sufficiently long, the probability of a background bin in the image having more counts than the guide star bin is negligible.
7. The possibility of source confusion is neglected. It is assumed that a more complex algorithm can be used to alleviate this problem.
8. The position of the guide star in instrument coordinates can then be compared to the inertial position of the guide star from the on-board catalog to get an inertial attitude fix at time t_1.

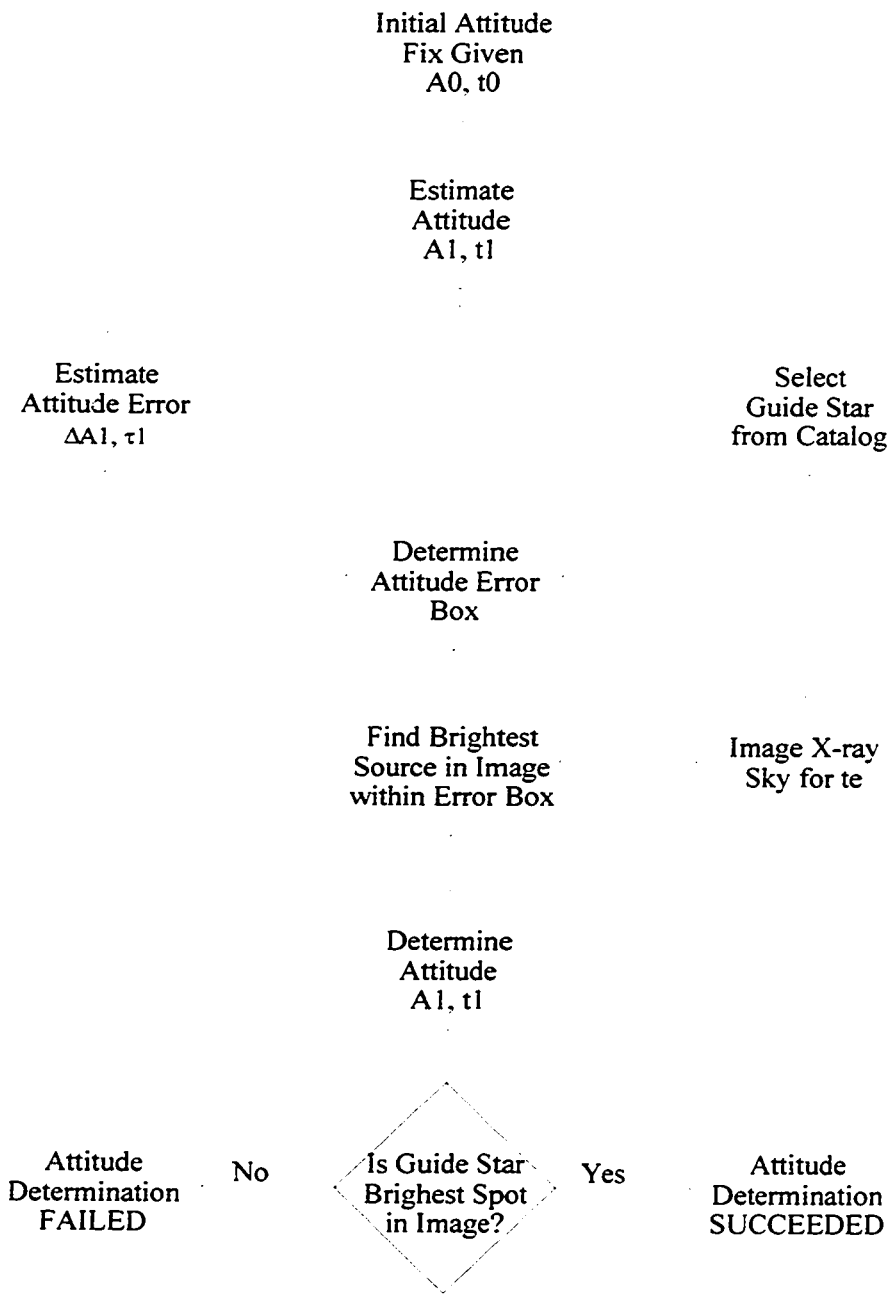

Figure 3.2: X-ray Star Mapper Feasibility Study

The problem then is to compute the exposure time necessary to guarantee (to an acceptable probability) that the guide star will be the brightest source in the attitude solution error box. If the image of the sky is divided into a number of equal bins, then the number of counts in any bin is given by a Poisson distribution. Defining X to be the number of counts in the bin containing the guide star and Y_i to be the number of counts in the i^{th} background bin, the number of counts in any bin are given by:

$$P(X=k)=e^{-\mu_s A t_e}\frac{(\mu_s A t_e)^k}{k!} \qquad \text{(guide star bin)} \qquad (3.2.1)$$

$$P(Y_i=l)=e^{-\mu_b A t_e}\frac{(\mu_b A t_e)^l}{l!} \qquad (i^{th}\text{ background bin}) \qquad (3.2.2)$$

where, μ_s = Mean rate of guide star (counts/sec*m^2)
μ_b = Mean rate of background (counts/sec*m^2)
A = Instrument effective collecting area (m^2)
t_e = Instrument exposure time (sec)

The probability of successfully determining the attitude is the probability that the image bin of the guide star contains more counts than any other bin in the solution error box (n bins total in the solution error box). That is,

$$P(S) = P(\text{success}) = P(\text{X is maximum}) \qquad (3.2.3a)$$

$$P(S)=\sum_{k=1}^{\infty}P(X=k)P(y_1<k)P(y_2<k)\ldots P(y_{n-1}<k) \qquad (3.2.3b)$$

$$P(S)=\sum_{k=1}^{\infty}P(X=k)\left[P(y<k)\right]^{n-1} \qquad (3.2.3c)$$

$$P(S)=\sum_{k=1}^{\infty}P(X=k)\left[\sum_{l=0}^{k-1}P(y=l)\right]^{n-1} \qquad (3.2.3d)$$

$$\boxed{P(S)=\sum_{k=1}^{\infty}e^{-\mu_s A t_e}\frac{(\mu_s A t_e)^k}{k!}\left[\sum_{l=0}^{k-1}e^{-\mu_b A t_e}\frac{(\mu_b A t_e)^l}{l!}\right]^{n-1}} \qquad (3.2.4)$$

This equation can be solved numerically for t_e given a series of source strengths, μ_s, a desired probability of success (in this case, P(S)=99.7%), and the instrument parameters given in Table 3.1. The relationship between guide star intensity and required exposure time is plotted in Figure 3.3. This information is then used in conjunction with the HEAO catalog to generate a contour plot of the exposure time necessary to achieve an attitude solution as a function of the pointing direction of the x-ray star mapper (Figure 3.4). The abscissa and ordinate in Figure 3.4 correspond to the galactic longitude and galactic latitude of the instrument boresight during a given observation. For each observation, the HEAO catalog is searched for the brightest source in the instrument field of view and it is selected as the guide star as previously discussed. The intensity of the guide star (μ_s) is corrected for the effect of reduced detector area when the photons from the guide star impacted the detector at an angle by multiplying by the cosine of the angle between the instrument boresight and the line of sight to the guide star.

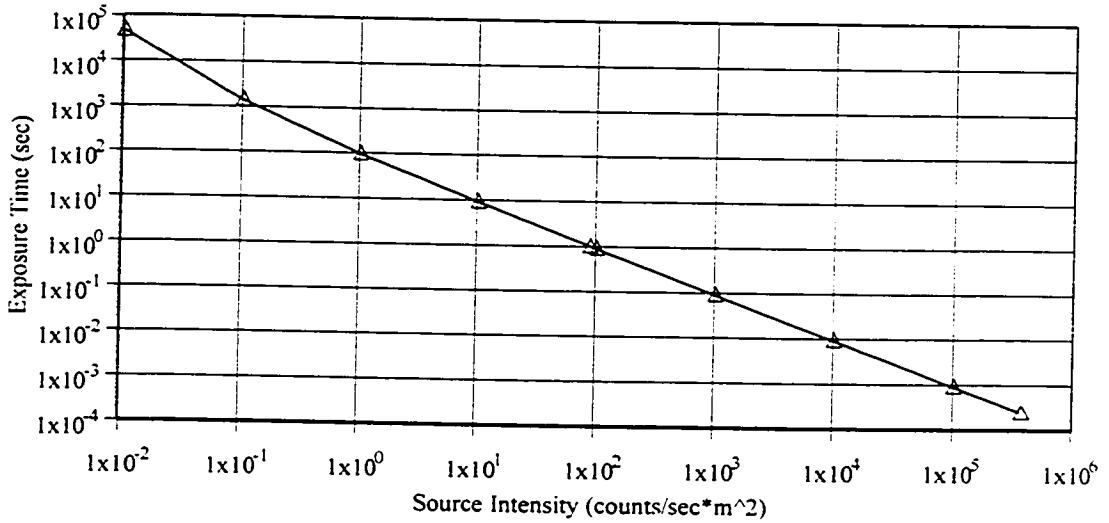

Figure 3.3: Ideal Star Mapper Sensitivity

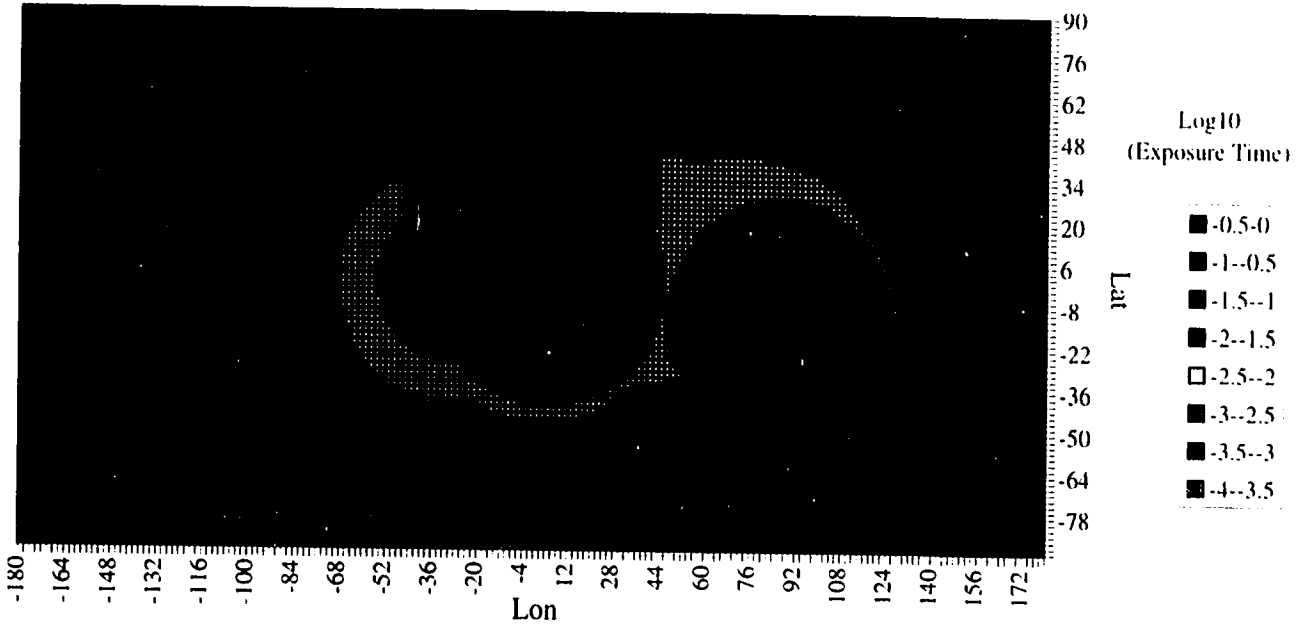

Figure 3.4: Ideal Star Mapper Exposure Time

The results of this study suggest that for an x-ray star mapper with characteristics similar to the SIXI instrument, a minimum exposure time of about 1 msec will be necessary when the brightest guide star (Sco-X1) is in the field of view. The required exposure time increases to about 10 sec in areas where the guide stars are fainter. Note that the exposure time necessary to make a measurement is inversely proportional to the collecting area of the instrument. Thus, by doubling the instrument area, the exposure time can be cut in half, doubling the bandwidth of the instrument. The bandwidth of the attitude determination system can also be increased by using more than one instrument, each pointed in a different direction. When one instrument is looking at a portion of the sky where the guide stars are dim, the other instrument will see brighter guide stars allowing it to make measurements at a faster rate.

3.3 X-ray Star Scanners on Spinning Spacecraft

Spacecraft that spin about their maximum principal axes of inertia fill an important role in the design of spacecraft. These vehicles have two advantages: the location of the spin axis is relatively stable in inertial space and the spinning action of the spacecraft makes it an excellent scanning platform for observations of the earth and space. The stability of the spin axis makes this an inexpensive way of stabilizing a satellite when compared to a satellite that is controlled about all three axes. Measuring the attitude of a spinning satellite has been done with combinations of sun sensors, earth horizon sensors, star scanners and gyroscopes.

Using an x-ray star scanner is an excellent way to make accurate measurements of the orientation of a spinning spacecraft. This instrument is of simple design, consisting of a detector and a collimator and some associated electronics. The detector records the number of photons from the guide star as a function of time. The collimator attenuates the guide star intensity as a function of the orientation of the spacecraft. This effect is called the collimator transmission. The spinning action of the spacecraft causes the detector to "map" the collimator transmission as a function of time, making it possible to

determine the orientation of the spacecraft. The sparsity of celestial objects radiating brightly in the x-ray regime makes an x-ray star scanner very appealing for use on spinning spacecraft. A star scanner has the advantage that the spinning action of the spacecraft causes guide stars to come into the field of view (FOV) of an instrument that has a relatively small inherent field of view. The FOV is effectively 360 degrees in the spin direction (normal to the spin axis). Instruments on satellites in planetary orbits would be limited to something less than a 360 degree FOV by the presence of the planet, but would certainly have a FOV greater that 180 degrees. Thus, the high signal to noise ratios associated with a small FOV instrument will be available to an instrument with a large FOV. The small number of potential guide stars (<100) minimizes the potential for two guide stars to be in the instrument FOV simultaneously, thus minimizing the possibility of source confusion.

3.3.1 Instrument Fundamentals

Instruments used to detect x-rays are capable of measuring the time of arrival and the energy of a photon entering the detector. Some of these instruments (pixelated proportional chamber, silicon strip detector) also return the location of the photon hit on the detector. No information is available as to the direction the photon was traveling when it impacted the detector. But in order to use these photons to specify a direction to a target source, it is necessary to measure the direction a photon is traveling as it impacts the detector.

One way to determine the direction a photon is traveling is to place a collimator in front of the detector to limit its field of view. Any photon recorded by the detector then came from a small section of the sky defined by the collimator. In its simplest form a collimator can be a tube with walls dense enough and thick enough to block the path of photons incident upon them. A detailed analysis of the performance of collimators is given in Appendix D and outlined below.

Consider the two dimensional collimator shown in Figure 3.5. An arriving x-ray photon is constrained to move in a plane and is incident on the detector surface at an

angle α. Before the photon reaches the detector, it must pass between the two collimator walls. The collimator shadows the detector, reducing its effective length. The effective length of the detector is reduced from L_0 to L by this shadowing effect and by the fact that the x-rays are incident on the detector at an angle.

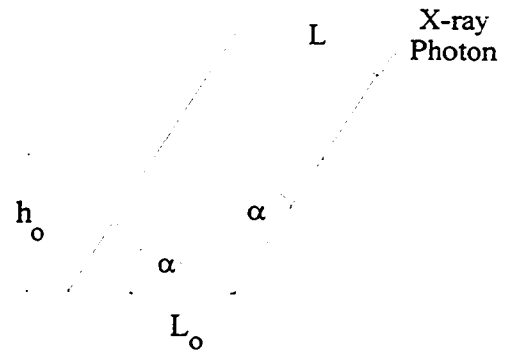

Figure 3.5: Two Dimensional Collimator Geometry

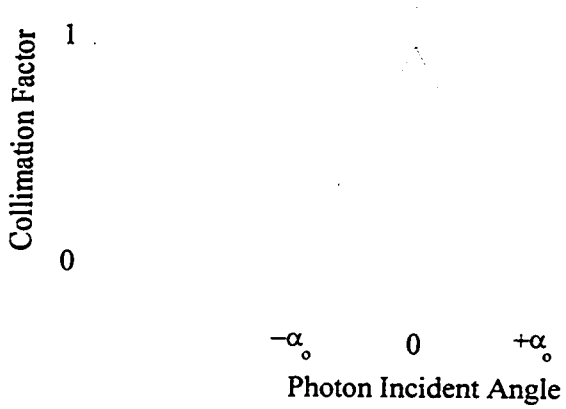

Figure 3.6: Ideal Two Dimensional Collimator Transmission

The effectiveness of a two dimensional collimator can be described by a single parameter, T_C that is a function of the incident angle, α, and the instrument geometry:

$$T_C = \left(1 - \frac{\tan|\alpha|}{\tan(\alpha_o)}\right)\cos(\alpha), \qquad |\alpha| \le \alpha_o \qquad (3.3.1a)$$

$$T_C = 0, \qquad |\alpha| \ge \alpha_o \qquad (3.3.1b)$$

$$\text{where,} \quad \tan(\alpha_o) = \frac{h_o}{L_o} \qquad (3.3.1c)$$

α_O is called the "full-width-half-max" of the detector and is also one half the instrument field-of-view.

For a collimator with a very narrow field-of-view (small α_O), this parameter can be approximated by,

$$T_C = \left(1 - \frac{|\alpha|}{\alpha_o}\right), \qquad |\alpha| \le \alpha_o \qquad (3.3.2a)$$

$$T_C = 0, \qquad |\alpha| \ge \alpha_o \qquad (3.3.2b)$$

This simplified expression is the equation for a triangle with base $2\alpha_O$ and height 1 centered at α=0. The collimator transmission, T_C is shown as a function of the incident angle, α in Figure 3.6.

A simple three dimensional collimator can be constructed from one, or a series of, rectangular tubes, open on each end to allow for the passage of x-rays. The transmission of such a collimator can be modeled as if it is independent in two orthogonal directions. These orthogonal directions are called the principal directions of the collimator. The overall transmission is simply the product of the transmission of two two-dimensional collimators oriented orthogonally, viz.:

$$T_C = \left(1 - \frac{\tan|\rho|}{\tan(\rho_0)}\right)\cos(\rho)\left(1 - \frac{\tan|\alpha|}{\tan(\alpha_0)}\right)\cos(\alpha) \qquad (3.3.3)$$

A contour plot of the transmission of such a collimator is shown in Figure 3.7. Note that the zero transmission lines (lines that define the instrument FOV) form a square. Lines of constant transmission are hyperbolae with asymptotes that are the zero transmission lines.

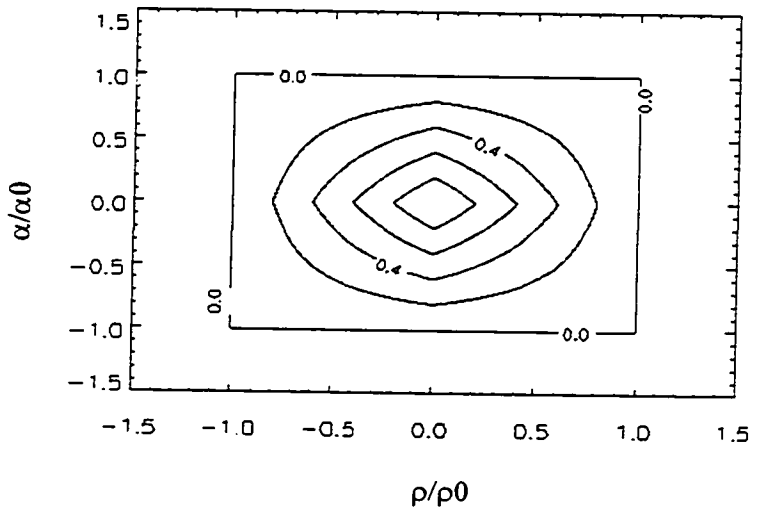

Figure 3.7: Ideal Three Dimensional Collimator Response

3.3.2 General Star Scanner Description

A series of simple x-ray star scanners can be constructed by combining a rectangular collimator with an x-ray detector. The collimator must be oriented such that the detector line of sight is perpendicular to the spin axis and one of the detector principal axes is parallel to it. These directions must be known before the instrument is used as an attitude reference. As the spacecraft rotates, x-ray sources will come into the collimator field of view. A scan over the guide star is created by counting the photons and placing them in bins of constant elapsed time. If the spin rate and source intensity are constant during the scan, the number of counts recorded in each bin over a scan will map the

triangular response of a two dimensional collimator. By matching the known transmission of the collimator to the shape of the scan, the orientation of the satellite can be determined.

In order to describe the operation of an x-ray star scanner it is necessary to describe the apparent motion of a guide star in the instrument frame of reference as a function of time. A complete derivation of the related equations of motion is included in Appendix E and summarized here. This model will be called the First Order Star Scanner Model.

First, several coordinate systems must be defined:

Celestial Coordinates - Inertially fixed frame. Denoted (X_c, Y_c, Z_c), the X_c axis points to galactic north while the Y_c axis is in the direction of the first point of Aries.

Guide Star Coordinates - Inertially fixed frame. A guide star is defined by its position in celestial coordinates. This position is given by the right ascension of the ascending node (RA) and the declination (DEC) of the star. First, a rotation through RA about the X_c axis to a set of coordinates (X', Y', Z') is performed. A rotation through DEC about the Z' axis to the guide star coordinates (X, Y, Z) is then made. This places the Y axis pointing directly at the guide star. Derivation of all equations of motion will take place in the Guide Star inertial frame.

Spacecraft Coordinates - Body fixed frame. The spacecraft coordinates are in the principal directions of the inertia tensor. The y-axis points nominally out the instrument face. The z-axis is in the nominal spin direction. This system is defined by the unit vectors (x,y,z).

Instrument Coordinates - Body fixed frame. The y_i-axis is in the direction of maximum instrument transmission. The x_i-axis defines the pitch axis of the instrument. The z_i-axis defines the roll axis of the instrument. This coordinate system can be defined by in terms of the Spacecraft Coordinates by three euler rotations (δ_x, δ_y, δ_z).

The attitude motion of the spacecraft can be divided into two categories: torque free motion and forced motion. The forced motion is governed by the Euler Equations:

$$T_x = I_{xx}\dot{\omega}_x + (I_{zz} - I_{yy})\omega_y\omega_z \qquad (3.3.4a)$$

$$T_y = I_{yy}\dot{\omega}_y + (I_{xx} - I_{zz})\omega_x\omega_z \qquad (3.3.4b)$$

$$T_z = I_{zz}\dot{\omega}_z + (I_{yy} - I_{xx})\omega_y\omega_x \qquad (3.3.4c)$$

These equations are written in the body fixed spacecraft coordinate system. The torque free or polhode motion of the vehicle can be described by:

$$0 = I_{xx}\dot{\omega}_x + (I_{zz} - I_{yy})\omega_y\omega_z \qquad (3.3.5a)$$

$$0 = I_{yy}\dot{\omega}_y + (I_{xx} - I_{zz})\omega_x\omega_z \qquad (3.3.5b)$$

$$0 = I_{zz}\dot{\omega}_z + (I_{yy} - I_{xx})\omega_y\omega_x \qquad (3.3.5c)$$

While spin stabilized spacecraft are designed to have an inertially stable spin axis, there will always be some polhode motion and some forced motion present. As described in Appendix E, this motion causes the guide star to travel a complex path in instrument coordinates. Fortunately, if we assume that the period of the polhode motion is long when compared to the spin period of the satellite and that the spin axis is always close to the desired spin axis and that the misalignment of the instrument relative to the spacecraft is small, it can be shown that the guide star will track a simple path over the instrument.

The collimator parameters, ρ and α, can be written in terms of the motion of the spacecraft, viz.:

$$\rho = -(\Omega t + \delta_z) \tag{3.3.6a}$$

$$\alpha = -(\theta(0) + \delta_x) \tag{3.3.6b}$$

Note that during a scan the pitch angle to the guide star (described by α) is a constant and that the roll angle (described by ρ) is linear with time. The transmission of the collimator can then be written as a function of time, viz.:

$$T_c(\alpha, \rho) = T_\alpha(-\theta(0) - \delta_x)T_\rho(-\Omega t - \delta_z) \tag{3.3.7}$$

The rolling motion of the vehicle causes the scan to be triangular shaped while the constant pitch angle defines the height of the peak.

Given the basic configuration of a detector, rectangular collimator and some electronics, there are three basic types of x-ray attitude measurement instruments that can be defined:

1. X-ray spin rate sensor
2. Single collimator x-ray star scanner
3. Differential collimator x-ray star scanner

3.3.3 X-ray Spin Rate Sensor

A simple x-ray spin rate sensor can be constructed by simply measuring the time it takes for a guide star to pass through the FOV of the collimator. The spin rate of the satellite is directly proportional to the length of time required for the source to pass through the FOV. That is, it is proportional to the width of the triangle base. This instrument consists of the following components:

1. A collimator to define the field-of-view of the instrument.
2. A detector to count the photons passing through the collimator.
3. A threshold to indicate the presence of a guide star in the FOV and trigger the signal processing software.
4. Signal processing circuitry to fit collimator functions to selected scans to determine the spin rate of the satellite.

This instrument offers the following advantages:

1. The number of celestial sources radiating in x-rays is large enough to provide a number of candidates (~100) for making the measurement, but small enough to minimize the problem of source confusion (vis-à-vis optical observations).
2. Measuring spin rate does not require knowledge of which source is being observed or of the spin phase. This reduces the need for on-board computation.
3. Using a collimator and solid-state detector provides for a durable, yet easily manufactured instrument. No optics or precision machining are required.
4. To first order, the measurement of spin rate is immune to calibration errors in the alignment of the collimator and the measurement of the gain of the detector.
5. A single, small detector can be used to measure this quantity.

3.3.4 Single Collimator X-ray Star Scanner

An x-ray star scanner uses all of the information present in a scan to determine the orientation of the spacecraft. It is apparent from equation 3.3.7 that there is sufficient information in a scan to determine the roll angle and pitch angle of the spacecraft in guide star coordinates. This is in addition to the roll rate measurement as described above. If the guide star associated with the scan can be identified, two of the three angles defining the orientation of the spacecraft relative to the celestial sphere can be determined. This can be done either from a priori information (e.g. a previous attitude fix) or by observing the temporal characteristics of the guide star as it passes through the FOV. For the purposes of this discussion, the process of identifying the guide star is assumed to be handled separately from the process of determining the orientation of the vehicle. It is apparent, however, that the operation of this instrument will require a limited catalog of guide stars and their celestial coordinates to be kept on-board. A simple drawing of this instrument is given in Figure 3.8a.

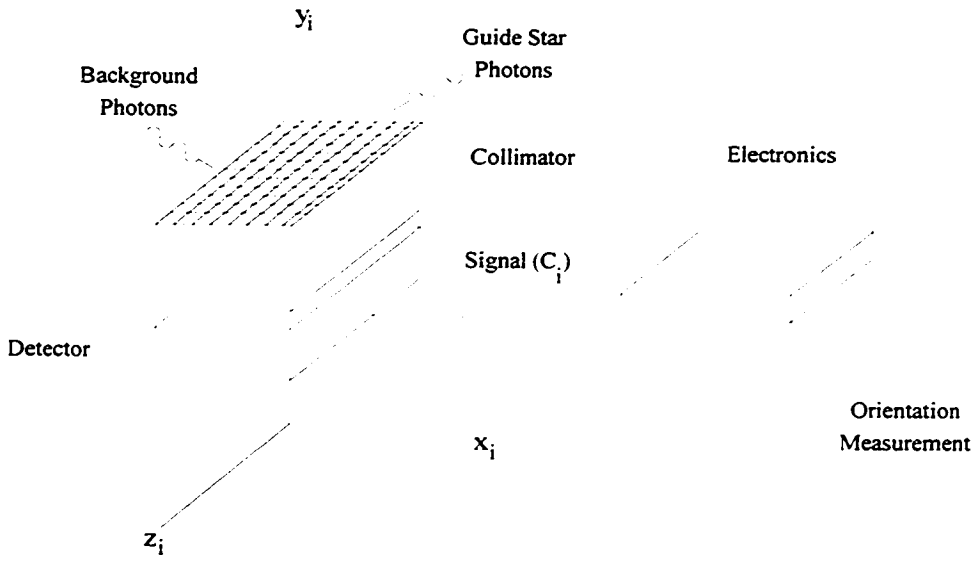

Figure 3.8a: Single Collimator X-ray Star Scanner Geometry

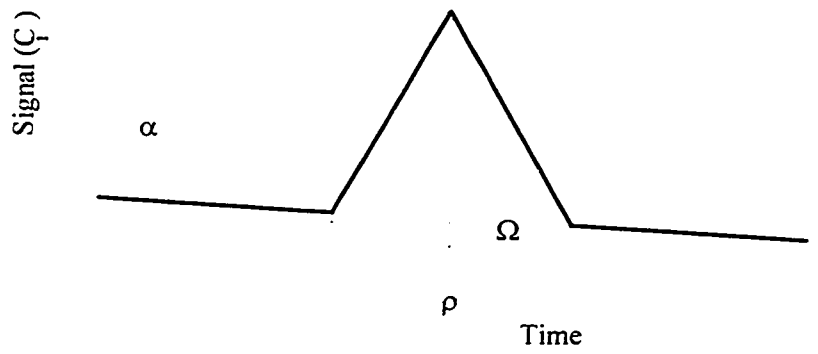

Figure 3.8b: Single Collimator X-ray Star Scanner Response

The measurement process can be described in terms of the number of photons present in a given bin, Y_i, during a scan, viz.:

$$Y_i = AB_i + RA\left(1 - \frac{\tan|\theta(0) + \delta_x|}{\tan(\alpha_0)}\right)\cos(\theta(0) + \delta_x)\left(1 - \frac{\tan|\Omega t_i + \delta_z|}{\tan(\rho_0)}\right)\cos(\Omega t + \delta_z) \tag{3.3.8}$$

where, A = Detector Area
B_i = Background Count Rate
R = Guide Star Intensity

Each scan over a known guide star will give two pointing measurements - the roll angle and the magnitude of the pitch angle (Figure 3.8b). At the time when the peak collimator transmission occurs, the line of sight to the guide star, the collimator normal and the spin axis all lie in the same plane. The sign of the pitch angle and the angle defining a rotation about the line of sight to the guide star are unobservable. By scanning over two sources successively the complete state of the satellite can be determined - with the exception of the pitch sign, which is still unobservable. The primary shortcoming of this instrument lies in its need for an a priori measurement of the guide star intensity.

While a catalog of known intensities can be kept on board, a majority of the x-ray sources show significant temporal variability in their intensities. This variability will lead directly to errors in the pitch angle measurement.

3.3.5 Differential Collimator X-ray Star Scanner

The need for an a priori estimate of the guide star intensity presents a major limitation to the performance of an x-ray star scanner. By using two collimated detectors to produce a differential signal, it is possible to measure the "pitch" of the satellite spin-axis relative to a target source and do so independent of the source intensity. This is in addition to a measurement of the spin phase and rate. To produce the necessary differential pitch signal, the two detectors must be oriented such that a guide star passing into the field of view of the detectors appears at a different pitch angle to each. That is, the instrument coordinates of the two detectors must be offset in pitch (δ_x) relative to one another. The differential signal of the scans from each detector is a measure of the pitch angle and is independent of the instantaneous intensity of the guide star. The sign of the pitch angle becomes observable as well.

There are two basic design approaches to this type of x-ray star scanner. The first approach uses two completely independent instruments, each with its own collimator, detector and electronics (Figure 3.9a). The two independent signals then provide enough information to determine the spacecraft orientation as previously described (Figure 3.9b). Alternately, a single detector can be used with two independent collimators to provide the two signals (Figure 3.10a). One collimator is canted in the pitch direction by $+\delta_x$ degrees, while the other collimator is canted by $-\delta_x$ degrees. In order to separate the two signals (one detector, two collimators) they must appear sequentially in time (Figure 3.10b). This can be done by canting the collimators apart in the roll direction as well (δ_z). If the collimators are not canted apart, the signal from the instrument will be the sum of the two signals rather than two peaks that can be fitted separately.

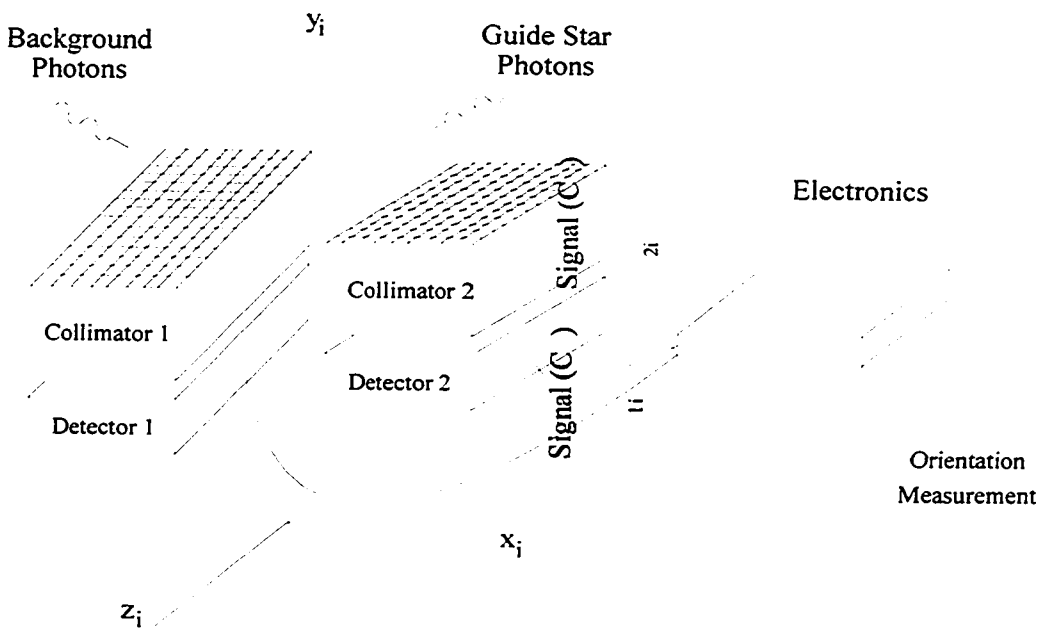

Figure 3.9a: Dual Collimator/Dual Detector X-ray Star Scanner Geometry

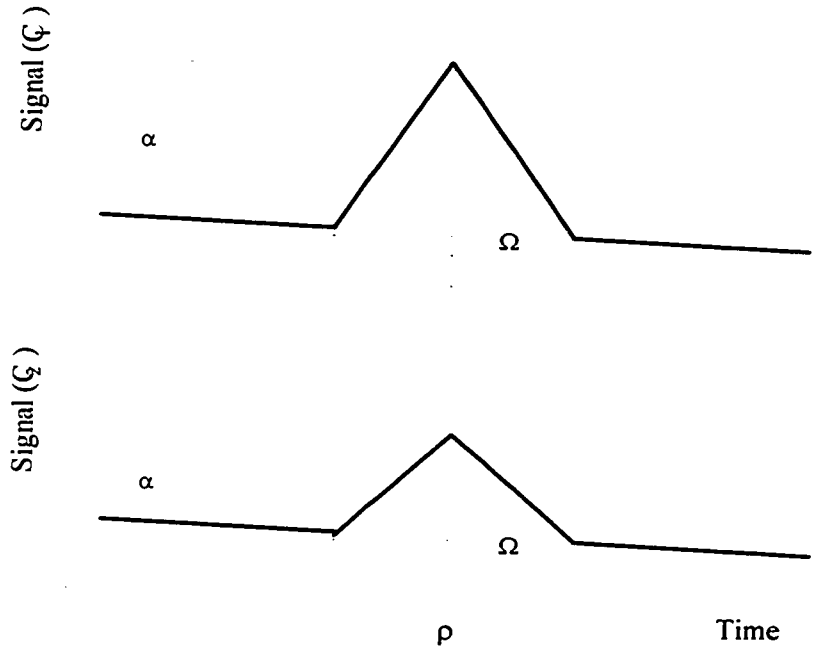

Figure 3.9b: Dual Collimator/Dual Detector X-ray Star Scanner Response

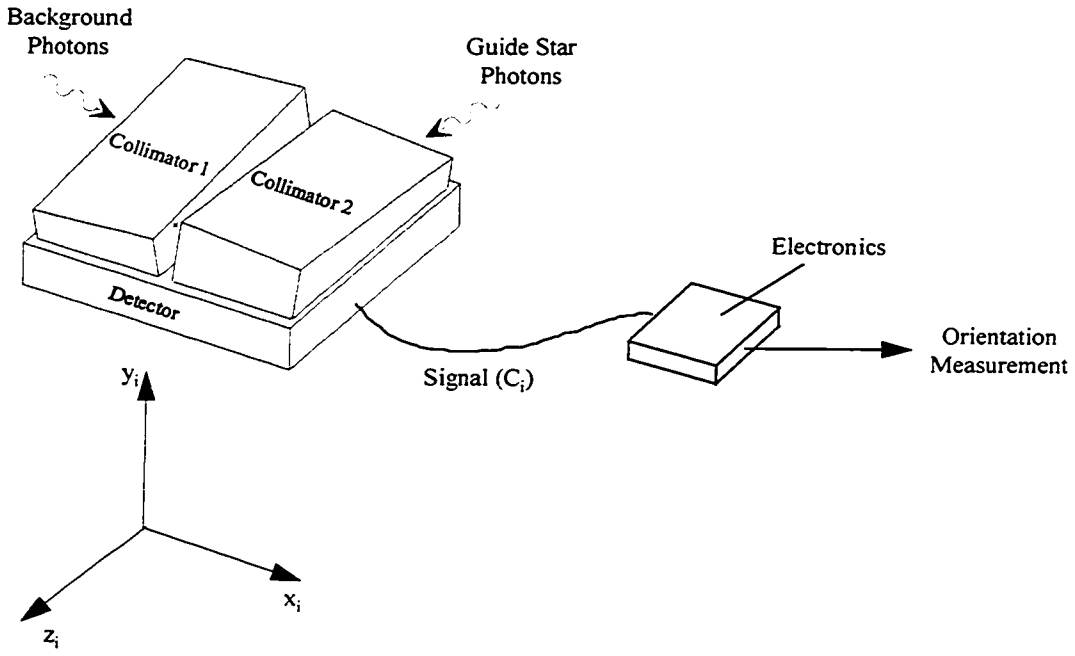

Figure 3.10a: Dual Collimator/Single Detector X-ray Star Scanner Geometry

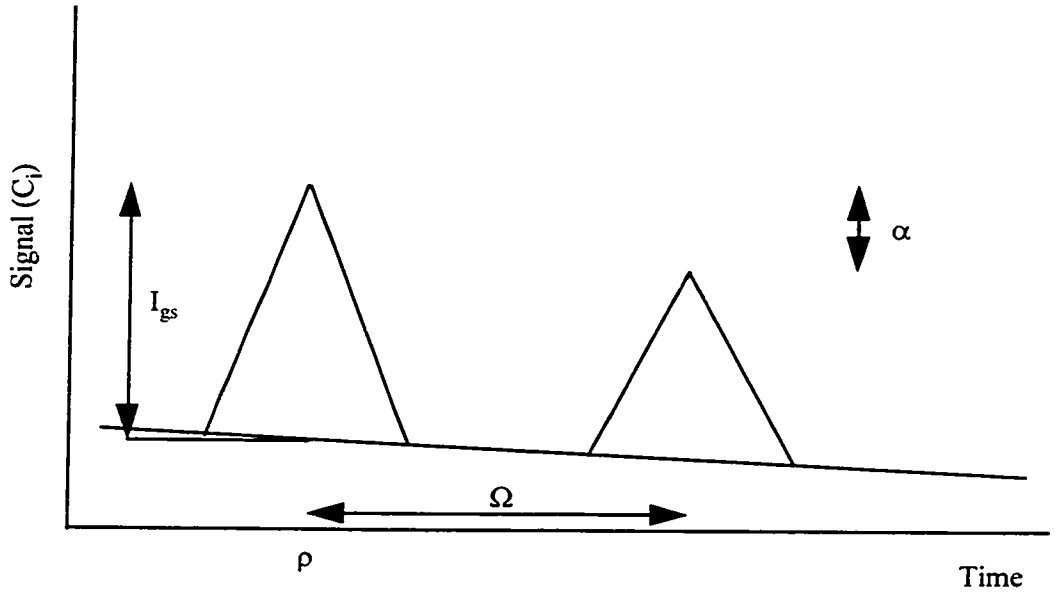

Figure 3.10b: Dual Collimator/Single Detector X-ray Star Scanner Response

A comparison of the performance of a dual instrument versus a single instrument with dual collimators can be performed by examining the relative signal to noise ratios. A crude measure of SNR is the ratio of the average number of counts collected from the source divided by the standard deviation of the number of counts collected due to noise (Poisson fluctuations due to the source and background). The steady background can be removed during the fit routine.

By using two detectors, each with area A, the SNR for one of the detectors would be:

$$Signal = S = A\frac{\rho_o}{\Omega}R$$

$$Noise = N = \sqrt{A\frac{\rho_o}{\Omega}(B+R)}$$

$$SNR_2 = \frac{S}{N} = \sqrt{A\frac{\rho_o}{\Omega}}\frac{R}{\sqrt{B+R}}$$

where, ρ_o = FOV Half Cone Angle in Roll
B = Background Intensity
R = Source Intensity
A = Area
Ω = Roll Rate

(3.3.9a-c)

An equivalent size single detector/dual collimator instrument has double the collecting area of the dual instrument model. But the background intensity is also doubled because there are two collimators feeding the detector. A "collimator packing factor", ($l \leq 1$) is added to account for geometric constraints is placing the dual collimator system on the detector. This will reduce the effective area of the instrument.

$$Signal = S = 2lA\frac{\rho_o}{\omega_s}R \qquad (3.3.10a)$$

$$Noise = N = \sqrt{2lA\frac{\rho_o}{\omega_s}(2B+R)} \qquad (3.3.10b)$$

$$SNR_2 = \frac{S}{N} = \sqrt{2lA\frac{\rho_o}{\omega_s}}\frac{R}{\sqrt{2B+R}} \qquad (3.3.10c)$$

By taking the ratio of the SNR's, the relative performance of these instruments as a function of the guide star and background intensities can be determined, viz.:

$$\frac{SNR_1}{SNR_2} = \frac{\sqrt{\frac{2Al\rho_o}{\omega_s}}\frac{R}{\sqrt{2B+R}}}{\sqrt{\frac{A\rho_o}{\omega_s}}\frac{R}{\sqrt{B+R}}} = \sqrt{2l\frac{1+\frac{R}{B}}{2+\frac{R}{B}}} \qquad (3.3.11)$$

It is apparent then that the single detector/dual collimator approach is superior to the dual detector approach when the ratio of the source strength to the background strength is greater than some function of the detector geometry, viz.:

$$\frac{R}{B} \geq \frac{2(1-l)}{2l-1} \qquad (3.3.12)$$

In fact, if the collimator packing factor is unity, the single detector approach will always yield the superior instrument.

3.3.6 Second Order Star Scanner Model

The operation of an x-ray star scanner as manufactured will not be ideal. The peak of the collimator transmission will not be sharp as manufacturing errors will tend to round this peak off. Additionally, it will have tails where there is a measurable transmission at incident angles greater than the instrument field-of-view - a parameter that itself will not turn out to be exactly the desired value. Thus, it will be necessary to calibrate the collimators used on x-ray star trackers.

Once the collimator has been calibrated, there will be misalignments between the spin axis of the satellite and the orientation of the detector axes. These misalignments may be caused by integration errors in the placement of the collimator detector system or by a misalignment between the spacecraft coordinate system and the actual principal axes of the spacecraft. The polhode motion of the vehicle will also introduce errors in the orientation measurement process. By expanding the First Order Star Scanner Model to include second order small terms we arrive at The Second Order Star Scanner Model. Since this model includes the polhode motion of the vehicle and collimator misalignment

terms, it should be possible to use it to improve the estimate of the instrument attitude from the scanned data. The derivation of this model is presented in detail in Appendix F and summarized here.

To derive the second order model, we follow the derivation of our first order model, neglecting terms that are third order small and smaller. One additional assumption must be made. The spacecraft is assumed to be a body of revolution about the spin axis. The resulting description of the polhode motion in terms of the spacecraft angular velocity in body axes is:

$$\begin{aligned} \omega_x &= \dot{\omega}_1(0)t + \omega_1(0) \\ \omega_y &= \dot{\omega}_2(0)t + \omega_2(0) \\ \omega_z &= \Omega \end{aligned} \qquad \text{(3.3.13a-c)}$$

With the polhode motion (ω_x, ω_y) decoupled from the spin motion (ω_z), these equations can be integrated in terms of the spacecraft euler angles to get the time history of the spacecraft attitude, viz.:

$$\begin{aligned} \phi &= \Omega t \\ \theta &= \theta(0) + \dot{\theta}(0)t \\ \psi &= \psi(0) + \dot{\psi}(0)t - \Omega\theta(0)t \end{aligned} \qquad \text{(3.3.14a-c)}$$

The location of the guide star in instrument coordinates can then be determined by transforming the guide star vector ($\bar{R}_s$) first into spacecraft coordinates and then into instrument coordinates. The transformation from spacecraft coordinates into instrument coordinates accounts for the small, unknown misalignments in the detector orientation (ε_x, ε_y, ε_z). The result is a time history of the guide star location in terms of the collimator angles, viz.:

$$\rho = -(\Omega t + \delta_z + \varepsilon_z + (\theta(0) + \delta_x + \varepsilon_x)(\delta_y + \varepsilon_y)) \qquad \text{(3.3.15a)}$$

$$\alpha = -(\theta(0) + \delta_x + \varepsilon_x) - \dot{\theta}(0)t + (\varepsilon_y + \delta_y)(\Omega t + \delta_z + \varepsilon_z) \qquad \text{(3.3.15b)}$$

There are three possible manufacturing errors in the placement of the collimator:

1. Rotation about spin axis (ε_z)
2. Rotation in pitch direction (ε_x)
3. Rotation about instrument line of sight (ε_y)

There is only one term due to the polhode motion in this model - the pitch rate, $\dot{\theta}(0)$. While the collimator orientation angles (δ_x, δ_y, δ_z) are known parameters, it should be possible to extract some of the misalignment terms and the polhode motion term from scanned data.

3.3.6.1 Rotation about Spin Axis

A misalignment of the collimator about the spin axis (ε_z) will introduce a bias of ε_z in the roll phase measurement. There will be no change in the transmission function of the collimator other than to shift it in roll phase. This misalignment cannot be observed and thus cannot be removed from the measurements.

3.3.6.2 Rotation in Pitch Direction

A misalignment of the instrument in the pitch direction (ε_x about the instrument x-axis) will introduce a bias in the measurement of the spacecraft pitch angle, $\theta(0)$ of ε_x. Again, this misalignment is unobservable and cannot be removed from the measurements.

3.3.6.3 Rotation about Instrument Line of Sight

A misalignment of the instrument about the instrument line of sight (ε_y) will introduce some nonlinearities into the star scanner operations. First, the location of the peak transmission will be shifted by an amount $\theta(0)\varepsilon_y$ in roll. It will also affect the shape of the collimator response function. The presence of this misalignment will cause the transmission of the collimator to be increased/decreased as the peak transmission is

[illegible] The transmission is [illegible] increased as the glint [illegible] moves. The cumulative effect is to make the triangle flatter on one side than the other.

While this term should be observable with a single star, we will see that the presence of noise in the signal makes estimation of it problematic. Note, however, that given two scans of the same guide star (e.g. with a differential star scanner), it should be possible to estimate α_3 based on the two different shifts in the peaks of the two signals.

3.3.6.4 Polhode Motion

The polhode motion of the vehicle will introduce a pitch rate term (β^2) into the second order model. This will have no effect on the roll estimate made by the star scanner. It does, however, change the shape of the collimator response in the same manner as a misalignment of the collimator about its normal. With a single collimator system, this term will add to the α_3 term, making it unobservable as an independent parameter. With a differential star scanner, this parameter can be estimated. This will be demonstrated in Chapter 4.

Chapter 4: HEAO-A1 Attitude Determination Studies

4.1 Introduction

The data from the HEAO-A1 surveys of the x-ray sky provide an excellent opportunity to prove the concept of x-ray attitude determination on spinning spacecraft. The scanning data can be used to demonstrate the performance of both the single detector attitude determination scheme and the differential detector scheme.

4.2 HEAO-A1 Description

As previously described, the HEAO-1 mission (Figure 4.1) contained four experiments, one of which was the Large Area Sky Survey (LASS or HEAO-A1) consisting of seven proportional chambers sensitive to x-rays in the 250 eV to 25 keV range (Wood et al, 1984). All of the detectors were proportional chambers of the same basic design, although the collecting areas and collimators were different on modules 5, 6, and 7. The counting modules had three layers of high voltage wires that provided

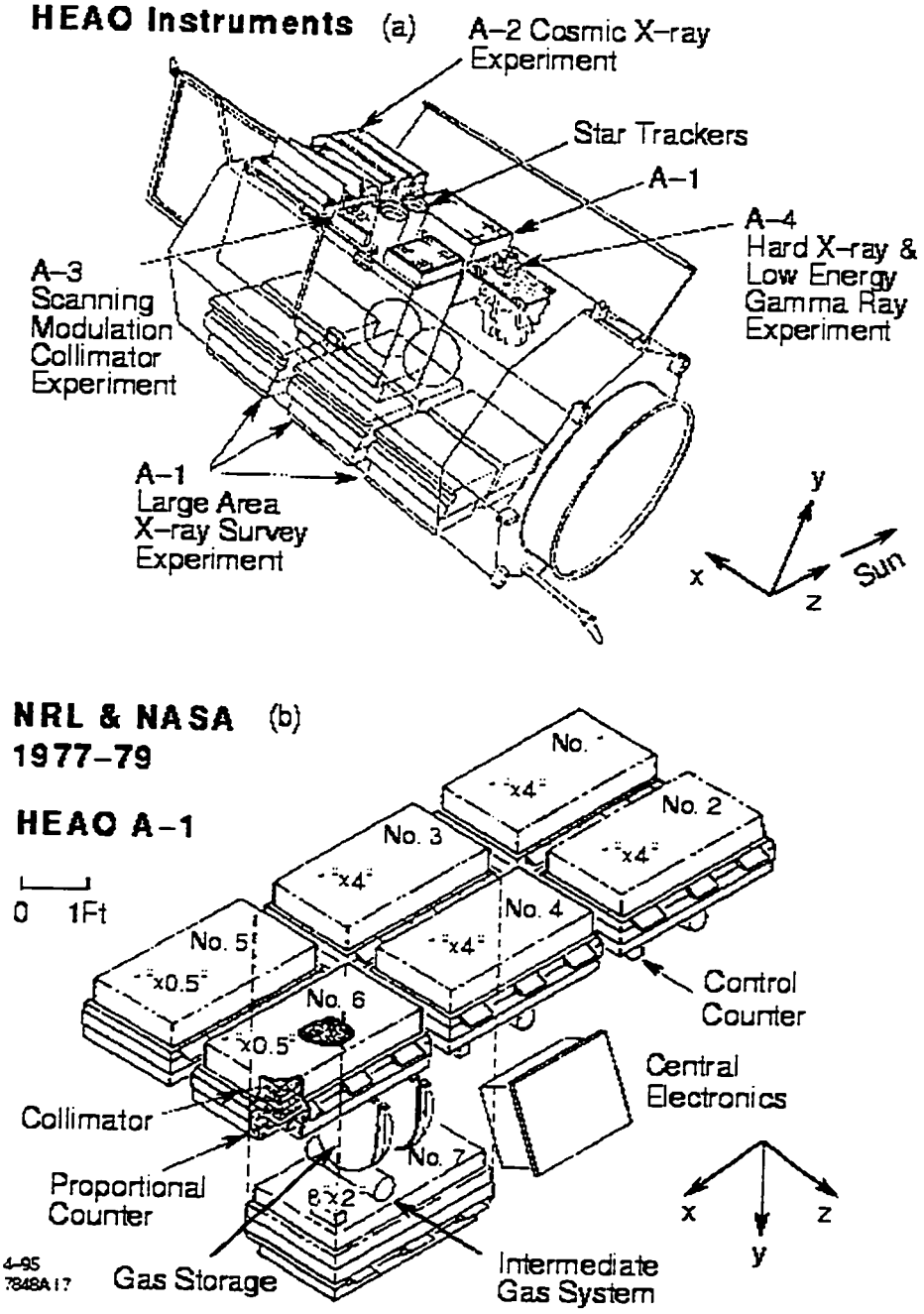

Figure 4.1: HEAO-A1 LASS Mission

counting as well as anticoincidence protection against charged particle events. These detectors operated with a counter gas that was 22% methane and 78% xenon at a nominal pressure of 2 psia. The gas was contained within the counter by the counter body on five sides (opaque to x-rays) and a 2.5 μm Mylar film that was transparent to x-rays above 250 eV on the sixth side. The window was supported against the gas pressure by a rectangular cell honeycomb stainless steel strongback with a stainless steel mesh between the two. The honeycomb strongback also formed the second stage of the collimator. A multigrid collimator was placed above the strongback to provide the first stage of collimation. These were a series of etched molybdenum sheets with spacer frames between them. A 2 μm Kimfol polycarbonate film with a second surface aluminum reflector was placed above the multigrid collimator to act as a heat shield (Wood et al. 1984). The physical properties of each module are summarized in Table 4.1.

Sensor Module	FOV (roll x pitch)	View Direction	Collecting Area (cm^2, m^2)	Comments
1	2 deg x 8 deg	-Y	1650 (0.165)	Failed 9/23/77
2	2 deg x 8 deg	-Y	1650 (0.165)	Failed 9/22/77
3	2 deg x 8 deg	-Y	1650 (0.165)	Single Detector Case
4	2 deg x 8 deg	-Y	1650 (0.165)	Failed 1/26/78
5	2 deg x 1 deg	-Y + 1/3 deg Z	1350 (0.135)	Dual Detector Case
6	2 deg x 1 deg	-Y - 1/3 deg Z	1350 (0.135)	
7	16 deg x 4 deg	+Y	1900 (0.135)	

Table 4.1: HEAO-A1 Module Properties

The transmission of the rectangular collimators of the HEAO-A1 modules can be modeled as the product of two two-dimensional collimators acting in orthogonal directions as described in Chapter 3. These are the in-scan (roll) direction and the spin axis (pitch) direction. This model was validated for the HEAO mission by a Monte Carlo simulation before launch and by scans through the Crab nebula once the satellite was on orbit and operational (Ibid). These scans were also used to calibrate the collimator

responses of the detectors for the purpose of generating the all-sky catalog. These calibrations were not used in the HEAO attitude determination studies described here.

All seven detectors were oriented nominally perpendicular to the spin axis of the satellite such that the spinning action caused them to sweep out great circles of the sky normal to the earth-sun line. Thus, every six months the entire celestial sphere would be scanned. The spin axis, called the 'Z-axis', was pointed at the sun and the nominal spin period was 0.00272 rad/sec. After some initial processing by the detector electronics, the photons from these scans were sent to the A-1 central electronics module where they were binned in either 0.320 sec (320 ms) or 0.005 sec (5 ms) time bins depending on the mode of operation. These data are stored along with energy information, housekeeping information and the orientation of the spacecraft on a tape recorder prior to downlink to a ground station (Ibid).

Of critical importance to the HEAO-1 mission and particularly to this research was the presence of a precision attitude determination system on board. This system consisted of two BBRC CT-401 fixed-head star trackers from Ball Research and four single degree of freedom gyroscopes. Course and fine sun sensors were also present on the spacecraft for initial acquisition and station keeping (Fallon, Wertz et al 1990). The CT-401 star tracker has an 8 deg x 8 deg field of view and has an accuracy of +/-3 arcminutes without calibration and +/-10 arcseconds when calibrated for such effects as temperature and star intensity variations. The calibration constants associated with these corrections are obtained from pre-flight testing (Ibid).

Information from these sensors was used to construct an aspect solution (as a function of time) for the spacecraft that was downlinked with the science data. This information was used in both the construction of the x-ray catalog and as a truth measurement in the attitude determination studies of this chapter.

4.3 HEAO-A1 Module 3 Attitude Determination Algorithm

The scanning data from Module 3 (Mod3) of the HEAO-A1 mission were used to demonstrate the concept of a single collimator x-ray star scanner. Furthermore, a sufficient number of trial scans existed to predict the performance of such an instrument. This analysis was done using the Interactive Data Language (IDL) on a UNIX workstation.

The steps taken to determine the attitude of the HEAO spacecraft from Mod3 scanned data are:

1. Select a single scan of the guide star. A sample of such a scan is shown later in Figure 4.2.
2. Fit an appropriate response function to the scan.
3. Determine the location of the guide star in detector coordinates from the fitted parameters.
4. Compare this to the known location of the guide star as given by the spacecraft aspect solution.
5. Generate an error signal in detector coordinates based on this difference.

The database from the HEAO-A1 mission is maintained by the Particle Astrophysics Group at SLAC by Professor Lynn Cominsky and graduate students Han Wen and Andrew Lee. This consists of scanning data from Modules 3 and 5 (some of which is binned at 0.320 sec and some of which is binned at 0.005 sec), pointed data from the high bit rate mode operations and programs necessary to process this information. The data from a series of scans by Module 3 over the Crab nebula were used in this study. Module 3 data were selected for two reasons: Module 3 was operational and stable for most of the mission and its large field-of-view in the pitch direction allowed it to see a given guide star for a number of scans. While the database consists of scans over hundreds of different sources, proving the star scanner concept only requires the analysis

of the performance of the instrument in scanning a single guide star. The Crab nebula was chosen as the guide star for several reasons:

1. Being the fourth brightest x-ray source in the sky (after the sun, Sco-X1 and GX4+1), it offers an excellent SNR at "large" instrument pitch angles.
2. The Crab is the "standard candle" of the x-ray sky. Problems due to the temporal variability of x-ray sources are minimized.
3. There are no bright sources in the vicinity of the Crab. Source confusion is eliminated.
4. The Crab Nebula has a pulsar at its center with a pulse period of 0.033 sec (33 ms). This offers a tie-in to x-ray timing studies discussed in Chapter 5.
5. The scanning data from the Crab have been used extensively by Han Wen in various other work. This made them readily available in a usable form.

The scans of Module 3 over the Crab were selected from the larger database by software written by Dr. Ken Fairfield. This data subset consists of the scanned data binned at 0.320 sec and the satellite aspect solutions at each time bin from the spacecraft attitude determination system. Each scan is constructed by concatenating three to five successive major frames. For the 320 msec data, a major frame is divided into 128 bins, each 0.320 sec long. The number of photons recorded by the detector are integrated over successive 320 msec segments and recorded in each bin. Each major frame is 40.96 sec long. Each scan is between 122 sec and 205 sec in length and contains a total of 384 to 640 bins.

When a subset of the Module 3 data is requested, that subset actually includes scans where the guide star was just out of the field of view of the instrument. This ensures that every usable scan is retrieved. Each of these must then be checked visually to eliminate those where the source does not appear or where there was an error in the detector. As an example, there were two scans where the data ended before the guide star

had passed through the collimator field of view completely. All sets where the data showed a complete scan over the guide star were kept in the subset. Some of the scans contained bins where the number of photons counted in that time step were in error. For example, the background rates (i.e. bins where the guide star was not in the field of view) were generally 20 to 50 counts per bin. In a few cases a bin that should have contained only background photons had a value of 2000 counts or more, while the bins preceding and following it had values corresponding to the expected background rate. The fitting algorithm employed to estimate the spacecraft orientation was specifically designed to be immune to such effects. This algorithm will be discussed in detail later.

The detectors used on HEAO-A1 had a deadtime associated with their processing electronics. Deadtime is the length of time it takes a detector to process a given photon hit during which the detector is insensitive to further x-rays. If a photon arrives at the detector before it has finished process the previous photon hit, the newly arriving photon will not be registered. The net effect of deadtime is to underestimate the number of photons arriving in a given bin. The data used here were corrected for the deadtime effect per the work of Han Wen in AstroGravity Note #14 (Han Wen, 1994) with an estimated detector deadtime of 1.4×10^{-5} sec (14 μsec). This correction is,

$$C_3 = \frac{C_{3d}}{1 - C_{3d}\frac{T_d}{T_b}} \tag{4.3.1}$$

where,
C_3 = Counts Corrected for Deadtime Effects
C_{3d} = Counts from Database
T_d = Detector Deadtime
T_b = Binning Time (320 msec)

A representative scan of the Crab, after it has been corrected for deadtime effects is shown in Figure 4.2. The bins were numbered according to the IDL standard for arrays from 0 to N-1 where N is the number of bins in a given scan.

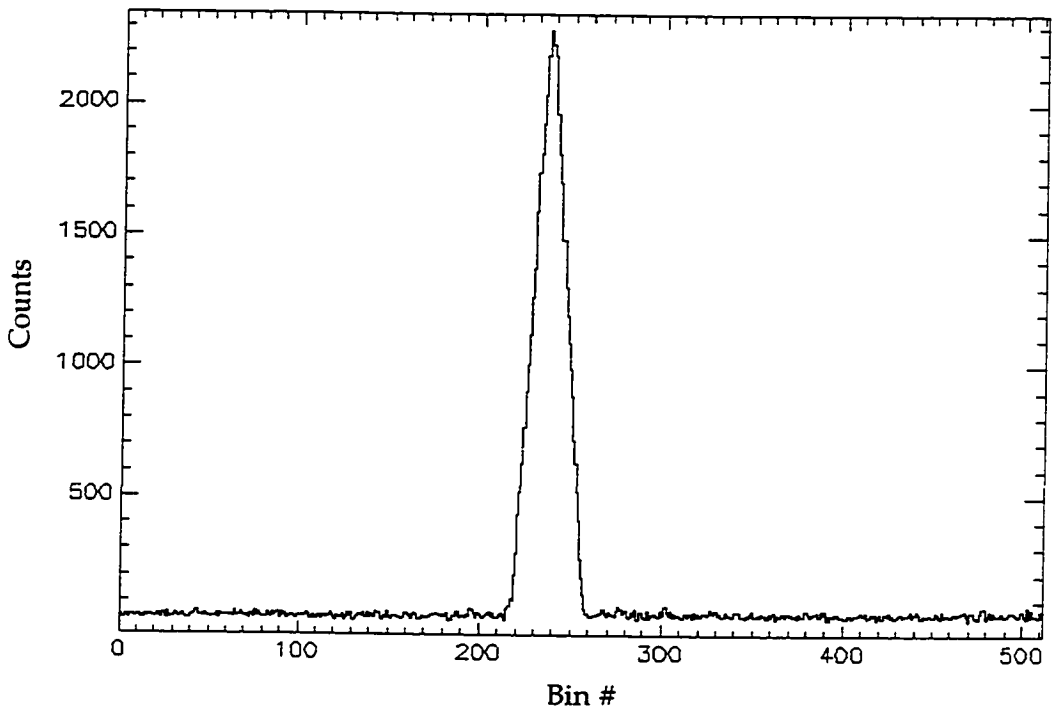

Figure 4.2: Sample HEAO-A1 Module 3 Data

The scan shown in Figure 4.2 is the sum of those photons collected by scanning over the guide star (the peak) and background photons (the constant offset), viz.:

$$Y_i = (B_i + RT_i)A \tag{4.3.2}$$

Y_i = Counts in Bin i

B_i = Background Rate in Bin i

where, R = Source Rate

T_i = Collimator Transmission at Bin i

A = Geometric Area of Detector

The background can be modeled by a simple function that is linear with time. The function has two parameters, B_0 and B_f, representing the number of background counts in the first and last bins of the scan respectively, viz.:

$$B_i = B_0 + \frac{i(B_f - B_0)}{N-1} \tag{4.3.3}$$

where, B_0 = Background Rate at Bin 0
B_f = Background Rate at Bin N - 1

The guide star intensity, R, must be given by a priori information. In this case, the intensity of the Crab Nebula is 4.121 counts/(sec*cm^2) (4.121(10^4) counts/(sec*m^2)) (Wood et al, 1984).

Recalling from Chapter 3 and Appendix D that the transmission of a rectangular collimator can be represented by the product of two independent, orthogonal one dimensional collimators, viz.:

$$T_i = T_{\alpha i} T_{\rho i} \quad \text{where,} \quad \begin{matrix} T_{\alpha} = \text{Transmission in Pitch at Bin i} \\ T_{\rho i} = \text{Transmission in Roll at Bin i} \end{matrix} \tag{4.3.4}$$

The individual transmission functions are,

$$T_{\alpha i} = \left(1 - \frac{\tan|\theta(0) + \delta_x|}{\tan(\alpha_o)}\right)\cos(\theta(0) + \delta_x), \quad |\theta(0) + \delta_x| \le \alpha_o \tag{4.3.5a}$$

$$T_{\alpha i} = 0, \quad |\theta(0) + \delta_x| \ge \alpha_o \tag{4.3.5b}$$

$$T_{\rho i} = \left(1 - \frac{\tan|\Omega t_i + \delta_z|}{\tan(\rho_o)}\right)\cos(\Omega t_i + \delta_z), \quad |\Omega t_i + \delta_z| \le \rho_o \tag{4.3.5c}$$

$$T_{\rho i} = 0, \quad |\Omega t_i + \delta_z| \ge \rho_o \tag{4.3.5d}$$

Recalling that t=0 is defined to be the time when the instrument roll angle, ρ, is zero, t_i can be written as follows:

$$t_i = t_b(i - i_p) \qquad \text{where,} \qquad \begin{array}{l} t_b = \text{Bin Size (sec)} \\ i_p = \text{Bin Number Where} \\ \quad\ \text{Roll Angle is Zero} \end{array} \qquad (4.3.6)$$

Combining equations 4.3.2 through 4.3.6, the signal from the x-ray star scanner, Y_{3i} can be written in terms of the fit parameters, viz.:

$$Y_i = \left(B_i(B_0, B_f) + RT_i(i_p, \theta(0), \Omega)\right)A \qquad (4.3.7)$$

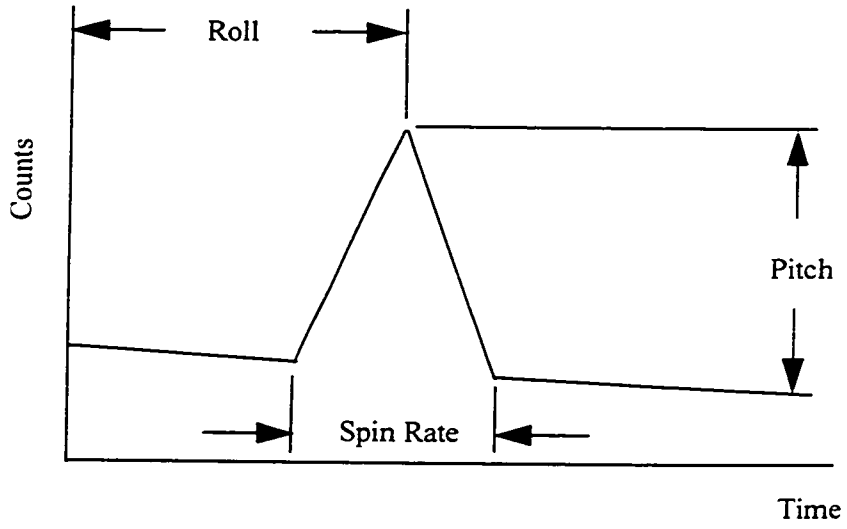

Figure 4.3: Single Detector Fit Parameters

Summarizing the five parameters in the model that we will fit (Figure 4.3):

1. The location of the peak transmission is a measure of the roll phase of the vehicle (i_p).
2. The height of the triangle is a measure of the pitch angle of the spin axis ($\theta(0)$).
3. The width of the triangle is a measure of the spin rate of the vehicle (Ω).

4 & 5. The background is modeled as a linear function of time (B_0,B_f).

The parameter vector is $P = [B_0, B_f, i_p, \Omega, \theta(0)]^T$

The number of counts actually measured by the HEAO-A1 Module 3 detector in bin i of a scan is C_{3i}. The problem is to find a set of parameters that makes Y_{3i} the most probable representation of the data, C_{3i}.

As described in Section 3.2.2, the number of photons arriving at the detector in a given time bin can be modeled by a Poisson distribution. That is, the probability of detecting n photons is governed by,

$$P(X = n) = e^{-\mu A t_b} \frac{(\mu A t_b)^n}{n!} \quad \text{where, } \mu = \text{ Total Intensity} \qquad (4.3.8)$$

As the mean value of the distribution, μAt_b, becomes large, the Poisson distribution approaches the Gaussian distribution, viz.:

$$\lim_{\mu A t_b \to \infty} P(x \le n) = \int_{-\infty}^{n} \frac{1}{\sqrt{2\pi\mu A t_b}} e^{-\frac{(z-\mu A t_b)^2}{\mu A t_b}} dz \qquad (4.3.9)$$

The number of counts in a given bin can be represented by a Gaussian distribution with mean, $\mu A t_b$ and standard deviation, $\sqrt{\mu A t_b}$.

The set of parameters, P, that provide the maximum likelihood solution to a data set with additive Gaussian noise is that set minimizing the Chi-squared error (Bevington, Robinson, 1992), viz.:

$$\min \chi^2 = \sum_{i=0}^{N-1} \frac{\left[Y_{3i}(P) - C_{3i}\right]^2}{\sqrt{C_{3i}}} \qquad (4.3.10)$$

This cost function was minimized by using a gradient search algorithm supplied by the IDL software called "CRVFIT". This method requires the user to supply the derivatives of the fitted curve, Y_{3i}, taken with respect to the fit parameters. The fitted curve used here is discontinuous at the edges of the field-of-view and at the peak of the transmission. Therefore, the derivatives of Y_{3i} were computed numerically.

To start the gradient search it is necessary to make an initial guess of the solution vector (the fitted parameters, P). It is not necessary to be extremely accurate in the initial guess. However, since the model of the data is nonlinear, the search can converge to different solutions given widely varying initial guesses. An easily computed starting point for the two background parameters (B_o, B_f) is a constant at the level of the average of the number of counts per bin over the whole scan, viz.:

$$B_0 = B_f = \frac{1}{N} \sum_{j=0}^{N-1} C_{3j} \qquad (4.3.11)$$

The nominal spin rate for the HEAO satellite is 0.00272 rad/sec. This is used as the initial guess for the spin rate parameter, Ω. Since no information about the pitch angle, $\theta(0)$, is available, $\theta(0)$ was initially set to zero. The zero roll bin, i_p, is the most critical initial guess in guaranteeing that the fitting process converges to the correct solution. This is due to the presence of random data upsets (discussed previously). For example, a simple criterion for selecting an initial value for i_p is to set it equal to the bin containing the most counts - expecting this bin to be near the middle of the peak in the scan. If there is an upset in the data that causes a background bin to have more counts than any bin in

the peak, the fit process will not converge properly. This can be avoided by using a slightly more complicated criterion: The number of counts in each bin are replaced by the average number of counts in that bin, the preceding bin and the following bin. The initial guess for the zero roll bin, i_p, is set to the bin with the most total counts, viz.:

$$f(i_p) = \max_i \left(\sum_{j=i-1}^{i+1} C_{3j} \right) \tag{4.3.12}$$

The result of this fitting process is a measure of the satellite orientation with the maximum likelihood of representing the true set of parameters that created the scan. This process was used to estimate the orientation of the satellite from 99 independent scans of the Crab Nebula.

Each estimate of the satellite orientation was then compared to the truth measure of the spacecraft orientation to determine the errors in the star scanner estimates. The truth measurements were provided by the on-board star trackers and were recorded four times per major frame. The actual spacecraft orientation at each time bin was determined by linearly interpolating between the two nearest truth measurements. These measurements provided the pointing directions of the spacecraft y and z axes in celestial coordinates.

Given the position of the guide star in celestial coordinates (from the HEAO Catalog) and the orientation of the spacecraft in celestial coordinates, the spacecraft orientation can be transformed into guide star coordinates per Appendix E. The location of the guide star can then be represented by the instrument pitch and roll angles, ρ_i and α_i as a function of the time bin, i. The x-ray star scanner estimate of the spacecraft orientation occurs at just one time bin, i_p. At this point the estimated instrument roll angle is 0, while the instrument pitch angle is $\theta(0)$. The true spacecraft roll rate can be determined from successive orientation solutions, viz.:

$$\Omega_t = \sin^{-1}\left(\frac{\hat{Y}(i_b) \bullet \hat{Y}(i_b + 1)}{t_b} \right) \tag{4.3.13}$$

The error in the star scanner orientation estimate can now be determined, viz.:

$$\alpha_e = |\alpha_t| - |\theta(0)| \tag{4.3.14a}$$

$$\rho_e = \rho_t - 0 \tag{4.3.14b}$$

$$\Omega_e = |\Omega_t| - |\Omega| \tag{4.3.14c}$$

Note that the pitch angle error and roll rate error involve the differences in the magnitudes of the truth measures and the star scanner estimates. This is due to the fact that the sign of the pitch angle and the sign of the roll rate are not observable by an x-ray star scanner. The results of this study are shown in Figure 4.4.

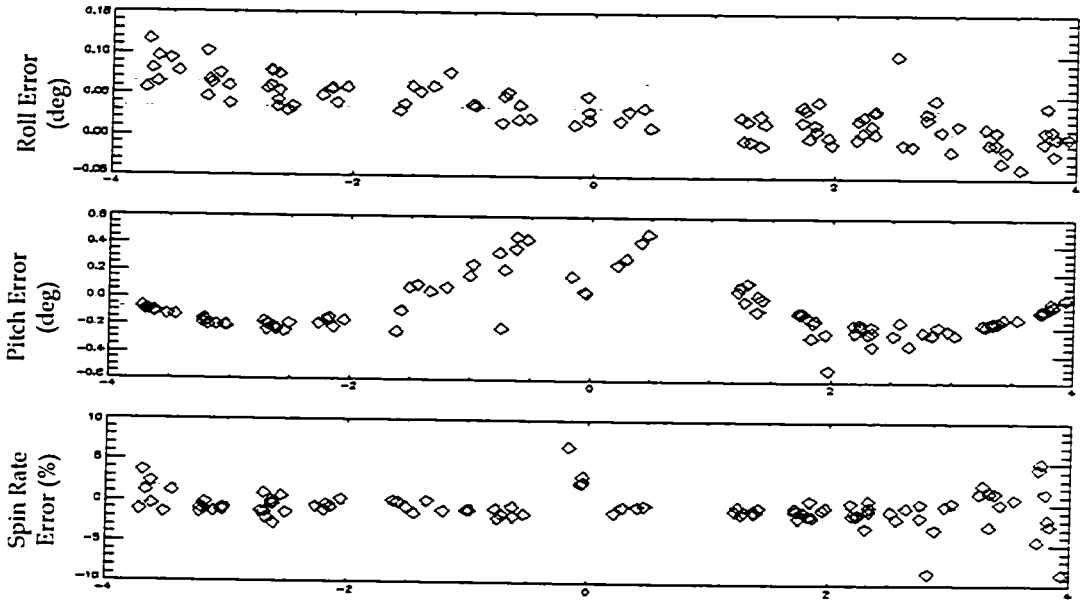

Figure 4.4: Single Detector Results

This study demonstrates the general concept of using an x-ray star scanner to determine the orientation of a spinning spacecraft. The error in the roll estimate over the 99 scans had a mean of 0.032 deg and a standard deviation of 0.030 deg. When plotted as a function of the true pitch angle, the roll error appears to be a linear function of the pitch

angle. This is consistent with a slight misalignment of the instrument axes relative to the spacecraft axes as discussed in Section 3.3.6.

The errors involved in measuring the pitch angle are much greater (-0.084 deg mean and 0.19 deg standard deviation). The large errors in the pitch angle estimate can be attributed to two factors. First and foremost, the pitch angle estimate a function of the a priori estimate of the guide star intensity. This estimate may be in error either due to the inherent temporal variability of the guide star or due to errors in the intensity measurements reported in the HEAO Catalog. An underestimation of the guide star intensity will lead to an over estimate in the pitch angle that is proportional to the magnitude of the true pitch angle. That is, when the guide star is near the limit in the instrument field of view, the total guide star signal will be small and the error in the pitch angle estimate will be small. When the guide star is close to the instrument line of sight, the total guide star signal will be large and the error the pitch angle will be at its greatest. Note that the overall structure of the pitch error shown in Figure 4.4 is consistent with an underestimate in the intensity of the Crab Nebula.

The simple model of the collimator transmission used here may also lead to errors in the pitch estimate. The collimator transmission, as manufactured, will be more complicated than the simple linear model described in Chapter 3. Calibration of the x-ray star scanner before launch would allow a more accurate model of the instrument to be used.

The measurement of the spin rate has a bias of -0.56% of the actual rate and a standard deviation of about 2%. The bias may be introduced by differences between the approximate geometry of the collimator and its actual geometry. That is, if the actual field of view of the collimator is 1% larger than the anticipated field of view (ρ_0), the spin rate estimate will be 1% slow. Note also that the spin rate estimates at the edges of the collimator field of view show decreasing accuracies. This is due to the fact that the smaller signal present at large pitch angles makes it more difficult to fit the collimator transmission to the data.

Three of the roll rate estimates made when the pitch angle was nearly zero have errors as large as 7%. This can be attributed to the error in the estimate of the guide star intensity. This intensity was probably underestimated as described above. At pitch angles near zero, the fitting process has a problem - it cannot make the fitted peak high enough to match the data. The closest fit to the data has zero pitch angle (to get as close as possible to the peak) and a wider base than the data. This wider base results in a spin rate estimate that is slower than the true spin rate.

4.4 HEAO-A1 Module 3/5 Attitude Determination Algorithm

There are two major drawbacks to using a single detector as an x-ray star scanner:

1. The sign of the pitch angle cannot be determined.
2. The magnitude of the pitch angle estimate is dependent on an a priori estimate of the intensity of the guide star. Any error in the estimate of the intensity leads to an error in the estimate of the pitch angle. The previous study with a single collimator instrument demonstrates this.

A differential x-ray star scanner can be constructed by using two single collimator x-ray star scanners in conjunction as described in Chapter 3. If each scanner is oriented such that during a scan the guide star is at different pitch angles in each instrument fame. then the relative strengths of the two signals is a measure of the pitch angle of the spacecraft and is independent of the guide star intensity. In fact. one of the parameters in the model will be the instantaneous guide star intensity.

By using data from the Module 5 (Mod5) detector in conjunction with that from the Module 3 detector. the operation of a differential detector as an x-ray star scanner can be demonstrated. The Mod5 detector was offset by 1/3 deg in pitch relative to the Mod3 detector which was aligned with the spacecraft axes. It also had a much smaller field-of-view in the pitch direction (0.5 deg vs. 8 deg for Mod3). Unfortunately, this difference in collimator geometry means that a double solution exists for the pitch angle measurement

- one on either side of the Mod5 pointing direction. This ambiguity is shown in Figure 4.5. The section of the Module 5 pitch axis transmission curve that is non-zero falls completely within that portion of the Module 3 pitch axis transmission that is non-zero. Thus, there are two possible spacecraft pitch angles that could generate any single scan. Each solution will have a different measure of the instantaneous guide star intensity. Since we no longer use a priori information about this parameter, there is no way to determine which solution is correct. This was resolved by generating both solutions and selecting the solution with the proper pitch angle sign based on the sign of the truth measurement. Note that a dual collimator instrument specifically designed as a star scanner would not have this ambiguity problem.

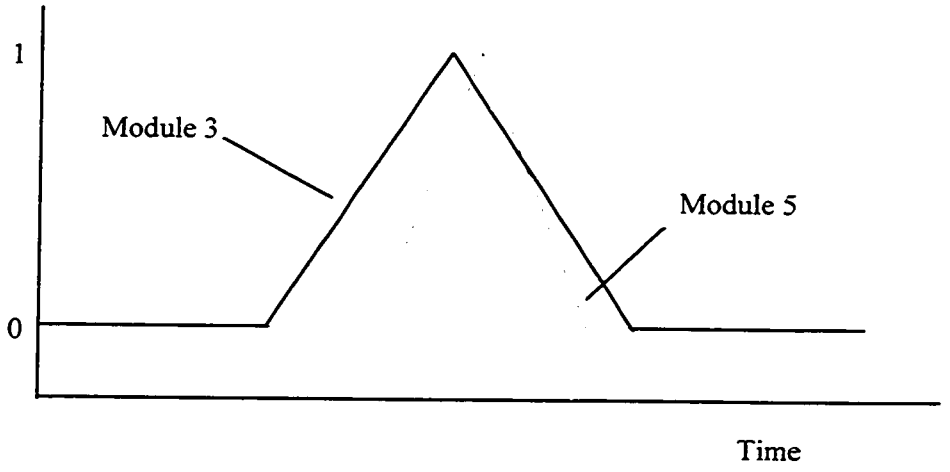

Figure 4.4: HEAO-A1 Differential Detector Ambiguity

The same basic algorithm was followed for the differential star scanner analysis as was followed for the single collimator star scanner analysis:

1. Select a single scan where the target source appears in both Module 3 and Module 5.
2. Fit an appropriate response function to the scans.
3. Determine the location of the source in instrument coordinates from the fitted parameters.
4. Compare this to the known location of the source as given by the spacecraft aspect solution.
5. Generate an error signal based on this difference.

In order to allow direct comparison to the results for the single detector, the Crab was chosen as the guide star for the dual detector analysis. Because the FOV of Module 5 is considerably smaller than that of Module 3, only a small subset of the scans available to Module 3 are also available to Module 5. This subset was further reduced by the fact that Module 5 was not operational at all times. The count rates for the data from both Module 3 and Module 5 were corrected for deadtime effects as described previously. The deadtime for Module 5 was assumed to be 14 μsec since the detectors had identical electronics suites. An example of the data from the two modules corresponding to one scan is shown in Figure 4.6.

In addition to differences in the signals caused by the geometry of the two collimators, Module 3 and Module 5 have different collecting areas. These differences in geometry were accounted for in the modeling process. Thie modeling process for the differential star scanner case is similar to that for the single collimator star scanner case with three exceptions. The backgrounds for each detector were modeled as linear functions in time with independent parameters for each. The intensity of the guide star was added to the model. The roll phase, pitch angle and guide star intensity parameters make it necessary to perform the fit on the two scans simultaneously.

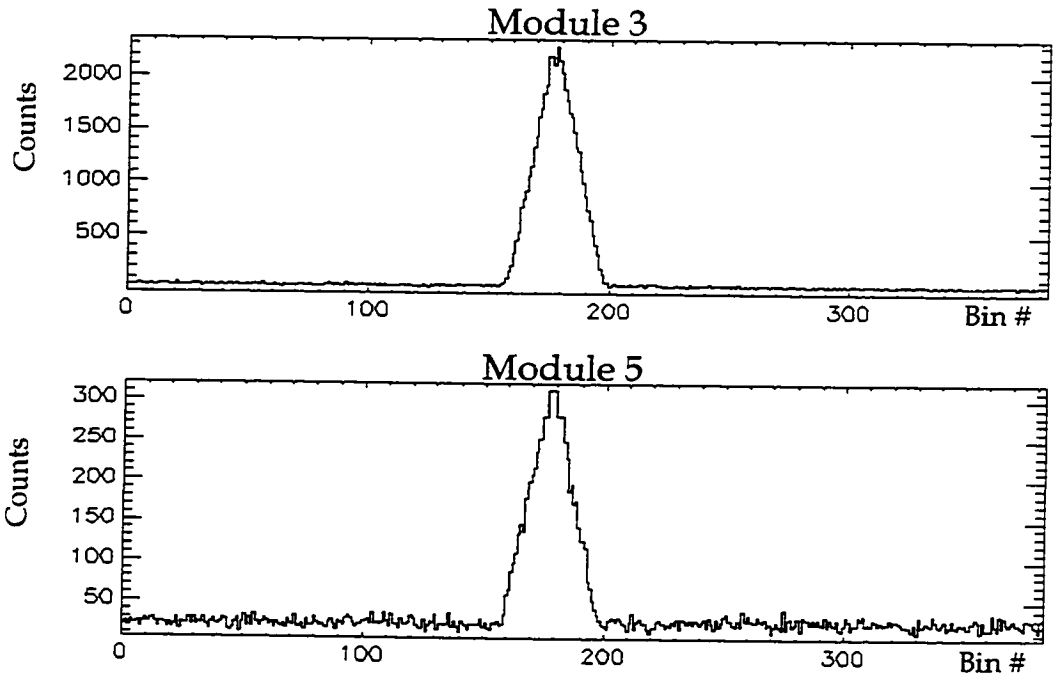

Figure 4.6: Dual Detector Sample Data

Reviewing Section 4.3, the number of counts in any bin of a scan by Module 3 or 5 can be written as,

$$Y_{3i} = (B_{3i} + RT_{3i})A_3 \qquad (4.4.1a)$$

$$Y_{5i} = (B_{5i} + RT_{5i})A_5 \qquad (4.4.1b)$$

where, Y_{ji} = Counts in Bin i of Module j

B_{ji} = Background Rate in Bin i of Module j

R = Source Rate

T_{ji} = Module j Collimator Transmission at Bin i

A_j = Geometric Area of Module j Detector

The background seen by each detector is modeled as a linear function in time, viz.:

$$B_{3i} = B_{30} + \frac{i(B_{3f} - B_{30})}{N-1} \quad \text{where,} \quad \begin{matrix} B_{30} = \text{Background Rate at} \\ \text{Bin 0 of Module 3} \\ B_{3f} = \text{Background Rate at} \\ \text{Bin N - 1 of Module 3} \end{matrix} \tag{4.4.2a}$$

$$B_{5i} = B_{50} + \frac{i(B_{5f} - B_{50})}{N-1} \quad \text{where,} \quad \begin{matrix} B_{50} = \text{Background Rate at} \\ \text{Bin 0 of Module 5} \\ B_{5f} = \text{Background Rate at} \\ \text{Bin N - 1 of Module 5} \end{matrix} \tag{4.4.2b}$$

The transmission of Module 3 is modeled as in Section 4.2. The Module 5 transmission is modeled similarly. The axes of the Module 5 collimator are not aligned with the spacecraft axes. This is modeled by the δ_{5x} term that is now non-zero.

$$\begin{aligned} T_{5\alpha i} &= \left(1 - \frac{\tan|\theta(0) + \delta_{5x}|}{\tan(\alpha_{5o})}\right)\cos(\theta(0) + \delta_{5x}), && |\theta(0) + \delta_{5x}| \le \alpha_{5o} \\ T_{5\alpha i} &= 0, && |\theta(0) + \delta_{5x}| \ge \alpha_{5o} \\ T_{5\rho i} &= \left(1 - \frac{\tan|\Omega t_i + \delta_{5z}|}{\tan(\rho_{5o})}\right)\cos(\Omega t_i + \delta_{5z}), && |\Omega t_i + \delta_{5z}| \le \rho_{5o} \\ T_{5\rho i} &= 0, && |\Omega t_i + \delta_{5z}| \ge \rho_{5o} \end{aligned} \tag{4.4.3a-d}$$

Following the notation of Section 4.2, the signals from the differential star scanner can be modeled, viz.:

$$Y_{3i} = \left(B_i(B_{30}, B_{3f}) + RT_{3i}(i_p, \theta(0), \Omega)\right)A_3 \tag{4.4.4a}$$

$$Y_{5i} = \left(B_i(B_{50}, B_{5f}) + RT_{5i}(i_p, \theta(0), \Omega)\right)A_5 \tag{4.4.4b}$$

Summarizing the eight parameters in the model that will be fitted to the data (Figure 4.7):

1. The location of the peak transmission is a measure of the roll phase of the vehicle (i_p).
2. The difference in the heights of the triangles is a measure of the pitch angle of the spin axis ($\theta(0)$).
3. The absolute heights of the triangles is a measure of the intensity of the guide star (R).
4. The width of the triangles is a measure of the spin rate of the vehicle (ω_s).

5-8. the background is modeled as a linear function of time. The background seen by each module is modeled independently (B_{30},B_{3f}, B_{50},B_{5f}).

The parameter vector is $P = [B_{30},B_{3f}, B_{50},B_{5f}, i_p, \Omega, \theta(0),R]^T$

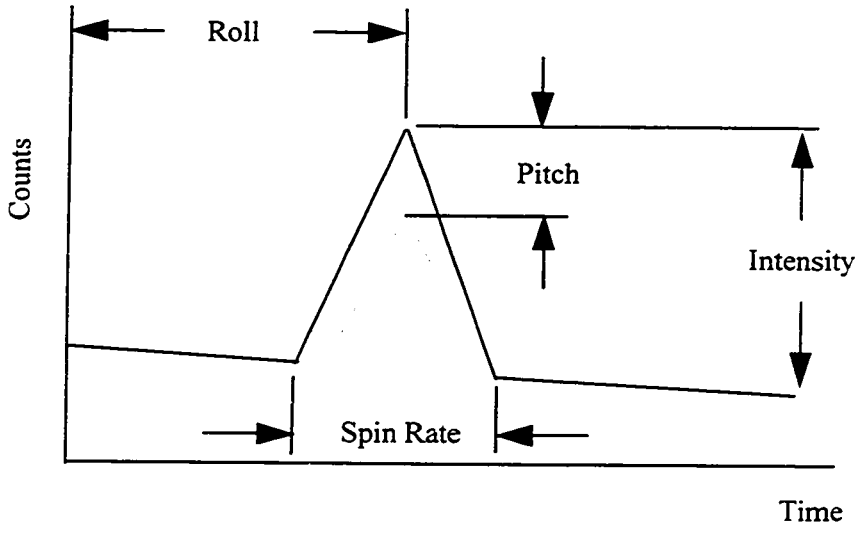

Figure 4.7: Dual Detector Fit Parameters

The two curves (one for each Module) were fitted to the data simultaneously by minimizing the Chi-Squared error. That is,

$$\min \chi^2 = \sum_{i=0}^{N-1} \left\{ \frac{[Y_{3i}(P) - C_{3i}]^2}{\sqrt{C_{3i}}} + \frac{[Y_{5i}(P) - C_{5i}]^2}{\sqrt{C_{5i}}} \right\} \qquad (4.4.5)$$

Again, this was minimized using the IDL routine "CRVFIT" and the derivatives were computed numerically. The initial guess was generated as in Section 4.3 with three exceptions. The roll phase was initialized by using the Mod3 data alone as discussed previously. The initial intensity of the guide star was taken from the HEAO catalog. The background rates were initialized by computing the mean count rates from the two scans separately.

After solving for the set of parameters that minimize this cost function, the attitude solution was compared to the truth measurement of the spacecraft attitude. Seven scans were available where the Crab nebula passed through both the Mod3 and Mod5 collimator fields of view. The resulting improvements in the roll angle estimate, pitch angle estimate and roll rate estimate are shown in Figure 4.8.

The additional information available from Module 5 leads to a three fold improvement in the roll estimate. In particular, the standard deviation in the roll error was reduced to 0.0075 deg while the bias dropped to 0.012 deg. This improvement is due in part to the subset of the data used for the differential x-ray star scanner studies. The small field of view on the Mod5 collimator limited the data set to scans where the guide star was at small pitch angles. This means that the linear structure that appears in the single collimator roll error data is suppressed.

The estimate of the pitch angle improved dramatically. The magnitude of the bias was reduced by a factor of four to 0.018 deg and the standard deviation improved by an order of magnitude to 0.021 deg. This is due to the fact that the intensity of the source did not need to be known a priori. Thus, any ambiguity in the knowledge of this term did not introduce error into the pitch estimate. Note that if we examine the performance of the single collimator x-ray star scanner in measuring the pitch angle over the small subset

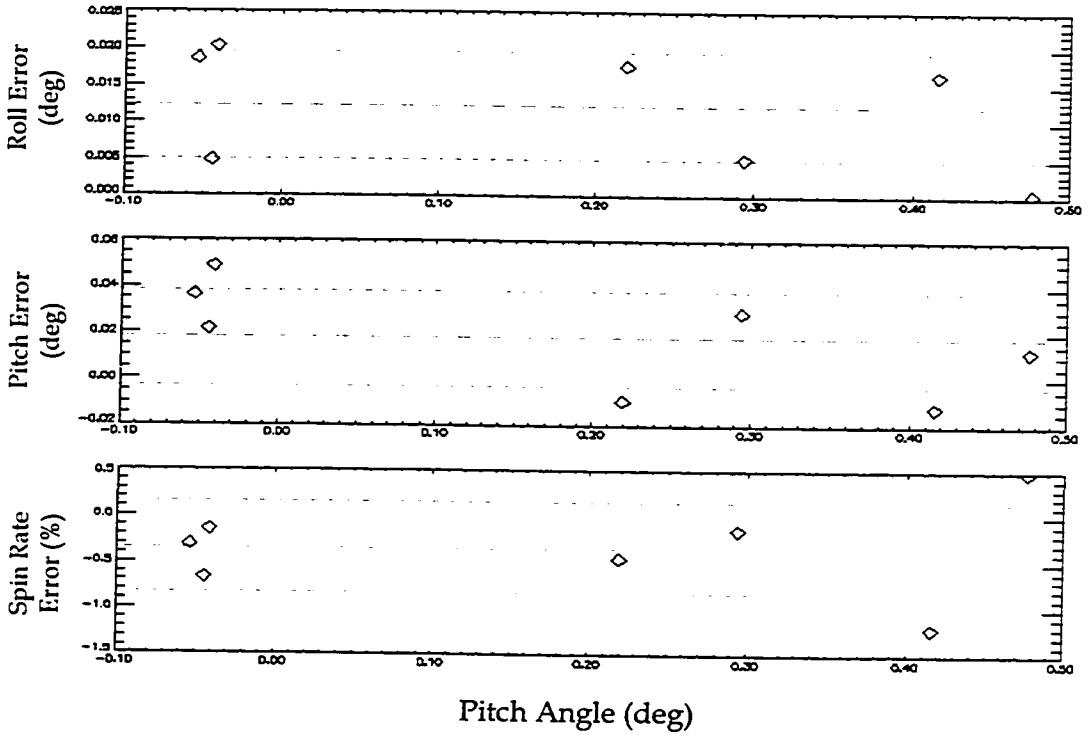

Figure 4.8: Dual Detector Performance

of scans available to the differential x-ray star scanner. the improvement in the differential collimator approach in seen to be even more dramatic.

The roll rate error showed a slight improvement in bias (-0.35%) and a four-fold improvement in the standard deviation of the error (0.48%). The addition of the guide star intensity to the model has led to an improvement in the estimate of the spin rate when the guide star is at small pitch angles. The 2% to 7% error seen in this parameter as described in Section 4.2 has been eliminated. The model can now match the large count rates consistent with small pitch angles that could not be effectively modeled before. Note also that scans with large pitch angles were not part of the subset used in this analysis.

While only seven scans were available to demonstrate the performance of differential x-ray star scanners, this instrument is shown to be capable of using x-ray

guide stars to measure the orientation of the spacecraft with accuracies on the order of 0.01 deg.

4.5 Dual Detector with Second Order Model

While the performance of an x-ray star tracker using a first order model in the attitude fitting process demonstrates promising performance, there appear to be residual errors in the data that may be modelable. In particular, the roll error data from the single detector case shows a correlation between the roll error and the true pitch angle wherein the roll error appears to be linear with the pitch angle. As described in Chapter 3, the second order star scanner model predicts just such an effect. If the collimator is not properly aligned with the vehicle axes, a roll error that is proportional to the pitch angle will be introduced, viz.:

$$T(\rho,\alpha) = T_\rho(\rho)T_\alpha(\alpha) = \left(1 - \frac{\left|\Omega t + \delta_z + (\theta(0) + \delta_x)(\delta_y + \varepsilon_y)\right|}{\rho_o}\right) * \left(1 - \frac{\left|\theta(0) + \delta_x - \dot{\theta}(0)t + (\varepsilon_y + \delta_y)(\Omega t + \delta_z)\right|}{\alpha_o}\right) \quad (4.5.1)$$

Note that this model predicts that the peak transmission is moved in roll linearly with the pitch angle due to the misalignment term, ε_y. The roll error shown in Figure 4.4 corresponds to a misalignment of about 1.5 deg. This happens to be approximately the size of the deadband of the attitude control system. There is also a term due to the polhode motion of the vehicle, $\dot{\theta}(0)$ (described in Chapter 3).

The second order model was implemented in the fit process of the single detector star scanner by adding a term for the collimator misalignment and a term for the polhode motion to the parameter vector. Unfortunately, the results were not encouraging. More than half of the 99 scans available failed to converge to a solution and those that did showed a markedly worse estimate of roll and pitch than the estimates made without the

spin axis misalignment. This is due to the following. When only one scan is available, the spin axis misalignment term, ε_y, is determined by fitting the skewness of the scan. The pitch angle is estimated from the height of the transmission peak. The roll angle estimate is then modified by the product of ε_y and α. Fitting the skewness of the scan is susceptible to noise and the pitch angle estimate is a function of the predicted intensity of the source. Any error in the estimate of these two parameters leads to a direct error in the estimate of the roll angle. With the pitch angle in error by as much as 0.8°, the roll angle estimate becomes corrupted.

By using two detectors, the estimate of the spin angle can be determined from the differential location of the peak in the scans (Figure 4.9). Since the two detectors have different pitch alignments, a misalignment of the spin axis about the nominal collimator normal will cause the peaks of the transmission curves in the two modules to shift by differing amounts. If there is no spin misalignment, the peak transmission of the two modules will occur at the same time.

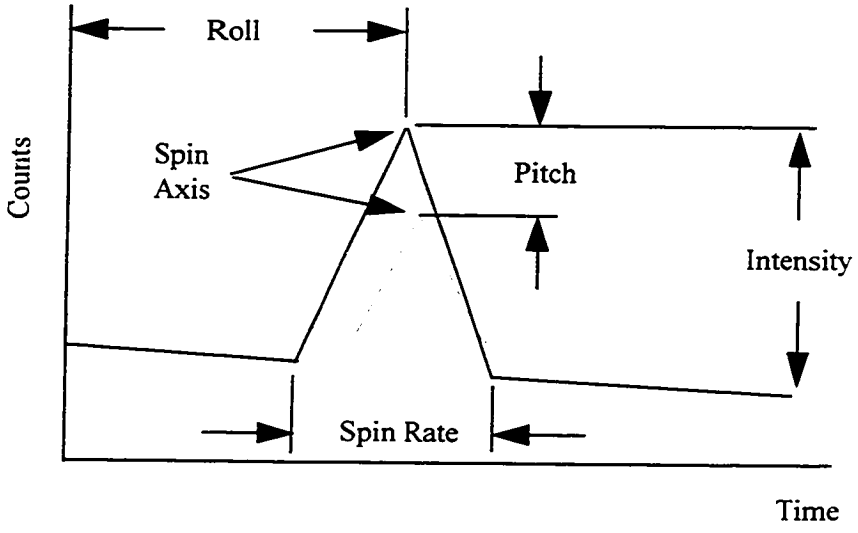

Figure 4.9: Dual Detector/Second Order Model Fit Parameters

The dual detector analysis of Section 4.4 was modified to use the second order star scanner model in the fitting process. The resulting transmission functions are.

$$T_{5\alpha i} = \left(1 - \frac{\tan\left|\theta(0) + \delta_x - \dot{\theta}(0)t + \varepsilon_y \Omega t\right|}{\tan(\alpha_{5o})}\right) \cos(\theta(0) + \delta_x - \dot{\theta}(0)t + \varepsilon_y \Omega t),$$

$$\text{when} \quad \left|\theta(0) + \delta_x - \dot{\theta}(0)t + \varepsilon_y \Omega t\right| \le \alpha_{5o}$$

$$T_{5\alpha i} = 0, \qquad \text{when} \quad \left|\theta(0) + \delta_x - \dot{\theta}(0)t + \varepsilon_y \Omega t\right| \ge \alpha_{5o}$$

(4.5.2a-b)

$$T_{5\rho i} = \left(1 - \frac{\tan\left|\Omega t + \theta(0)(\delta_y + \varepsilon_y)\right|}{\tan(\rho_{5o})}\right) \cos(\Omega t + (\theta(0) + \delta_x)\varepsilon_y),$$

$$\text{when} \quad \left|\Omega t + \theta(0)(\delta_y + \varepsilon_y)\right| \le \rho_{5o}$$

$$T_{5\rho i} = 0, \qquad \text{when} \quad \left|\Omega t + \theta(0)(\delta_y + \varepsilon_y)\right| \ge \rho_{5o}$$

(4.5.2c-d)

Summarizing the ten fit parameters:

1. The location of the peak transmissions is a measure of the roll phase of the vehicle (i_p).
2. The difference in the heights of the triangles is a measure of the pitch angle of the spin axis ($\theta(0)$).
3. The absolute heights of the triangles is a measure of the intensity of the guide star (R).
4. The width of the triangles is a measure of the spin rate of the vehicle (ω_s).

5. The difference in the location of the two peaks in a measure of the spin axis misalignment (ε_y).

6. The skewness of the scan is a measure of the polhode motion, $\dot{\theta}(0)$

7-10. A sloped background was fit to the data from each Module (B_{30},B_{3f}, B_{50},B_{5f}).

The parameter vector is $P = [B_{30},B_{3f}, B_{50},B_{5f}, i_p, \omega_s, \alpha,R, \varepsilon_y, \dot{\theta}(0)]^T$

The two curves (one for each Module) were again fit to the data simultaneously by minimizing the Chi-Squared error and the attitude solution was compared to the true aspect solution as previously discussed. Figure 4.10 shows that the increased complexity of the second order star model does not improve the performance of the instrument. This is probably due to the reduced set of scans available to the study. The small FOV of Module 5 limited the data set to scans with a small pitch angle - the same scans that should have the smallest error in roll angle due to spin axis misalignment. The spin misalignment estimate term was generally in the one degree range while the nutation rate was a few millidegrees per second.

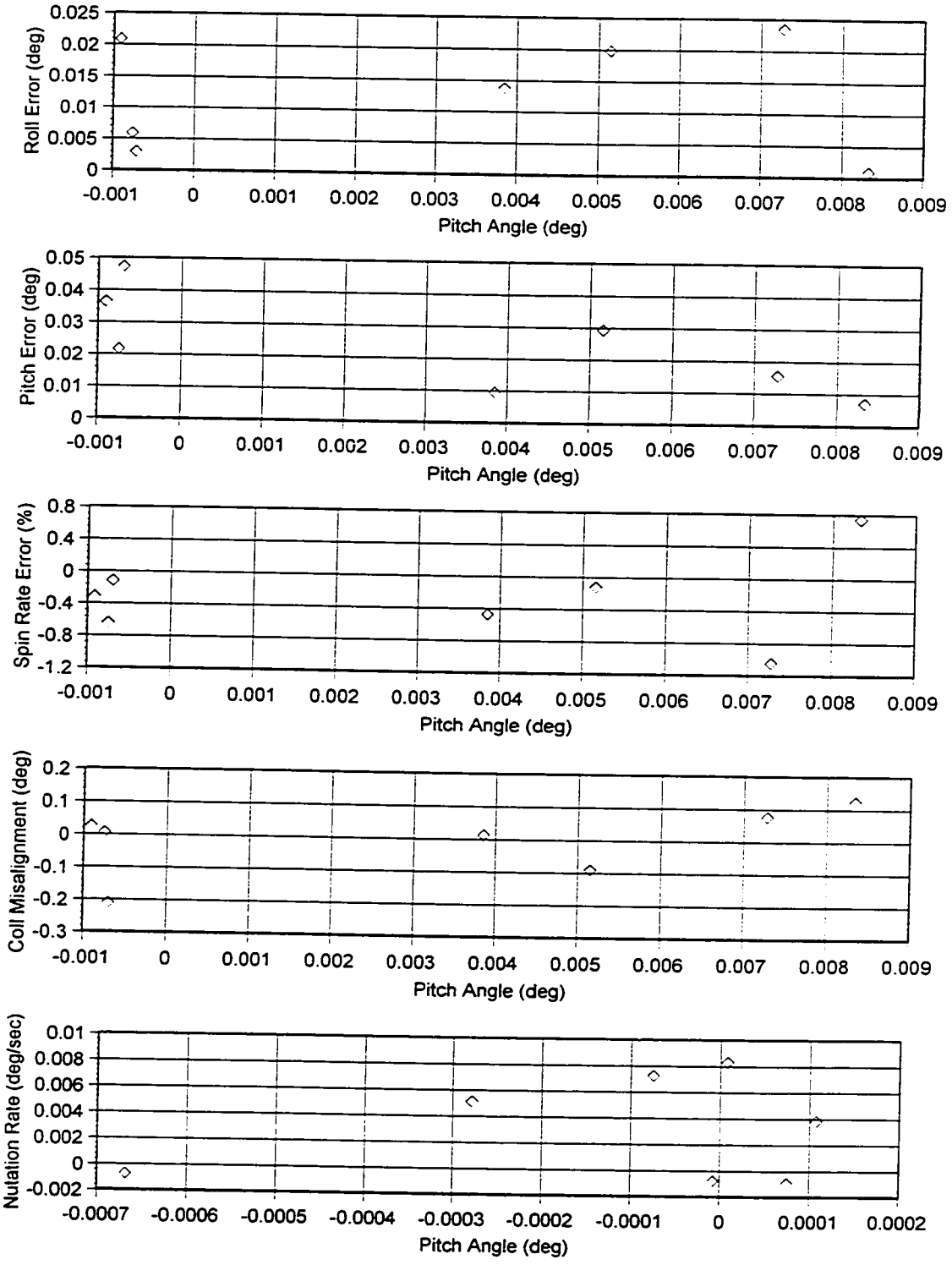

Figure 4.10: Differential Detector / Second Order Model Results

4.6 HEAO-A1 Attitude Determination Summary

Measured Parameter	Single Detector		Dual Detector (1st Order)		Dual Detector (2nd Order)	
	μ	σ	μ	σ	μ	σ
Roll Error (deg)	0.032	0.030	0.012	0.0075	0.013	0.0093
Pitch Error (deg)	-0.084	0.19	0.018	0.021	0.024	0.015
Roll Rate Error (%)	-0.56%	2.0%	-0.35%	0.48%	-0.28%	0.56%

Chapter 5: Autonomous X-ray Time Keeping

5.1 Introduction

One of the most exciting aspects of x-ray navigation is the prospect of using x-ray pulsars as frequency references. A single x-ray pulsar can provide a stable reference for keeping local time. Since the periods of known x-ray pulsars vary from milliseconds to months, by observing several pulsars simultaneously an unambiguous measurement of local time can be made. That is, each pulsar will give a measure of time on a different timescale - one for seconds, one for hours, one for days and so on (Wood, 93). Unlike current methods of keeping time, this method can be used to measure local time on satellites anywhere, so long as their position is known. Furthermore, this process requires no intervention from ground support or other systems (e.g. Global Positioning System).

In this chapter, we will consider the use of a single x-ray pulsar (Crab Nebula pulsar) to provide a frequency reference at short timescales ($\sim 10^{-2}$ sec).

5.2 Phase Locked Loops

The signal from an x-ray pulsar cannot be used directly as a clock signal by a satellite. The pulsations have a complex shape and are imbedded in an overall signal that has a very poor signal-to-noise ratio (SNR). To be useful, the satellite clock must have a signal with a specific pulse shape (e.g. sawtooth, square, sinusoid) and phase noise low enough to meet the mission timing requirements. This local clock is typically provided by an oscillator. The frequency of the local oscillator will drift with time due to environmental effects such as changing ambient temperature, vibration and even fluctuations in the local gravitational field (Gardner, 1979). To provide accurate time information over long timescales, it is necessary to slave the oscillator to a stable reference frequency - in this case an x-ray pulsar. In this way the long period fluctuations of the local oscillator can be removed.

While many different designs have been suggested to accomplish this, one of the most popular is to use a mechanism called the phase locked loop (PLL). A PLL is an estimator that uses a feedback loop to drive the phase difference between the reference signal (in this case the signal from the pulsar) and the signal from a voltage controlled oscillator (VCO) to zero. The VCO is a local oscillator that produces a periodic signal (square, sinusoid, sawtooth, etc.) whose frequency can be varied by an external signal. Furthermore, the presence of the VCO introduces a nonlinear element into the PLL that causes frequency of the VCO to be matched to the average frequency of the input signal. This allows the PLL to combine a narrow bandwidth in tracking for good noise rejection with a wide bandwidth in acquisition for robust performance.

The PLL (Figure 5.1) consists of four components:

1. Prefilter
2. Phase Detector
3. Loop Filter
4. Voltage Controlled Oscillator

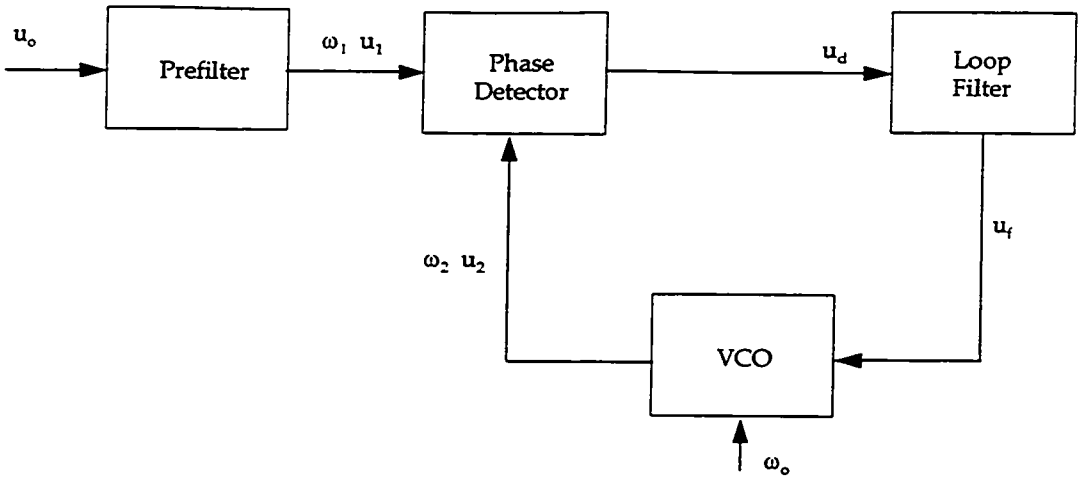

Figure 5.1: Phase Locked Loop Schematic

The reference signal (u_0) is first passed through a prefilter. This is typically a bandpass filter with a center frequency approximately equal to the reference frequency. The passband of the prefilter must be large enough to guarantee that any drift in the reference frequency or the prefilter parameters do not cause the reference signal to become attenuated, but small enough to remove as much noise as possible. Removing the noise with a prefilter helps the performance of the PLL in both acquisition and tracking.

The prefiltered signal, u_1, is then sent to the PLL. A complete description of the modeling of the phase locked loop is contained in Appendix H and a host of publications (Gardner, 1979; Best, 1993). This description is summarized here.

The phase detector takes the prefiltered reference signal, u_1, and the VCO signal, u_2, and computes the difference in phase between the two signals, viz.:

$$\theta_e = \theta_1 - \theta_2 \tag{5.2.1}$$

$$u_d = K_{pd}\theta_e \tag{5.2.2}$$

This phase error, u_d, is sent to its output. Ideally, the phase error would be computed directly. Unfortunately, u_1 and u_2 are typically sine waves - not direct phase measurements, so the phase error cannot be computed by simple subtraction. One way

to compute the phase difference between two signals is to multiply them together. Consider the simplest case where u_1 and u_2 are sine waves, but 90° out of phase:

$$u_1 = \sin(\theta_1) \tag{5.2.3}$$

$$u_2 = \cos(\theta_2) \tag{5.2.4}$$

$$u_d = K_{pd} u_1 u_2 \tag{5.2.5}$$

It can be shown (Appendix H) that for small phase errors the detector signal is,

$$u_d \cong K_{pd}\theta_e + \text{ terms at twice the reference frequency} \tag{5.2.6}$$

If this signal is passed through a loop filter that suppresses signals at twice the input frequency, the phase detector can be approximated as ideal. This implies that the loop is operating in a locked state. That is, the VCO frequency, ω_2, is the same as the reference frequency, ω_1.

One of the roles of the loop filter is to suppress the errors in the performance of the phase detector. Additionally, the loop filter is the primary factor in determining the performance of the PLL, in both tracking and acquisition modes. The literature is extensive on this point (Gardner, 1979). Many methods exist to design filters of varying complexity. Unfortunately, analytical description of the nonlinear acquisition of PLL operations exist only for PLL's with a few specific loop filters. In fact, it is difficult to guarantee the dynamic stability of loops with filters of higher than second order. Two loop filters whose performance have been described analytically are:

Active Lag-Lead: $$F_{lf}(s) = K_f \frac{1+\tau_2 s}{1+\tau_1 s} \tag{5.2.7a}$$

Proportional + Integral Control: $$F_{lf}(s) = \frac{1+\tau_2 s}{\tau_1 s} \tag{5.2.7b}$$

While the types of loop filters available are as varied as the applications of PLL's, these two filters provide an excellent set of design options while being simple enough to allow accurate prediction of their performance in acquiring and tracking a complex signal in the presence of noise (Gardner, 1979).

The voltage controlled oscillator is the local clock that will be used as the frequency reference by the satellite. The signal from the loop filter (u_f) is used to control the frequency of the VCO,

$$\omega_{vco}(t) = \omega_0 + K_{vco}u_f(t) \tag{5.2.8}$$

The phase of the VCO (θ_2), is just the integral of ω_{vco},

$$\theta_2(t) = \int_0^t \omega_{vco}(t)dt + \theta_2(0) \tag{5.2.9a}$$

$$\Theta_2(s) = \frac{K_{vco}}{s}U_f(s) \tag{5.2.9b}$$

$$u_2(t) = \cos(\theta_2(t)) \tag{5.2.10}$$

Note that when the VCO is tracking the reference signal (θ_e is small), the output of the VCO, u_2, is actually 90° out of phase with the reference.

The general nonlinear equations for a phase locked loop are,

$$U_1(s) = F_{pf}(s)U_0(s)$$
$$u_d(t) = K_{pd}u_1(t)u_2(t)$$
$$U_f(s) = F_{lf}(s)U_d(s)$$
$$\omega_{vco}(t) = \omega_0 + K_{vco}u_f(t)$$
$$\theta_2(t) = \int_0^t \omega_{vco}(t)dt + \theta_2(0)$$
$$u_2(t) = \cos(\theta_2(t))$$

where, $F_{pf}(s)$ = Prefilter Transfer Function
K_{pd} = Phase detector Gain
$F_{lf}(s)$ = Loop Filter Transfer Function
ω_0 = VCO Center Frequency
K_{vco} = VCO Gain

(5.2.11a-f)

If the loop is in the locked state, the equations for the phase-locked loop can be linearized in terms of the phase of reference signal and the VCO as (Best, 1993),

$$H(s) = \frac{\Theta_2(s)}{\Theta_1(s)} = \frac{K_{vco}K_{pd}F(s)}{s + K_{vco}K_{pd}F(s)} \tag{5.2.12a}$$

$$H_e(s) = \frac{\Theta_e(s)}{\Theta_1(s)} = \frac{s}{s + K_{vco}K_{pd}F(s)} \tag{5.2.12b}$$

Note that the performance of the loop, being generally defined by its closed loop poles, is a function of the detector gain K_{pd}. Since K_{pd} is a function of the amplitude of the input signal, variations in this amplitude or errors in predicting its size will affect the dynamics of the loop. This is demonstrated further in the PLL simulation discussed in Section 5.5.

Before the PLL can get into its locked state, it must undergo acquisition. In this process the nonlinear characteristics of the loop cause it to search for the frequency of the input signal. For example, if the VCO frequency is slower than the input signal frequency, over a cycle the input signal will lead the VCO signal causing a positive phase error. This is multiplied by the filter gain and ends up as a positive signal to the input of the VCO increasing the frequency of the VCO until it catches the input signal and locks.

There are several regimes of operation in which the nonlinear characteristics of the loop are important (Best, 1993). These ranges are generally described by a frequency offset about the nominal VCO frequency (Figure 5.2). The "Hold Range" is that frequency range where once the loop becomes locked, it will remain locked if no disturbances are present. This is the static stability limit of the loop. The "Pull-in Range" defines the dynamic stability limit of the loop. If the loop is unlocked, but the frequency offset is within the pull-in range, the loop will eventually lock-in. A subset of the pull-in range is the "Lock Range". The lock range defines a range of frequency offset inside which the loop will lock onto the reference signal within one beat note of the reference and VCO signals. That is, there will be no cycle slips before the PLL acquires the reference signal. Most loops are designed such that any conceivable initial frequency offset will be within the lock range. The acquisition performance of phase-locked loops with simple loop filters has been analyzed (Best, 1993). The performance of three simple loops are summarized in Table 5.1.

Loop Type	Active Lag-Lead	Proportional – Integral Control
Transfer Function	$F_{lf}(s) = K_f \frac{1+\tau_2 s}{1+\tau_1 s}$	$F_{lf}(s) = \frac{1+\tau_2 s}{\tau_1 s}$
Loop Natural Frequency	$\omega_n = \sqrt{\frac{K_{vco}K_{pd}K_f}{\tau_1}}$	$\omega_n = \sqrt{\frac{K_{vco}K_{pd}}{\tau_1}}$
Loop Damping	$\zeta = \frac{\omega_n}{2}(\tau_2 + \frac{1}{K_{vco}K_{pd}K_f})$	$\zeta = \frac{\omega_n \tau_2}{2}$
Hold Range	$\Delta\omega_H = K_{vco}K_{pd}K_f$	$\Delta\omega_H = \infty$
Pull-In Range	Complex	$\Delta\omega_P = \infty$
Lock Range	$\Delta\omega_L = K_f \frac{\tau_2}{\tau_1}$	$\Delta\omega_L = \frac{\tau_2}{\tau_1}$
Lock Time	$T_L = \frac{2\pi}{\omega_n}$	$T_L = \frac{2\pi}{\omega_n}$

Table 5.1: PLL Characteristics

5.3 Error Sources

Several factors can introduce errors into timing measurements that are made from X-ray pulsars.

Poisson Fluctuations

The dominant source of noise in an x-ray pulsar is the photon noise associated with the low count rates of these sources and appears to a PLL as a phase error. The purpose of the PLL is to reduce this error to an acceptable level.

Phase Detector Offset

The same non-linearities that give the phase-locked loop its adaptive characteristics also cause it to have a steady-state error in phase, even when the loop filter has an integral term that should drive such errors to zero. This is due to the multiplying effect of the phase detector and is a function of such measurable parameters as signal strength, detector and VCO gain and loop filter frequency response. It should be possible to describe this error analytically and remove it.

The complexity of the pulse shape will also introduce an offset in the time measurement as the loop will not lock onto the front of the pulse, but will lock in phase with the fundamental of the pulsation. This offset can be predicted analytically and removed as well.

Position-Timing Error

An error in the measurement of the position of a satellite will cause an error in the measurement of absolute time and, if fluctuations in position over short time scales are large enough, will cause errors in local time measurements by way of an apparent modulation of the reference frequency. Consider two detectors in two different positions measuring time from the same pulsar. If the distance traveled by the pulse wavefront from the star to each detector is different, the trailing detector will be measuring a time behind the leading detector, viz.:

$$\Delta t = \frac{\Delta x}{c} \qquad (5.3.1)$$

Thus, an error in the measured position of the satellite relative to some "inertial" point (i.e. the barycenter of the earth-sun system) of 300 m will cause an error in the inertial time measurement of 1 ms. Known satellite displacements (e.g. as the satellite orbits the earth and the earth orbits the sun) can be taken out of the measurements predictively to attain inertial measurements of time.

"Free-riding Zones"

At times a pulsar may not be available to a satellite (e.g. when the earth, sun or moon occludes the reference pulsar from the satellite). At these times the clock will be running at the last frequency update from a locked condition. This error cannot be removed from the measurements, but its magnitude can be bounded before the mission. Alternately, the clock can shift from one pulsar to the next as it orbits the earth.

Pulse Frequency Knowledge

The measurement of time is only as good as the reference. If there is error in the knowledge of the pulsar pulse period, this will be propagated into the absolute time measurement. Consider a detector that is locked onto a pulsar that has a pulse frequency of 10 Hz, but the knowledge of that pulse period is only good to a part in 10^9. If the actual pulse period of the frequency reference is $10 + 10^{-8}$, the local clock will run fast and the local time will diverge from absolute time. These errors cannot be removed, but they can be bounded.

Spin Down of X-ray Pulsars

The spin rates of pulsars are known to be increasing. These accelerations are very small and are systematic. They have been measured or bounded so that they can be removed from the measurements.

Local Oscillator Fluctuations

The local oscillator is not a perfect instrument, otherwise it would not need to be slaved to an x-ray source. Small variations in its frequency will increase the error in the local time. Additionally, if the local oscillator is used to time-tag the detector photons, this may cause an error in the measured signal.

Random Fluctuations of X-ray Pulsars

Some X-ray pulsars are known to have occasional random jumps in phase. If multiple sources are used for timing information, a fluctuation in one pulsar should be observable.

Doppler Shift of Pulsar Frequency

The motion of the detector along the line of sight to the reference object will cause the frequency of the pulsation to be Doppler shifted. This will cause a frequency error in the detector that is periodic with the orbit:

$$\Delta f = \frac{v_{los}}{c} f_{pulsar} \qquad (5.3.2)$$

where v_{los} is the velocity of the satellite along the line of sight to the pulsar.
This error will not grow with time and can be bounded and even removed to the level that the velocity of the satellite is known. Additionally, by observing multiple pulsars simultaneously, it should be possible to remove any long-term effects of the Doppler shift.

5.4 Simulation Description

To demonstrate the feasibility of using x-ray pulsars as inertial time references, the performance of a phase-locked loop was simulated. This simulation included the acquisition phase. Anticipating the USA mission, it was assumed that the HEAO catalog described the overall intensity of x-ray sources and that the response of the x-ray detector could be modeled as a HEAO detector (including the geometric area). This assumption also anticipates the availability of data from the pointed portions of the HEAO data. The results of this simulation should predict to some degree the performance of a PLL on HEAO pointed data as well as on a real-time USA mission.

Source	Alternate Name	Pulse Period (sec)	Type	Year of Discovery
	Crab Nebula	0.033		
X0535-668	A0538-66	0.069	Transient	1982
X0115-737	SMC X-1	0.71	Transient	1976
X1656+354	Her X-1	1.24	Variable	1972
X0115+634	V625 Cas	3.6	Transient	1978
X0332+530	BQ Cam	4.4	Transient	1985
X1119-603	Cen X-3	4.8		1971
X1048-594		6.4		1990
X2259+587		7.0		1980
X1627-673		7.7		1977
X1553-542		9.3		1983
X0834-430	GR0834-430	12.2	Transient	1991
X0532-664	LMC X-4	13.5	Variable	1983
X1417-624		17.6	Transient	1981
X1843+009		29.5		1990
X1657-415		38		1979
X2030+375		42		1989
X2138+568	Cep X-4	66		1991
X1836-045		81		1990
X1843-024		95		1990
X0535+262		104	Transient	1975
X1833-076	Sct X-1	111		1991
X1728-247	GX 1+4	114		1971
X0900-403	Vela X-1	283		1976
X1258-613	GX 304-1	272		1977
X1145-614		298		1978
X1145-619		292		1978
X1118-615	A1118-61	405	Transient	1975
X1722-363		413		1989
X1907+097		438		1984
X1538-522	QV Nor	529		1977
X1223-624	GX 301-2	696	Transient	1976
X0352-309	X Per	835		1990

Table 5.2: Pulsar Characteristics (White, 1995)

There are a number of pulsars that could be used as time references. Some of these are summarized in Table 5.2. The pulsar at the center of the Crab Nebula has one of the shortest periods yet discovered in an x-ray pulsar. It is one of the brightest sources in the x-ray sky in terms of total flux and has been studied extensively for a number of years. This source was also used as a guide star in the attitude determination portion of this thesis. For these reasons, the Crab Nebula was chosen as the pulsar reference for the inertial time reference simulation.

The Einstein mission was able to characterize the pulsar in the Crab Nebula quite extensively (Harnden, 1984). The pulse shape observed by Einstein in shown in Figure 5.2. Over a single period these pulsations account for about 4% of the total flux from the Crab. When pointed directly at the Crab, the rest of the signal comes from the steady flux from the nebula and from background (diffuse x-ray and trapped particles). The steady flux from the nebula is the primary contributor to the noise on the received signal. The signal from a pulsar at time step i can be written as,

$$C_i = B_i + S_i + P_i + N_i \tag{5.4.1}$$

where,

B_i = Counts from Background
S_i = Counts from Steady Part of Source
P_i = Counts from Pulsar
N_i = Counts from Noise

The pulsar was modeled by fitting a composite curve of four exponentials to the Einstein data. Each sub-pulse was modeled by a rising and a falling exponential and the resulting curves were added together. The location of the two peaks were fixed at bins 94 and 222. The two curves use to fit the two peaks are,

$$P_{1i} = a_1(e^{b_1 i} - 1) \qquad i < 94 \tag{5.4.2a}$$

$$P_{2i} = a_3(e^{b_3 i} - 1) \qquad i < 222 \tag{5.4.2b}$$

$$P_{1i} = a_2(e^{b_2(188-i)} - 1) \qquad i \geq 94 \tag{5.4.2c}$$

$$P_{1i} = a_4(e^{b_4(444-i)} - 1) \qquad i \geq 222 \tag{5.4.2d}$$

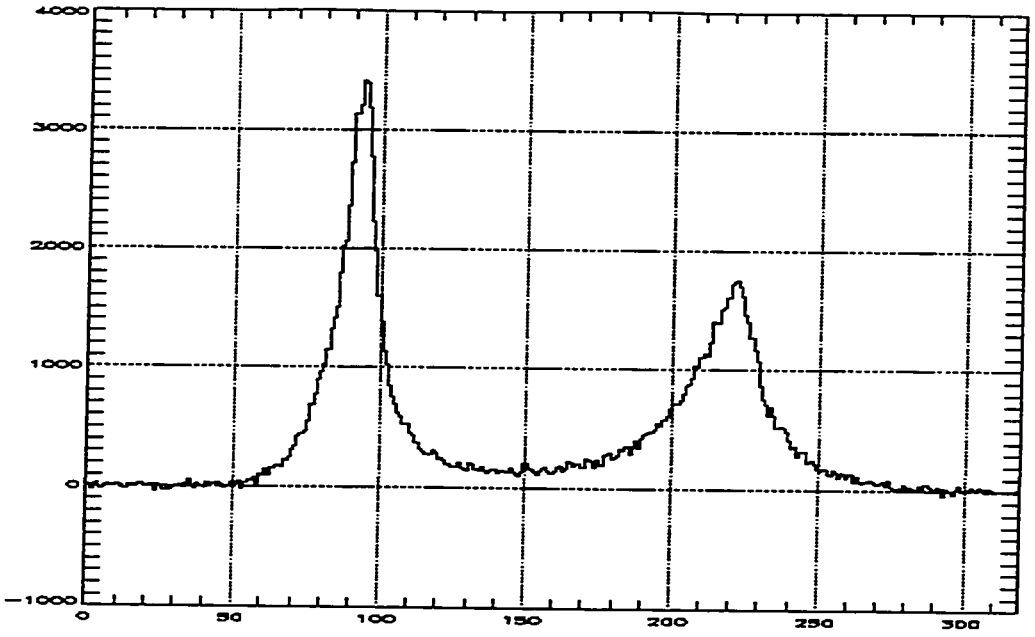

Figure 5.2: Observed Crab Pulse Shape

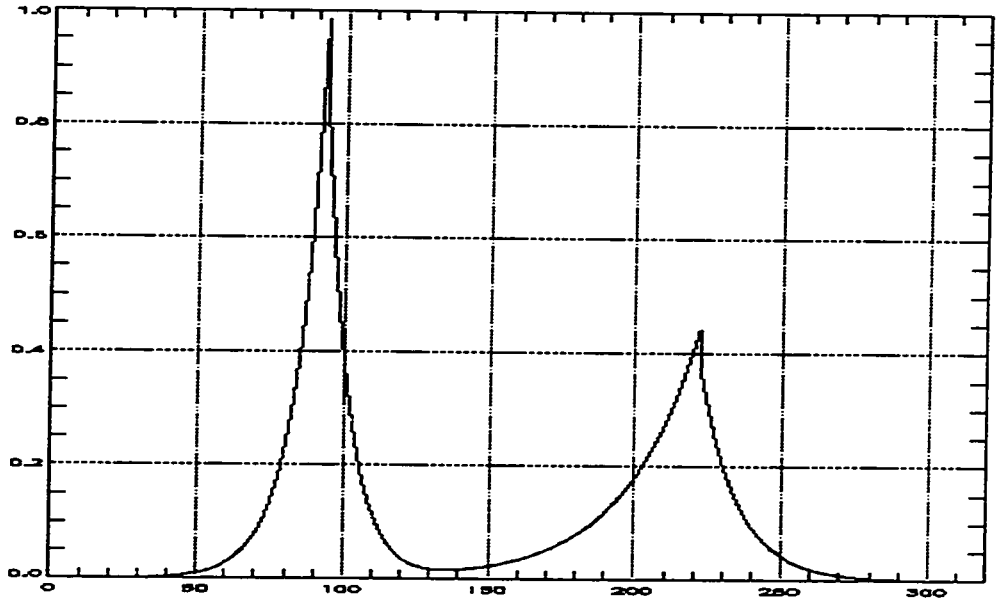

Figure 5.3: Crab Pulsar Fitted Shape

The parameters (a_1,b_1, a_2,b_2, a_3,b_3, a_4,b_4) were fit to the data by minimizing the Chi-squared error (Figure 5.3). The total number of pulsar counts at a particular bin is then (η_c is a normalizing parameter to get the proper ratio of pulsar counts to total counts),

$$P_i = (P_{1i} + P_{2i})\eta_c \tag{5.4.3}$$

When the size of the time bin is large compared to the features in the pulse shape, it is necessary to integrate the instantaneous count rate from the model over the total bin time. This has the effect of lowpass filtering the pulsar signal and was necessary in this simulation.

The noise present in the received signal is Poisson and can be added by using the POIDEV procedure in IDL. The mean of the signal is just the calculated signal level. For analysis purposes this noise can be approximated as Gaussian with zero mean and standard deviation,

$$\sigma_i = \sqrt{B_i + S_i + P_i} \tag{5.4.4}$$

The signal to noise ratio can then be approximated as,

$$SNR = \frac{P_i}{\sqrt{B_i + S_i + P_i}} \cong \frac{P_i}{\sqrt{B_i + S_i}} \tag{5.4.5}$$

5.5 Simulated PLL Design

While it is not the purpose of this simulation to optimize the performance of the phase locked loop in tracking the Crab pulsar, it is necessary to synthesize a design that will yield reasonable results. The first step in the design of the PLL is to determine the rate at which the reference pulsar will be sampled. This sets the bin size for the input signal, u_0. There are tradeoffs to be made in selecting a bin size. The smaller the bin size, the more points sampled per pulse and the better the representation of the pulse. But the noise in a given bin is inversely proportional to the square-root of the bin size. Thus, the smaller the bin size, the greater the noise on the signal. A large bin size was used to

reduce the level of noise on the signal, but at $5(10^{-3})$ sec (5 msec) sampling, several samples were taken per pulsation.

A series of simulated Crab data binned at 5 msec was generated based on the fitted pulsar curve. The mean rate from the steady portion of the Crab nebula was subtracted. A residual of the steady portion of the signal was left in the reference signal to simulate the uncertainties in the knowledge of this parameter. This was passed through a prefilter to eliminate any remaining bias in the signal and to reduced the level of noise in the signal to help the PLL gain and maintain lock. A second order Butterworth bandpass filter was designed in MATLAB using the "BUTTER" command (MATLAB, 1995). A Butterworth filter is an optimal filter that has the property that its passband is flat with zero gain. The size of the passband can be specified when constructing the filter. This must be large enough that any error in the expected input frequency will not place the fundamental of the pulsar signal outside the passband, resulting in a reduction of signal strength. The passband must be small enough, though, to reduce the noise on the signal as much as possible. It also suppresses the harmonics inherent in a pulse shape as complex as the Crab. The passband of the prefilter used here is +/-1% of the center frequency. The state space equations are contained in Appendix H.

The primary driver in determining the performance of the PLL is the design of the loop filter. An active lag loop filter was chosen since it has the most free parameters (3). There are two opposing goals in the performance of the PLL - good steady state noise rejection and fast acquisition time. It turns out that to get good noise rejection, a loop should have a low natural frequency, but to get fast acquisition it should have a high natural frequency. The maximum acquisition time is limited by the length of time that a pulsar can be tracked without interruption. For example, the USA Experiment can track a pulsar for no more than 1200 sec (20 min). On the other hand, the minimum acquisition time is limited by the desired accuracy of the local clock. These competing requirements were resolved by running the loop as slowly as possible while still acquiring the signal in a single USA pass - less than 1000 sec. The natural frequency (ω_n) of the loop was set at 0.01 Hz. The noise rejection is relatively insensitive to the closed loop damping (ξ)

in the neighborhood of its optimum - the critical damping ratio. Thus, the loop damping was set to 1.0.

Given the desired overall loop parameters (ω_n, ξ, K_{loop}), the loop filter can be designed in terms of the two crossover frequencies, τ_1 and τ_2 as follows,

$$\tau_1 = \frac{K_{loop}}{\omega_n^2} \tag{5.4.6a}$$

$$\tau_2 = \frac{2\xi}{\omega_n} \tag{5.4.6b}$$

The loop gain (K_{loop}) determines the VCO gain (K_{vco}) as follows,

$$K_{vco} = \frac{K_{loop}}{K_{pd} h_{inp}} \tag{5.4.7}$$

The phase detector gain (K_{pd}) is chosen such that the total gain through the phase detector ($K_{pd}h_{inp}$) is unity.

The loop performance parameters can then be calculated as indicated in Table 5.1.

5.6 Simulation Results

The performance of the phase locked loop was simulated with the following inputs:

VCO Frequency Offset:	0.01%
Mean Background Error:	1%
Initial Phase Error:	0 deg

The clock error is shown as a function of time in Figure 5.4 for a 2000 sec run. Note that the PLL initially runs ahead of the reference due to the initial frequency error. The loop begins to slow the VCO down at about 50 sec and is tracking the reference clock by 500 sec. The first 500 sec or so is the acquisition phase. For the remaining 1500 sec, the loop is tracking its reference. On average the VCO is 0.069 sec behind the reference and is generally within 0.0015 sec of this mean. This offset is not entirely a

error since the location of the zero phase point for the Crab pulse shape is arbitrary. The fundamental is not necessarily in phase with this selection. Since the PLL locks to the fundamental of the pulse shape, it will not necessarily lock to a zero phase offset.

Figure 5.5 shows a comparison of three signals within the loop: the raw input, the prefiltered signal and the VCO signal. Note that the raw signal cannot be used in any sense as a clock. The prefiltered signal at least appears sinusoidal, although there is a lot of amplitude and certainly some phase modulation of the signal. The tight bandwidth of the PLL yields the sinusoidal signal from the VCO shown in the bottom plot. The zero crossings can be used from this signal to determine time directly. Alternately, the phase measure from the simulation can be used as a time reference for higher update rates.

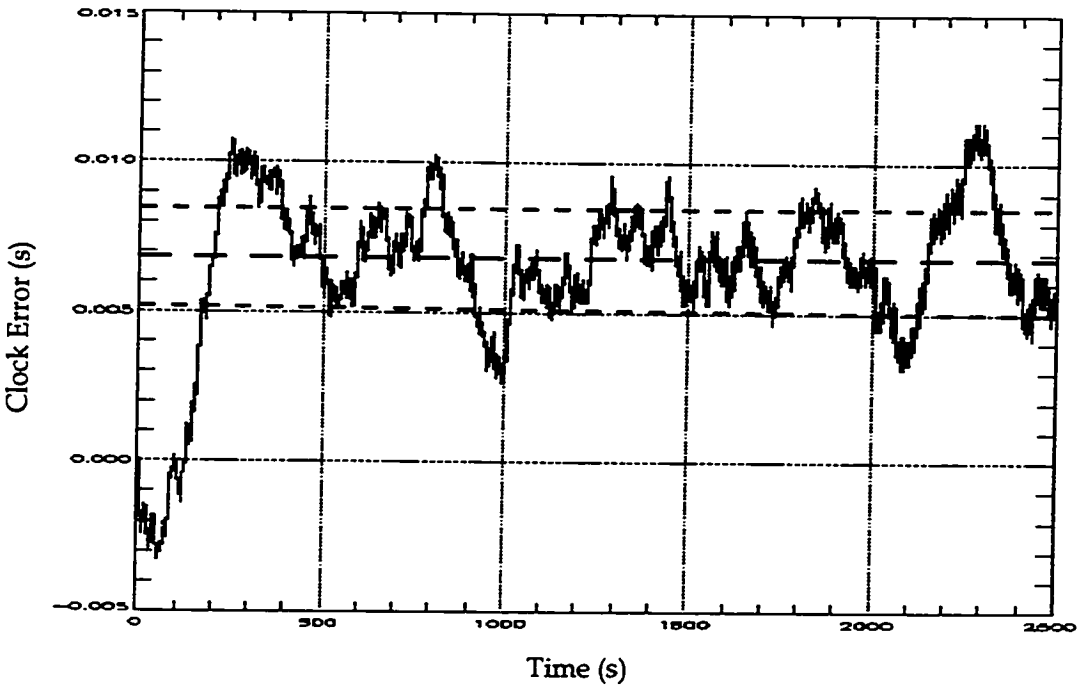

Figure 5.4: PLL Simulated Performance

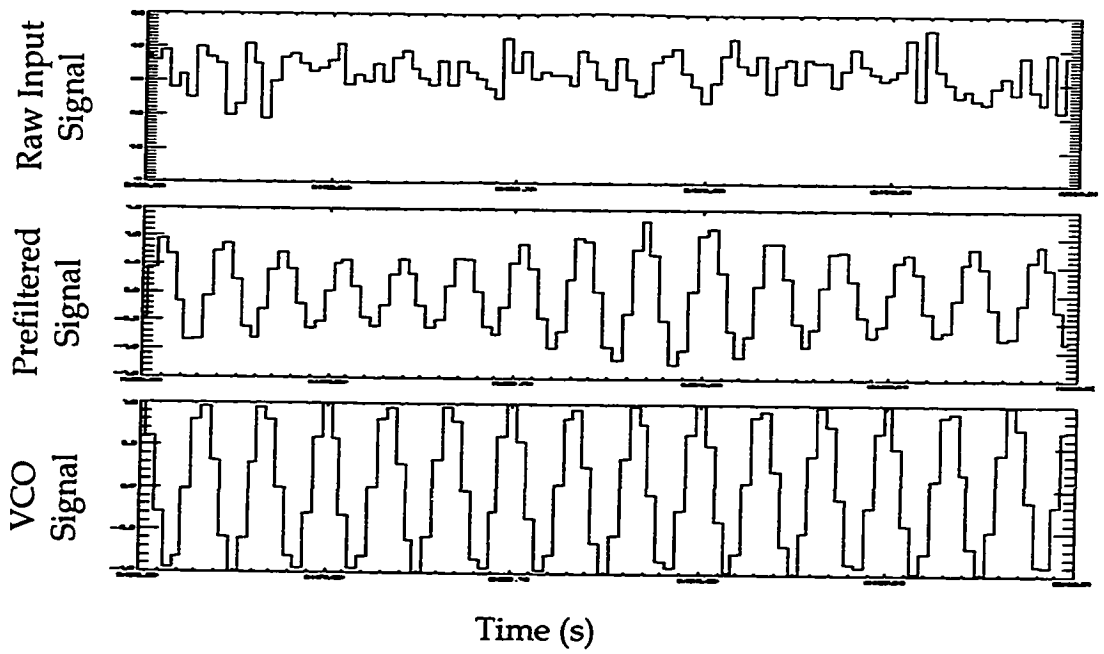

Figure 5.5: PLL Signal Comparison

It is possible that the simulated PLL did not lock onto any signal at all. It may have been able to lock onto noise that, after prefiltering, just appeared to be an input signal at the Crab frequency. In order to guarantee that the PLL simulation actually locked onto a real signal, the simulation was rerun with one exception - the pulse signal amplitude was set to zero. Figure 5.6 shows that the result is a loop that never achieves lock and simply drifts off in time.

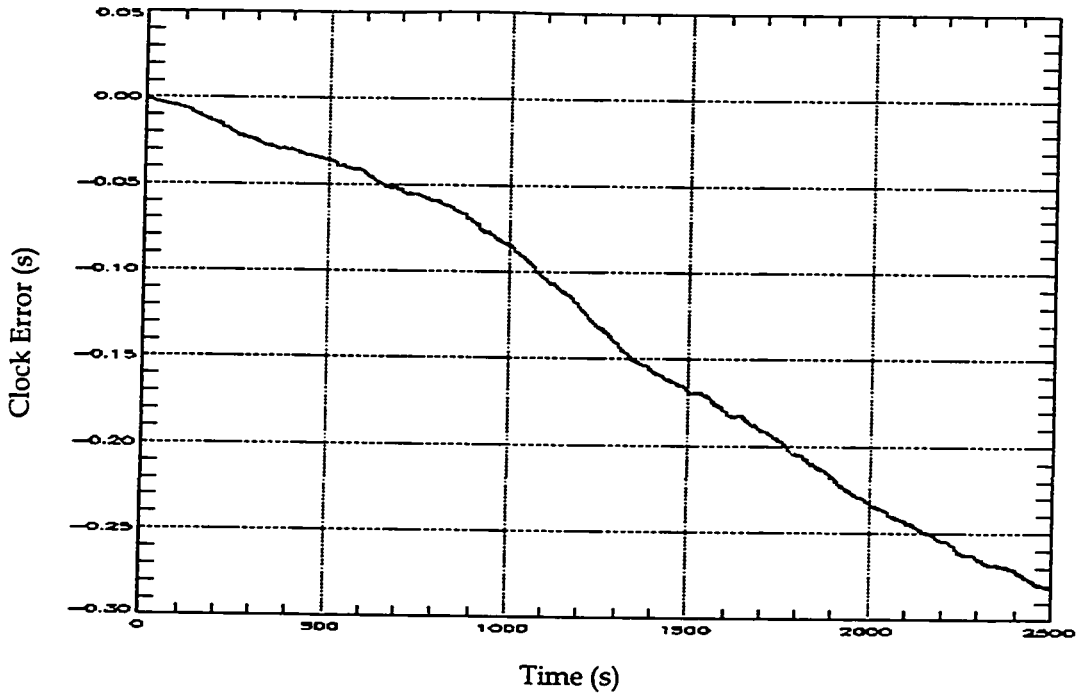

Figure 5.6: PLL Simulated Performance (Zero Pulsar Input)

This simulation has shown that it is possible to use a phase locked loop to track the pulsations of an x-ray pulsar and use that signal as an autonomous time reference. While the performance of this loop is acceptable, its design is certainly not optimum and must be improved before use on the USA Experiment.

Chapter 6: Conclusions and Recommendations

6.1 Conclusions

Emissions from stellar sources in the infrared, optical and ultraviolet wavelengths have been used as the basis for navigating satellites for more than three decades. Emissions in the x-ray regime have characteristics that suggest they also form an excellent basis for determining satellite attitude, time and position. X-ray navigation offers the potential for the autonomous determination of attitude, time and position from a single instrument operating in regimes from low earth orbit to geosynchronous orbit to interplanetary transfer to orbit about other planets. Furthermore, the x-ray regime offers the only fully autonomous measure of time on board a spacecraft.

The launch of the Unconventional Stellar Aspect Experiment in late 1996 will be the first opportunity to demonstrate some of the principles of x-ray navigation.

This thesis serves as a case study for designing, manufacturing and testing experiments for space applications in small, semi-autonomous groups. This has been

done through the structural and thermal design and analysis of the Unconventional Stellar Aspect Experiment.

Furthermore, this thesis is the first exploration of concepts of x-ray navigation. A variety of collimated x-ray instruments have been suggested for use on spinning spacecraft. The performance of a full attitude sensor with a single collimator has been demonstrated by using data from a previous spinning mission called HEAO-1. The improved performance of a dual collimator system was also demonstrated with this data. These instruments can provide attitude estimates with accuracies in the range of 0.01 deg. For more accurate attitude knowledge requirements on slowly spinning vehicles, an imaging x-ray system was considered and limits on the bandwidth of measurements from such a system were estimated. It was shown that exposure times from 0.0008 sec to 1 sec would be required depending on the guide stars in the instrument field of view.

The potential for determining local spacecraft time autonomously was demonstrated by simulating the operation of a phase locked loop with input from the Crab Nebula pulsar. This pulsar has a period of 0.033 seconds and a complex pulse shape. The characteristics of the pulse shape and the Poisson noise associated with the background were included in the simulation. It was shown that a simple PLL design could attain frequency lock with the pulsar in about 500 sec. Lock was maintained with a steady-state error for the length of the simulation without any cycle slip and with a time error of about 0.0015 sec.

6.2 Recommendations for Future Research

While many of the concepts of x-ray navigation have been demonstrated, there is still a great deal of work to be done before x-ray navigation is accepted as a standard method for determining the states of satellites. To this end the following areas of research are suggested to extend this concept:

1. While the USA mission is scheduled for launch in 1997, there is still much work to be done in support of its x-ray navigation mission. Algorithms must be developed to determine the attitude of the spacecraft while using the USA instrument as a scanning collimator. This instrument can also be used to test the idea of identifying guide stars based on their pulsations. Flight code needs to be written for the RH32 to run the algorithms in real time.
   Additionally, further simulations will be required to validate the PLL concept for the USA mission. These include simulations of other x-ray pulsars, the optimization of the PLL design for the USA case and the writing of flight code for the RH32 processor.

2. There is still a vast amount of data from the HEAO mission that can be used to prove the x-ray navigation concept. The pointed mode high bit rate data can be used prove the concept of x-ray timing. There may also be high bit rate data of pulsars where HEAO is in a scanning mode. This data can be used to explore guide star identification concepts as well as x-ray timing on spinning vehicles. Furthermore, this database can be used to demonstrate that the differential x-ray star scanner can be used on guide stars whose intensities show significant temporal variability.

3. This work has barely touched on the limits in accuracy that can be achieved by x-ray star mapper systems. The design of coded masks for and deconvolution techniques for these systems have not been studied. Note that this problem is unique in that a priori information is available to the reconstruction algorithm. The problems associated with manufacturing, calibration and deployment of these instruments must also be addressed.

4. Finally, before these instruments can be used effectively and reliably, a number of design studies need to be performed. How small can we build these instruments? How large should the field of view be? How much power will they require? What are the ultimate performance limits in terms of satellite spin rate and jitter?

Appendix A: Unconventional Stellar Aspect Experiment Interface Control Document

SPACE TEST PROGRAM
FLIGHT P91-1

ICD-907

P91-1/UNCONVENTIONAL STELLAR ASPECT (USA)

Interface Control Document

9 September 1992

F04701-91-C-0090
CDRL A004

Rockwell International
Space Systems Division
Rockwell International Corporation
P.O.Box 7024
Downey, California 90241-7024

1.0 SCOPE

1.1 SCOPE

This Interface Control Document (ICD) defines and controls the design at the interface between the Unconventional Stellar Aspect (USA) Experiment and the P91-1 space vehicle (SV). Experiment ground support equipment (GSE) to Integrated Space Vehicle (ISV) GSE design interfaces are also defined. This ICD is intended to ensure compatibility between the USA and the SV by documenting form, fit, and functional interface agreements required to satisfy design and installation. Ground checkout and launch operations are documented in the Ground Operations Requirements Document (GORD). Launch facility to GSE interfaces are also defined in the GORD. Orbital operations requirements are defined in the Flight Operations Requirements Document (FORD).

The interface requirements specified in this ICD take precedence over experiment requirements stated in the P91-1 contract.

1.2 EXPERIMENT MISSION DEFINITION

The primary objective of the experiment is to test new approaches to the navigation of satellites, based on use of sensors operating in X-ray wavelengths observing celestial sources in those same bands. This calls for observing the brightest X-ray sources in the sky for prolonged periods and making a variety of measurements using X-ray sensors. Navigation of satellites involves being able to determine a state vector that includes: (1) position of the satellite relative to the earth; (2) the time of the satellite; and (3) the satellite orientation. Different kinds of measurements support determination of these quantities. The measurements that are made sometimes characterize the sources themselves (including characterizing physical mechanisms responsible for production of X-ray emission) and other times directly lead to ascertaining one or more of the quantities comprising the state vector. To provide flexibility in scheduling observations and to give access to as many targets of opportunity as possible, it is necessary that the detectors have access to as large an amount of sky as possible. This coupled with the requirement to observe terrestrial sources translates into a wide range of pitch and yaw travel.

The USA experiment will observe sources for cumulative times of up to a month, but it switches from one source to another fairly frequently, typically twice per orbit. The observing program supports a number of different experiments and studies. Both the position and time determination tasks are carried out essentially by measuring X-ray count rates as a function of time and suitable processing the profiles so obtained. In the case of timekeeping, will calls for timing events to considerable precision, it is of central importance to be able to assign X-ray events an absolute time on the order of one microsecond. The celestial sources include precise natural clocks and it is important to time them precisely in order to exploit this feature. Some of these celestial events, such as eclipses, occur only occasionally and observations of them must be made at specific times. Examples of specific tasks include: (1) observation of horizon crossings of X-ray sources; and (2) observation of transitional events such as lunar occultations or eclipses or X-ray sources, particularly pulsars. In addition to the observation of celestial sources for navigation, there are some further tasks that involve observing terrestrial sources.

Examples of these terrestrial observations would include: (1) taking data at VLF ground stations simultaneously with USA observations of an X-ray source to correlate the variation in received VLF signal characteristics such as amplitude or phase with variations in X-ray input; (2) using those results to improve modeling of ionospheric response to ionization input; and (3) looking downward with the X-ray detectors to search for predicted X-ray flux associated with electrons precipitated by VLF signals. Downward-looking data are also used to investigate whether there are variations in X-ray flux from the earth at low latitudes that could serve as diagnostics for local enhancements of ionization or electron precipitation.

1.3 INTERFACE ITEM DESCRIPTION

1.3.1 P91-1 Description. The major elements comprising the P91-1 space vehicle system (SVS) are shown in Figure 1.

1.3.2 USA Experiment Definition. USA consists of two X-ray sensors and a gimballed mounting as shown in Figure 2. Both sensors fit into a 2-axis gimballed pointing assembly (provided by the experimenter). The autonomous navigation experiment computer processes inputs from the X-ray sensors and is part of the central electronics box that is mounted on USA.

The X-ray unit observes celestial sources and makes measurements that can be used for autonomous satellite navigation. The X-ray unit performs three navigation tasks (timekeeping, position determination, attitude or aspect determination), but does not necessarily do all three of these simultaneously. The X-ray unit's principal modes of observation are: (a) measuring the time-varying X-ray output of celestial sources which can be processed to provide an autonomous timekeeping system; (b) observing horizon crossings for autonomous position determination and atmospheric density studies; (c) observing modulations of steady X-ray sources or passage of sources through the field of view for aspect determination; and (d) observation of terrestrial X-ray emission, including some associated with very low frequency (VLF) transmitters. The X-ray emission used for any of these purposes must be within the field of view of the X-ray sensor assembly.

The X-ray sensor assembly consists of a pair of proportional counter units. These units are identical. Each X-ray detector includes a gas supply system to replenish lost detector gas. The collimators have fields of view that do not exceed 1.5 ° x 1.5°(FWHM).

USA's on-board computer is a high performance autonomous navigation experiment computer. It has sufficient computing power to carry out a wide variety of navigational data analysis tasks using data obtained from the on-board sensors as input. Power requirements for this computer are covered within the power budget of the satellite. It is expected that from time to time that new algorithms will be uplinked and loaded in order to refine the navigational methodology.

3.0 USA/SPACE VEHICLE INTERFACE REQUIREMENTS

3.1 GENERAL INTERFACE REQUIREMENTS

The interface requirements specified in these paragraphs apply to USA and the space vehicle and include requirements imposed on the total P91-1 space system resulting from the mission profile.

3.1.1 Operational Orbit. The sun-synchronous orbit is as follows.

Apogee:	450 ± 10 n.mi
Perigee:	450 ± 10 n.mi
Inclination:	98.7 ± 0.06°
Beta Angle:	36±3° beginning-of-life (BOL) with a drift potential to an end-of-life (EOL) beta angle of 15° to 54°
Period of Orbit:	101.6 minutes (nominal)

NOTE: Beta angle is defined as the angle between the orbit plane and the geocentric radial sun position vector as shown in figure 3. The beta angle is defined to be positive if SV motion is counterclockwise when seen from the sun.

3.1.2 On-Orbit Life. The mission supports experiment operations for a service life of one year after space vehicle checkout and test on-orbit. The ISV has an on-orbit design life of three years.

3.1.3 Storage Life. The ISV is be designed such that storage, under controlled conditions as specified in the GORD, may be planned for as long as two years.

3.1.4 Coordinate System. The coordinate system of the ISV is as shown in Figure 4. The origin of the coordinate system is at the centerpoint of the forward (+X) bulkhead (i.e., the ESEX/SV interface is at the origin). **The experimenter established USA coordinate system is shown in Figure 2.**

3.1.4.1 Earth Centered Inertial (ECI) coordinate System. The ECI coordinate system is defined such that the vectors originate at the earth's center. The +Z vector passes through the north pole, the +X vector passes through the vernal equinox (year 2000), and the +Y vector is normal to both the Z and X vectors using the right hand rule ($\hat{Y} = \hat{Z} \times \hat{X}$). See Figure 5.

3.2 STRUCTURE AND MECHANICAL INTERFACES

The interface requirements define the form, fit, and access requirements for the installation of the experiment external and internal to the space vehicle. Structure and mechanical interfaces will be as shown in Figure 6. **Size and shape of the experiment is limited to the envelope shown in Figure 6.**

3.2.1 Loads

3.2.1.1 Static Loads. The specified loads include the steady-state loads applied to the center of gravity of the experiment components. Forces and moments at the experiment/P91-1 interface are defined in Figure 7. Table 1 defines the design loads for the experiment given at the experiment c.g. A factor of safety of 2.0 for experiment primary structure is required if static load testing of the structure is not to be performed. Margins greater than zero are required. **A fracture control analysis per MIL-STD-1522 will be performed by USA for the pressure vessels.**

fiberglass spacers

3.2.2 Stiffness Requirement. **When the experiment is in its launch locked configuration with a rigid clamped interface, the fundamental natural frequency of the experiment is 50 Hz or greater axial and lateral.**

3.2.3 Field-of-Regard and Field-of-View. The field-of-regard and field-of-view of the experiment are in accordance with Figure 8.

3.2.4 Mass Properties. Total weight of the experiment is limited to 453 pounds including growth margin. This weight excludes the SV mating electrical connectors **and** the mounting attach hardware supplied by the SV Contractor. **Reference paragraph 3.5.3 for center of gravity (c.g.) and inertia limits for gimballing components.**

Mass property reports are submitted with additional reports required if there are major changes to the weight, c.g., or inertia data. Weight, c.g.'s and inertias are provided separately for gimballing components and other separately packaged components.

3.2.5 Mounting Provisions. Mounting provisions are as shown in Figure 6. Interfacing footprints, bolt locations and sizes are controlled to within ±0.005 inches. Interfacing **drill** templates are designed and manufactured by Rockwell from dimensional drawings provided by the experimenter. **The interfacing drill templates are** provided to the experimenter.

3.2.5.1 Mounting Surface Finish. Surface finish at each USA to ISV attachment interface is ≤63 microinches.

3.2.5.2 Mounting Surface Flatness. Mounting interface flatness is not applicable since alignment shims and thermal isolation are required at the USA to ISV interface. Shimming is to be provided as needed for installation.

3.2.5.3 Bonding Straps. Bonding strap provisions are as defined in Figure 6.

3.2.6 External Moving Parts. Moving parts are in accordance with Figure 8. The USA moving parts are the two gimballing sensors and the launch lock mechanisms.

3.2.7 Alignment. **USA is aligned to the SV Inertial Reference Unit A (IRU-A) alignment cube.**

3.2.7.1 Alignment Devices. The SV Contractor supplies the equipment **and personnel needed to perform the alignment of the experiment to the SV. USA supplies a mirror cube that has been previously mounted and aligned by USA on the USA detector boresight. The mirror cube will have a clear line-of-sight from the +Y and +Z sides of the SV and will be securely mounted and protected so as to survive ISV level acoustic and thermal vacuum testing without loss of calibration to the boresight. The mirror cube, shown in Figure 6, may be removed at the experimenter's discretion, after final alignment verification.**

3.2.7.2 Alignment Accuracy. USA is aligned to the SV **IRU-A alignment cube to an alignment accuracy within 0.5 degrees.**

3.2.7.3 Alignment Knowledge. Alignment **in 2 axes prior to shipment launch site is measured within an accuracy of one arc-minute with respect to the IRU-A alignment cube.**

3.2.8 Interface Materials

3.2.8.1 Space Vehicle/USA Interface. The SV/USA interfacing materials, mounting fasteners, and electrical bonding provisions are shown in Figure 6.

3.5.4 Scan Profile. All USA pointer motions have the same general form, although the details of how much and how fast each axis moves depends on what task is being performed. The four general types of motion are track, slew, raster scan, and special. *All* pointer velocity changes are made with an acceleration/deceleration of 2°/min/sec until the final angular velocity is reached. The acceleration maintains the disturbance torque about each axis below 2 oz-in. The maximum rotation rate is 20°/min. One or two axes may be driven depending on the type of motion being performed. For the track mode the pitch drive accelerates to 4°/min and remains at that value with minor deviations to correct for changes in the satellite attitude until the end of the observation, typically 15 to 20 min; after the observation the drive decelerates to zero velocity. During the typical observation the yaw drive operates only sporadically to correct for attitude errors. During a slew both drives accelerate to the maximum velocity of 20°/min until the next target is reached. There is typically a rotation of 90° to 120° about the pitch axis. The motion about the yaw axis is determined by the relative positions of the two targets and is typically between 0° and 90°. The raster scan mode has a pitch drive velocity of between 0° and 4°/min; the yaw drive accelerates to a maximum of approximately 10°/min for total travel of approximately 10° to 15°, then decelerates, reverses direction, and accelerates back to its previous rate of rotation in the opposite direction. It continues this procedure for the duration of the observation. The special observation modes are used to track vehicles or terrestrial targets and involve motions about one or both axes at rates less than 20°/min.

3.6 THERMAL CONTROL

The SV thermal control subsystem is designed and tested per MIL-STD-1540B protoflight levels. Experiments thermal control subsystems are designed and tested (qualification and acceptance) to experiment specific requirements.

3.6.1 USA/Space Vehicle Thermal Interface. The experiment/SV thermal interface schematic is presented in Figure 17. The parameters controlled by the experiment those controlled by the Space Vehicle as well as parameters affected by both experiment and SV, are identified in Figure 17. Thermal isolation interfacing hardware is shown in Figure 6.

3.6.2 Interface Temperature and Heat Flux Limits. The allowable temperature limits and heat transfer rates at the thermal interface during on orbit operation are per Table 2.

3.6.3 USA Allowable Temperature Limits. The experiment component operating and non-operating allowable temperatures are included in Table 2. The power dissipation levels are as shown in the power profile (Figure 14 and in Section 3.3.2.1.1).

3.6.4 Thermal Control Coatings, Materials, Surface Treatment and Restrictions. The selection and specification of the external coatings on the experiment and on the SV surfaces affecting USA thermal control is to be coordinated between the experiment and SV contractors.

All thermal control materials, i.e., multilayer insulation, paints, tapes, adhesives, etc., are of flight proven quality with outgassing properties for weight loss and Collected Volatile Condensable Material (CVCM) compatible with the outgassing criteria as defined in the P91-1 Contamination Control Plan (Section 4.2.3).

USA multilayer insulation (MLI), heaters and space radiators are provided and installed on the instrument by the experimenter prior to delivery to the SV contractor for integration with the SV.

3.7 ACTUATORS

No electroexplosive devices are used by the USA, however paraffin actuators are used to release the 2 axis gimbal and are controlled by USA via the 1553 bus. The release is fail safe, requiring 2 commands for release.

3.8 SAFETY REQUIREMENTS

The experiment meets the requirements of WSMCR 127-1, CSTCR 127-1 and the P91-1 System Safety Program Plan when the experiment is attached to the SV. The experimenter is required to support the SV contractual safety reviews. Experiment inputs to the P91-1 Hazard Analysis Reports are defined in Table 6.

The Certification of Safety is included in the Certificate of Compliance (Table 4). The launch site or factory safety training requirements which are applicable to the experimenters are specified in the GORD.

A Failure Mode Effects Analysis (FMEA) of the experiment interface is required. The purpose of the FMEA is to verify that failure of an experiment does not cause failure of the SV including the 1553 interface bus, or another experiment. The failure effects analyzed are limited to the SV to experiment interface. MIL-STD-1629, Task 101, provides guidance for this task.

3.8.1 Design Criteria. The experiment is designed to preclude any operation, event, condition, or failure that could cause detectable or undetectable malfunctions or damage to P91-1, damage to other equipment, injury to personnel, or damage to facilities.

3.9 FLIGHT ENVIRONMENT

The following parameters represent the induced flight environments to which the interfacing experiment is exposed during ascent and earth orbit. The experiment is expected to survive and/or operate when exposed to any feasible combination of those parameters encountered from ascent through mission operation.

3.9.1 Acoustic. Maximum predicted flight acoustic environment is shown in Figure 18.

3.9.2 Vibration. Predicted random and sinusoidal flight vibration levels for the space vehicle side of the USA interface are as shown in Figure 19.

3.9.3 Shock. The predicted pyro shock levels at the SV/experiment interface are expected to be within the envelope as shown in Figure 20.

3.9.4 Depressurization and Repressurization. The payload fairing (PLF) gaseous environment consists of residue remaining from the ground purge conducted prior to lift-off. The nominal PLF pressure during ascent is shown in Figure 21.

3.9.5 Effect of External Magnetic Fields. No instrument sensitivity to magnetic fields of up to 2 Gauss have been identified.

3.9.6 Radiation Environment. The total radiation dose for the three year mission is about 1.5×10^4 rads behind nominal (100 mil aluminum) shielding. Figures 22 and 23 provide the total dose and single event radiation environments.

3.9.7 Free Molecular Heating. Free molecular heating at fairing separation is less than 0.1 BTU/ft^2-sec. The free molecular heating rate history is shown in Figure 24.

3.10 Test Environment. The ISV is subjected to those tests described in the GORD. Tests are to be conducted to the protoflight levels as defined in MIL-STD-1540.

3.11 Flight Contamination Limits. The experimenter controls their flight contamination below the level budgeted in the P91-1 Contamination Control Plan, Section 4.1. The experimenter controls and directs venting from experiment enclosure to prevent impingement of outgassed products on any ISV sensitive surface.

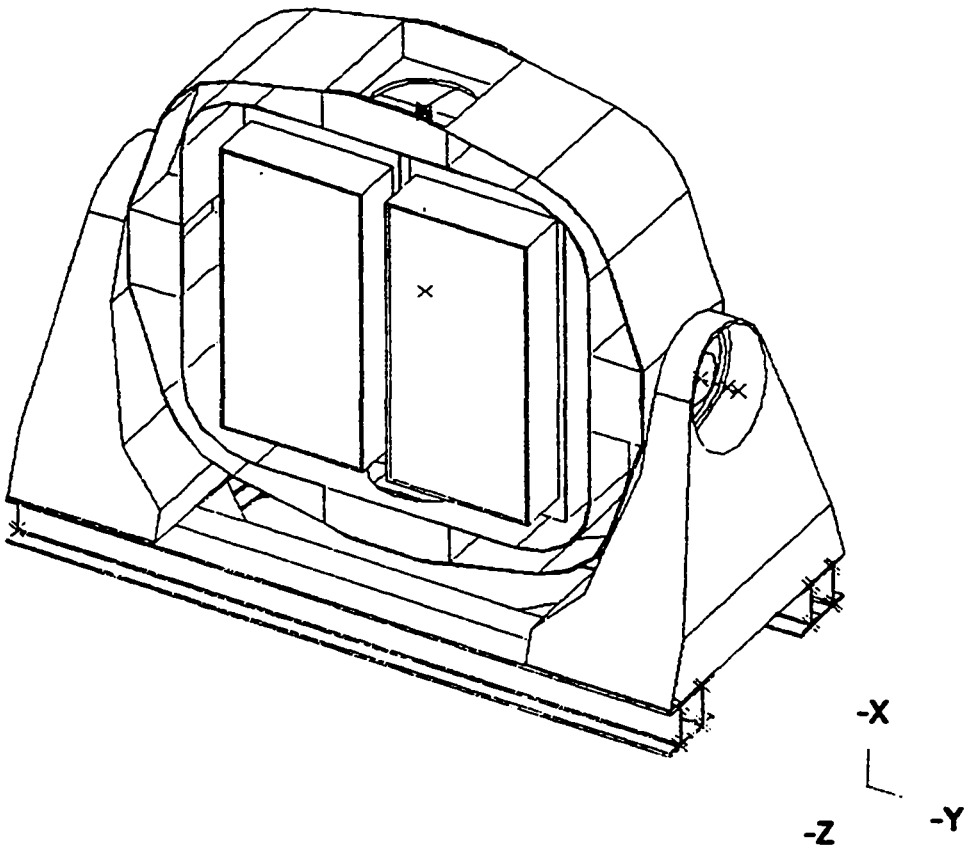

Figure 2. USA Experiment

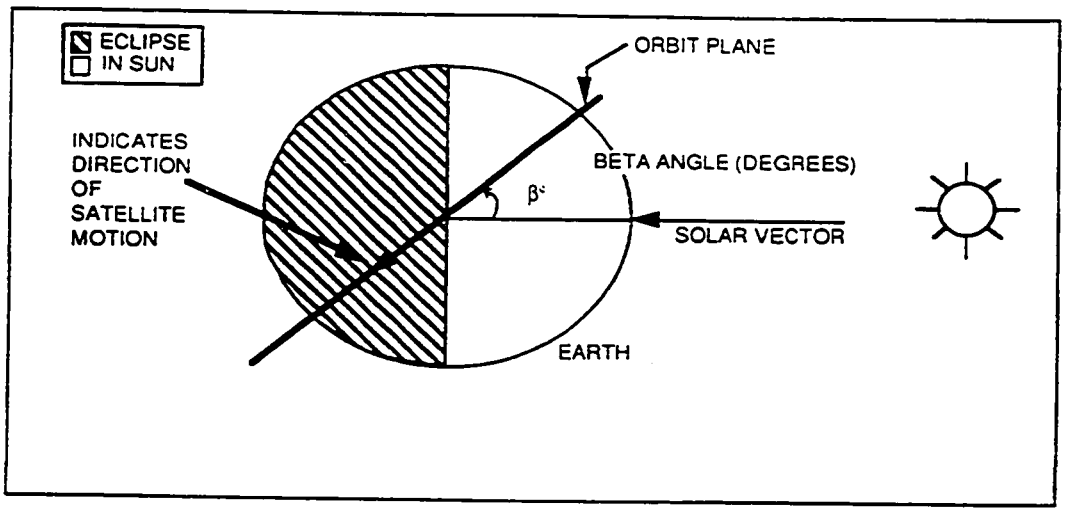

Figure 3. Beta Angle Illustration

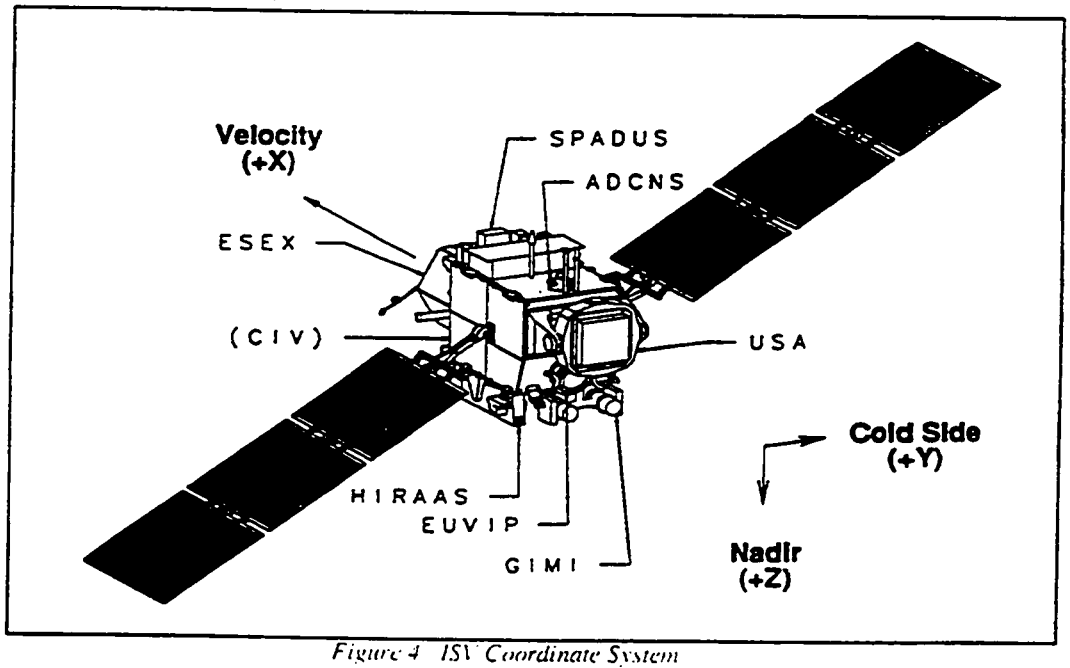

Figure 4 ISV Coordinate System

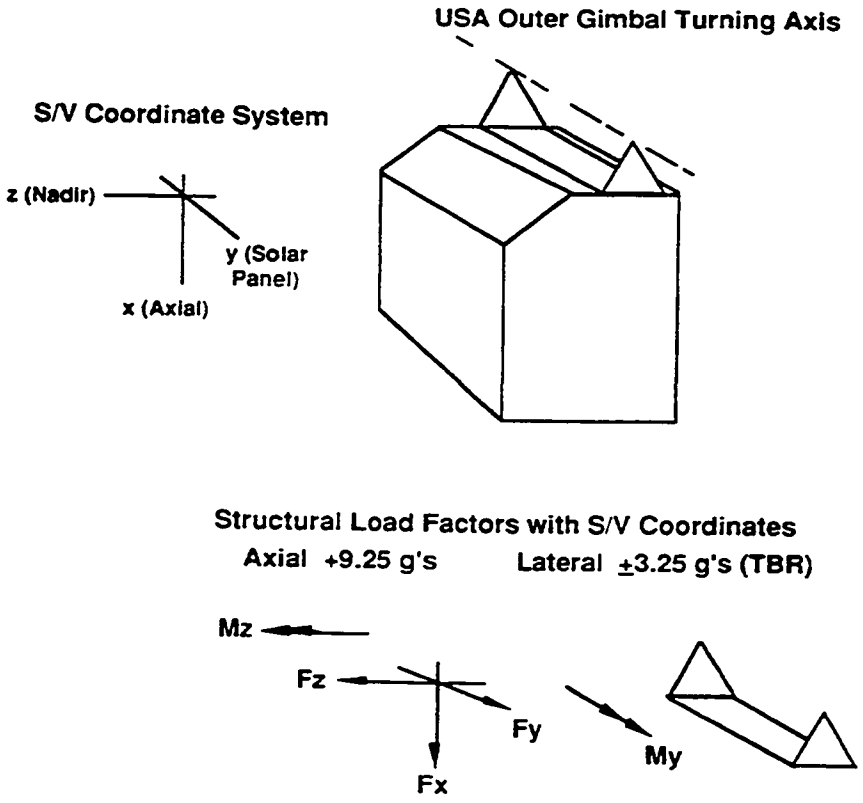

Figure 7. Interface Forces & Moments

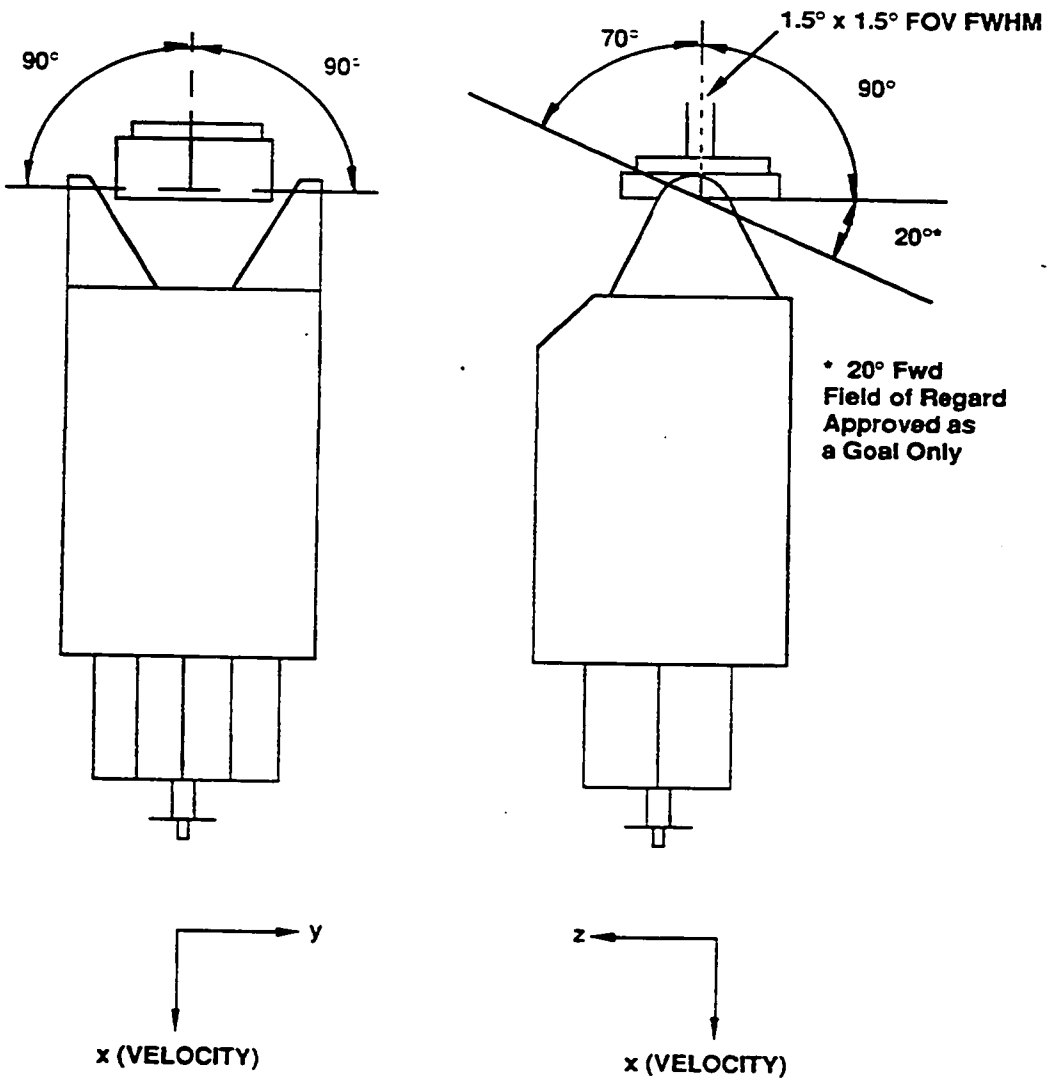

Figure 8. USA Field-of-Regard

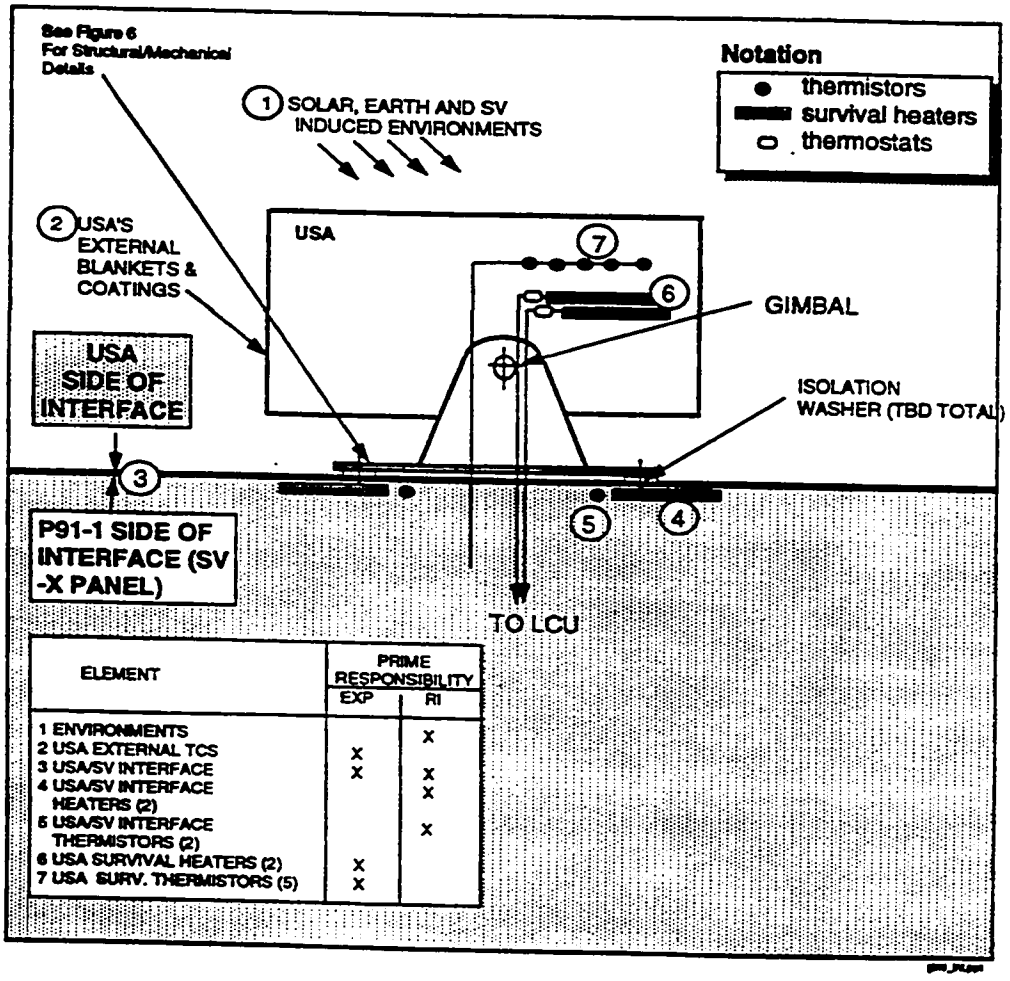

Figure 17. USA/SV Thermal Interfaces

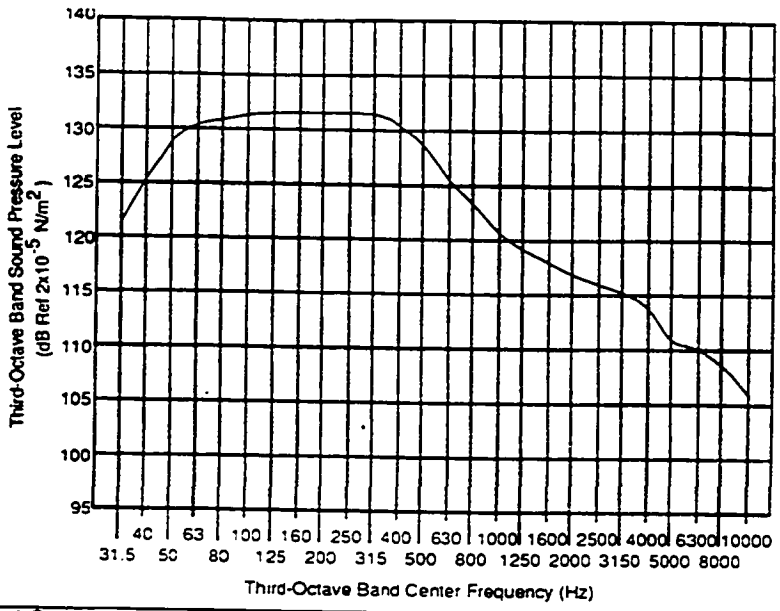

One Third Octave Band Center Frequency (Hz)	Maximum Flight Levels (dB)
31.5	121.0
40	125.0
50	128.0
63	129.5
80	130.5
100	131.0
125	131.0
160	131.0
200	131.0
250	131.0
315	131.0
400	130.5
500	129.0
630	126.0
800	123.0
1000	121.0
1250	119.0
1600	118.0
2000	117.5
2500	117.0
3150	116.0
4000	114.5
5000	112.0
6300	110.0
8000	108.5
10000	107.0
OASPL = 141.3 dB	

Figure 18. Acoustic Spectra

Sinusoidal Vibration		
Frequency (Hz)		Level (g_{o-p})
• Thrust Axis	5-6.2	0.5-in. D.A.
	6.2-100	1.0
• Lateral Axes	5-100	0.7
Notes: Accelerations apply at payload attach fitting base during testing. Responses at fundamental frequencies should be limited based on vehicle coupled loads analysis.		

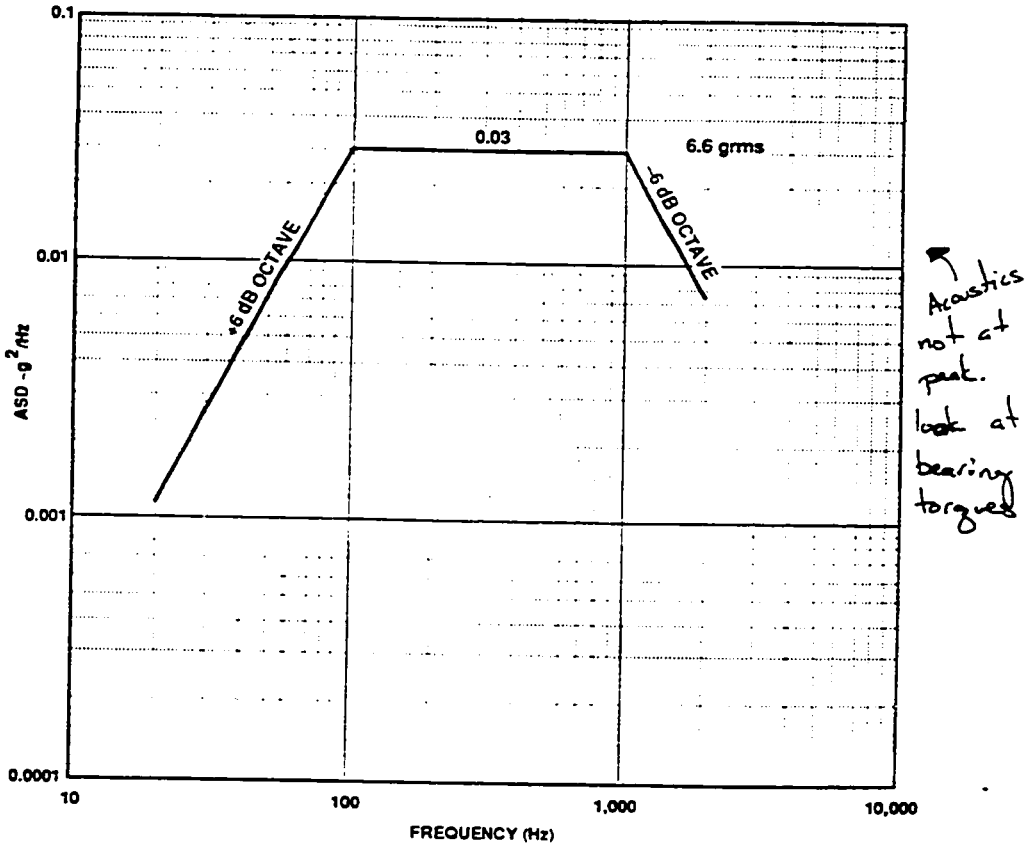

Figure 19. Maximum Predicted Flight Vibration Levels

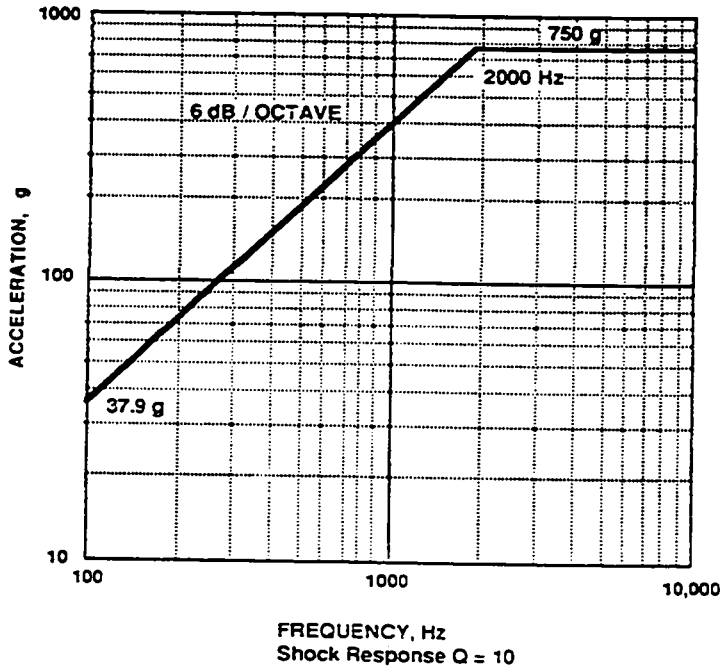

Figure 20. Predicted Pyro Shock Level at USA/SV Interface

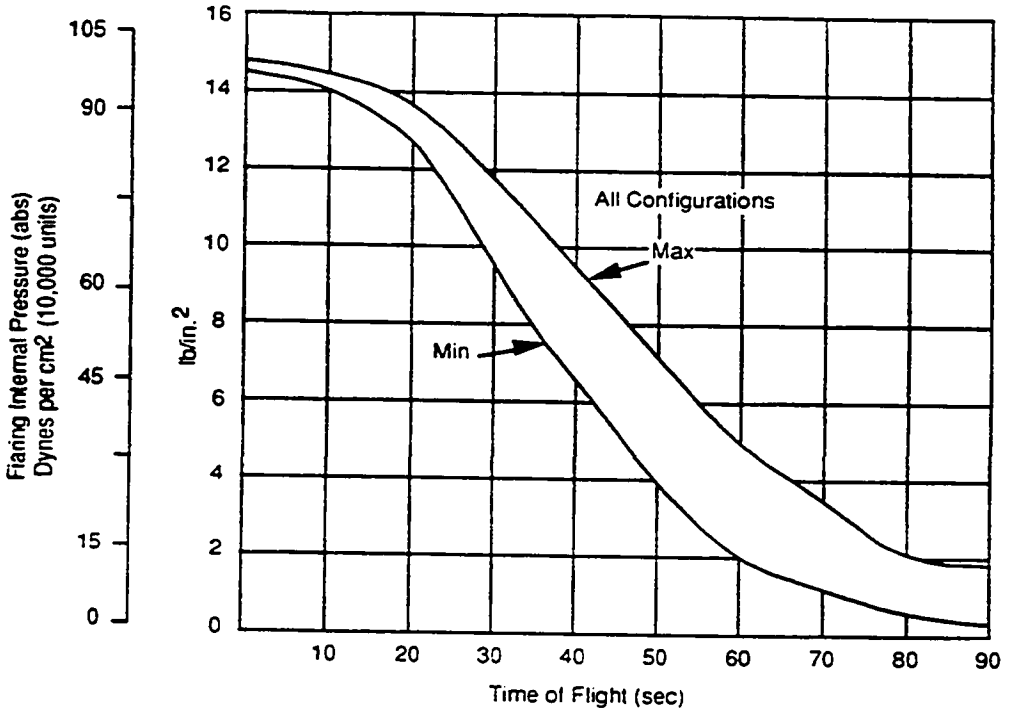

Maximum Rate of Change: -0.5 PSI/SEC
Maximum Rate Over a 5 SEC Interval: 0.4 PSI/SEC

Time of Flight (sec)	Min Pressure (psi)	Max. Pressure (psi)
0	14.5	15.0
10	14.1	14.6
20	12.7	14.3
25	11.4	13.8
30	9.8	13.4
35	7.9	12.8
40	6.4	12.2
45	5.1	11.5
50	3.9	10.7
55	3.0	9.8
60	2.2	8.9
70	1.1	7.1
80	0.6	5.2
90	0.4	3.4

Figure 21. Pressure Levels Decay

Table 1. Design Limit Flight Accelerations, g(s)

	Axial	Lateral
Lift Off	+4.55 / -.26	±3.25 (TBR) ± 4.50
Main Engine Cut Off	+9.25	±.13

Note: (-) Tension (+) Compression
Limit loads include dynamic amplification of the ISV structure.

Table 2. USA/SV Interface Component Allowable Temperatures and Interface Heat Flow Limits

	OPERATIONAL			SURVIVAL			ACCEPTANCE		PROTOFLIGHT	
COMPONENT	MIN (C)	MAX (C)	HEAT FLOW (W)	MIN (C)	MAX (C)	HEAT FLOW (W)	MIN (C)	MAX (C)	MIN (C)	MAX (C)
USA/SV Interface	-20	40	13**	-20	40	-12	N/A	N/A	N/A	N/A
The following temperatures are listed for Reference Only, e.g., thermal vacuum test										
Electronics	-13	50	*	-29	66	*	-24	61	-29	66
Detectors/Viton Seals	0	50	*	-15	66	*	-10	61	-15	66

*See Section 3.3.2.1.1 for Power Dissipation

**(+) Heat Flow is to SV; (-) Heat Flow is to Experiment

rerun launch lock analysis w/ lower axial load.

Appendix B: Selected Astrogravity Notes

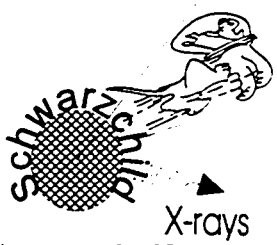

Astrogravity Note # 14
Han Wen
SLAC
September 22, 1994

Determining Dead Time

We derive a simple analytic expression for the dead time[1] and verify its form with a Monte Carlo simulation. The only assumptions we make is that the distribution of counts follows Poisson statistics and that the dead times are nonparalyzable.

We may relate the count rate, $\mathcal{N}$ to the time interval probability density function, $f(T)$ in the following manner.

$$\frac{1}{\mathcal{N}} = \langle T \rangle = \int_0^\infty T f(T) dT \tag{1}$$

where T is a time interval. Assuming Possion statistics,

$$P_P(n, \mathcal{N}T) = \frac{(\mathcal{N}T)^n e^{-\mathcal{N}T}}{n!} \tag{2}$$

we may determine $f(T)$ by considering the probability of having a time interval $T' \leq T$.

$$\begin{aligned} P(T' \leq T) &= \sum_{n=1}^{\infty} P_P(n, \mathcal{N}T) \\ &= 1 - P_P(0, \mathcal{N}T) \\ f(T) &= \frac{dP(T' \leq T)}{dT} \\ \Rightarrow &\boxed{f(T) = \mathcal{N} e^{-\mathcal{N}T}} \end{aligned} \tag{3}$$

[1] Muller, NIM 112 (1973) pgs. 47-57

If we turn on a dead time, τ to determine the ***observed*** count rate, $\mathcal{N}_o$ using eq. (1) we need to transform $f(T)$ to the observed time interval density, $f_O(T)$. We expect to $f_O(T)$ take the form,

$$f_o(T)\begin{cases}=0, & T<\tau\\ \propto f(T), & T\geq\tau\end{cases}$$
$$\Rightarrow\quad f_o(T)\propto U(T-\tau)f(T)$$

where $U(T-\tau)$ is unit-step function. Requiring that the integral of $f_O(T)$ be normalized to one determines the normalization to be:

$$f_o(T)=U(T-\tau)f(T-\tau)$$
$$\Rightarrow\quad \boxed{f_o(T)=U(T-\tau)\mathcal{N}e^{-\mathcal{N}(T-\tau)}} \tag{4}$$

Plugging this into eq. (1) gives,

$$\frac{1}{\mathcal{N}_o}=\int_0^\infty Tf_o(T)dT$$
$$=\frac{e^{\mathcal{N}T}}{\mathcal{N}}\int_{\mathcal{N}T}^\infty xe^{-x}dx$$
$$=\frac{1+\mathcal{N}T}{\mathcal{N}}$$
$$\Rightarrow\quad \boxed{\mathcal{N}_o=\frac{\mathcal{N}}{1+\mathcal{N}T}},\quad \boxed{\mathcal{N}=\frac{\mathcal{N}_o}{1-\mathcal{N}_oT}} \tag{5}$$
$$\Rightarrow\quad \boxed{f_{dead}=\frac{\mathcal{N}-\mathcal{N}_o}{\mathcal{N}}=\tau\mathcal{N}_o} \tag{6}$$

We verified the function form of the fractional dead time, eq. (6) by performing a Monte Carlo simulation of a Poisson process using a set dead time. Using the Poisson time interval probability distribution, eq. (3) we generated a series of relative separation times for a given count rate, $\mathcal{N}$. The distribution of these relative separation times, namely, $f(T)$ is shown in Fig. 1.

By summing the counts which did ***not*** fall within the dead time of previous counts we determine the ***observed*** count rate, $\mathcal{N}_o$ for this simulation. Plots of the resulting fractional dead times vs. $\mathcal{N}_o$ for two dead times, 11μs and 40μs are shown in Figs. 2-3. Both plots show a linear relationship between the fractional dead time and $\mathcal{N}_o$ with fitted slopes agreeing with eq. 6, namely, equalling their set dead times, respectively.

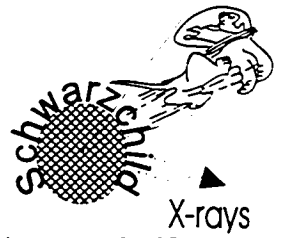

Astrogravity Note # 17
John Hanson
SLAC
March 14, 1996

USA Structure Test Program

Introduction

In support of the Unconventional Stellar Aspect Experiment (USA), SLAC has designed, manufactured, and tested the gimbal support structure for the experiment. Constructed from 6061/T6 aluminum, this structure was assembled using a process called dip-brazing. An integral part of this effort was the test program that occurred simultaneously with the design and manufacturing processes.

Test Program

The concurrent design, manufacturing and testing program that was applied to the USA experiment is summarized below:

1. Finite element modelling:

The USA structure was modelled with the CAEDS/IDEAS software package published by IBM and SDRC. The work will be described in a subsequent AstroGravity note.

2. Construction to established specifications:

All dip-brazing was done by Aluminum Dip Braze Co. (ADB) in Burbank, Ca. This work was done in accordance with Mil-B-7553-B Type V Grade B with quality standards per Mil-I-45208. All joint preparation was done to Mil-B-7553-B Type V Grade A specifications. Following the dip-brazing process, all parts were heat-treated to attain T6 conditions. All dip-brazed joints were then inspected radiographically and the results interpreted to determine the fractional braze wetting of each joint. Certifications of Conformance are on file with radiographs for all parts.

3. Manufacturing qualification:

Because the dip-brazing process is relatively new to the aerospace community, a series of qualification test samples were built by ADB and tested to failure at SLAC. This work is described in detail in AstroGravity Note #18.

4. Prototype pylon and flight articles:

After qualifying the manufacturing process, one prototype pylon was manufactured by ADB to prove the overall manufacturing concept. This pylon would later be subjected to a static load test. Only after visual and radiographic inspections of the prototype pylon were performed were the flight articles manufactured. The flight articles included two pylons and one yoke.

5. Quality assurance pull samples:

Each item dip-brazed by ADB was accompanied by five shear samples similar to those used in the manufacturing qualification process. These samples were prepared in the same manner and to the same specification as the prototype and flight articles and were brazed in the same bath and at the same time as their parent articles. The results of these tests are described in AstroGravity Note #19.

6. Static Load Test

As a final test of the USA structure, the prototype pylon was used in a static load test that subjected the pylon to 115% of the USA ICD loads. This test is described in detail in AstroGravity Note #20.

Test Summary

The results of all facets of the USA structural test program are summarized below (Table 1).

Test	Pylon 1 (Prototype)	Pylon 2 (Flight)	Pylon 3 (Flight)	Yoke (Flight)
Manufacturing Qualification Pull Samples	6892 psi Mean Shear Strength	6892 psi Mean Shear Strength	6892 psi Mean Shear Strength	6892 psi Mean Shear Strength
Certification of Conformance	On File	On File	On File	On File
Radiographic Inspection	70% min 75% avg	70% min 85% avg	70% min 85% avg	60% min 70% avg
Quality Assurance Pull Samples	6973 psi Mean Shear Strength	6491 psi Mean Shear Strength	6341 psi Mean Shear Strength	6037 psi Mean Shear Strength
Static Load Test	Passed	N/A	N/A	N/A

Table 1: USA Test Program Summary

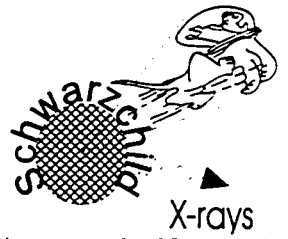

Astrogravity Note # 18
John Hanson
SLAC
October 10, 1994

USA Dip Brazing Manufacturing Qualification

Introduction

The primary support structure for the Unconventional Stellar Aspect Experiment makes extensive use of a bonding process known as dip-brazing in its manufacturing. Two pylons and one yoke are to be assembled from components made of 6061/T6 aluminum that are dip-brazed together. In order to ensure that dip-brazed joints will have sufficient strength to survive the launch environment, a number of qualification braze joints were tested.

Test Samples

Two types of joints were tested: eight shear samples and eight tensile samples. Figures 1 and 2 show the dimensions of the shear and tensile samples, respectively. All samples were made from 6061/T6 aluminum. The test samples were dip-brazed by the Aluminum Dip Braze Co. of Burbank, Ca. All manufacturing was done to Mil-B-7883-B Type V Grade B with joint preparation to Mil-B-7883-B Type V Grade A. The samples were then machined to the final configuration shown in Figure 3.

Test Results

All samples were tested to failure using a tensile test machine in the Material Science Department of Stanford University. All test sample failure modes were brittle failure of the braze joint. The resulting failure loads are summarized in Table 1.

The strength of the braze joints are sufficient for the USA experiment, with mean joint failure stresses of 6892 psi for the shear samples and 7722 psi for the tensile samples. Note, however, that due to the orientation of the braze joint relative to the load direction, the shear samples were capable of carrying more than twice the load of the tensile samples. Inspection of the bonding surfaces of the destroyed samples indicated

that each bond joint was only 20% to 30% wetted. Discussions with the manufacturer revealed that the samples were not manufactured with the Class A brazing preparation. The prototype pylon, flight articles and their respective validation samples will be manufactured to this specification and certification of this process will be provided.

Conclusions

While the qualification braze joints were not manufactured to the level of quality originally anticipated, their strength was sufficient to provide the USA gimbal structure design with a positive margin of safety. One prototype pylon, two flight pylons and one flight yoke will now be built by the Aluminum Dip Braze Co.

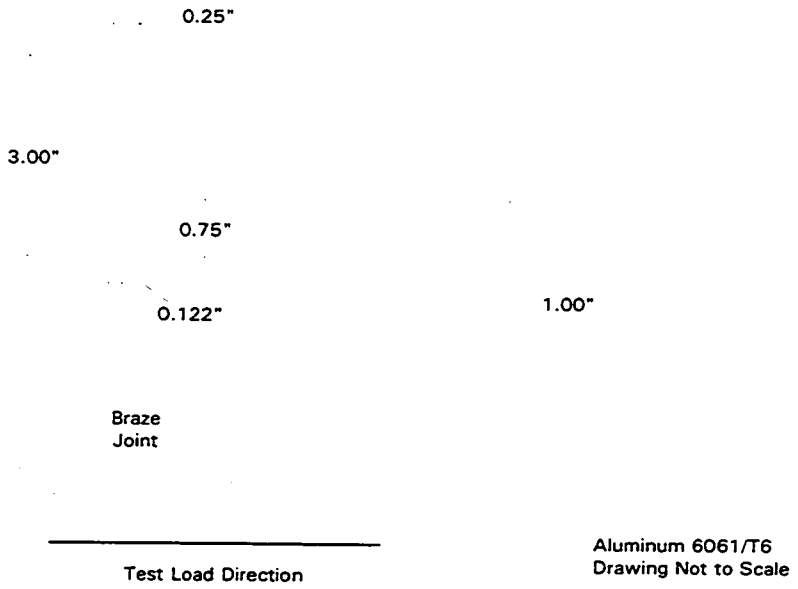

Figure 1: Shear Sample Specifications

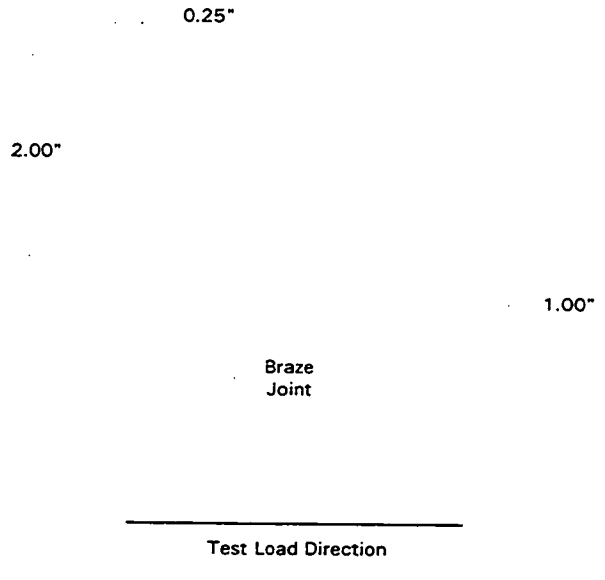

Figure 2: Tensile Sample Specifications

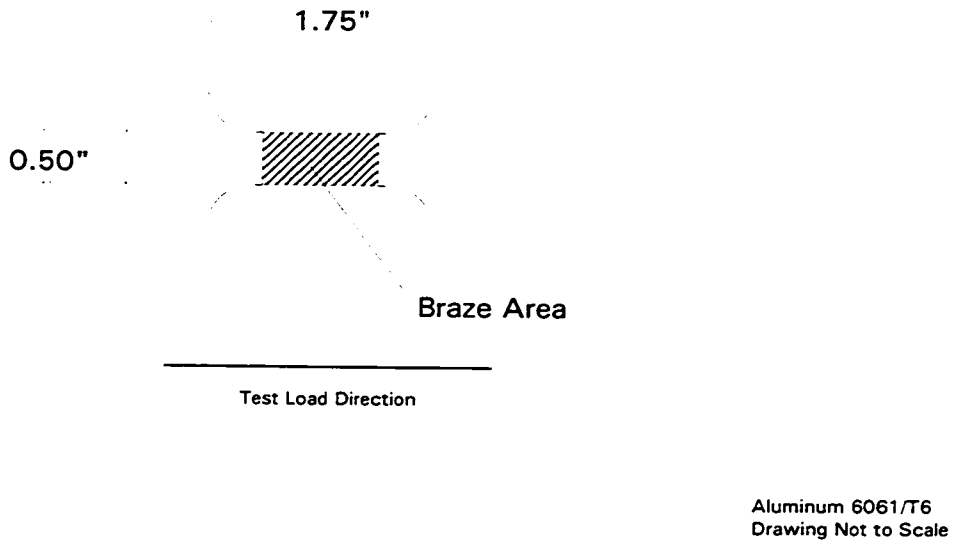

Figure 3: Final Shear Sample Configuration

Sample	Width (in)	Thickness (in)	Area (sq. in.)	Failure Load (lb)	Failure Stress (psi)	Shear Stress (psi)
10	0.503	0.241	0.121	2200	18148	5832
12	0.500	0.242	0.121	2950	24380	7867
13	0.501	0.239	0.120	2760	23050	7345
14	0.504	0.238	0.120	2150	17924	5688
15	0.499	0.240	0.120	2150	17953	5745
17	0.500	0.240	0.120	2900	24167	7733
18	0.503	0.240	0.121	2900	24023	7687
19	0.501	0.239	0.120	2720	22716	7239
			Average	2961	21545	6892
			Std Dev	360	2982	964

Table 1a: Shear Sample Results

Sample	Width (in)	Thickness (in)	Area (sq. in.)	Failure Load (lb)	Failure Stress (psi)
10	0.501	0.235	0.118	950	8069
11	0.499	0.247	0.123	1160	9412
12	0.504	0.247	0.124	690	5543
14	0.503	0.245	0.123	1210	9819
15	0.502	0.243	0.122	1020	8362
16	0.503	0.246	0.124	890	7193
17	0.501	0.248	0.123	770	6197
19	0.500	0.245	0.123	880	7184
			Average	946	7722
			Std Dev	179	1484

Table 1b: Tensile Sample Results

Notes:

1. Samples constructed of Al 6061/T6
2. Al 6061/T6 has an ultimate strength of 45,000 psi
3. All failure were brittle fracture of the joint
4. Error in failure loads due to testing ~10% of nominal

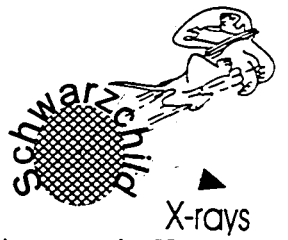

Astrogravity Note # 19
John Hanson
SLAC
March 14, 1996

USA Structure
Quality Assurance Testing

Introduction

The primary support structure for the Unconventional Stellar Aspect Experiment makes extensive use of a bonding process known as dip-brazing in its manufacturing. Two pylons and one yoke are to be assembled from components made of 6061/T6 aluminum that are dip-brazed together. In order to ensure that dip-brazed joints will have sufficient strength to survive the launch environment, a number of qualification braze joints were tested.

Test Samples

Qualification pull samples were manufactured with each prototype and flight article. Five shear samples were tested with each item (see Figure 1). All samples were made from 6061/T6 aluminum. The test samples were dip-brazed by the Aluminum Dip Braze Co. of Burbank, Ca. All manufacturing was done to Mil-B-7883-B Type V Grade B with joint preparation to Mil-B-7883-B Type V Grade A. A total of four sets of five samples were made.

Test Results

All samples were tested to failure using an Instron Model 1125 tensile test machine in the Material Science Department at Stanford University. This machine had a maximum applied load of 20,000 lb and was calibrated at 10,000 lb. All test sample failure modes were brittle fracture of the braze joint. the resulting failure loads are summarized in Table 1. The mean failure loads will be used in the final structural analysis report to determine the design margin of safety.

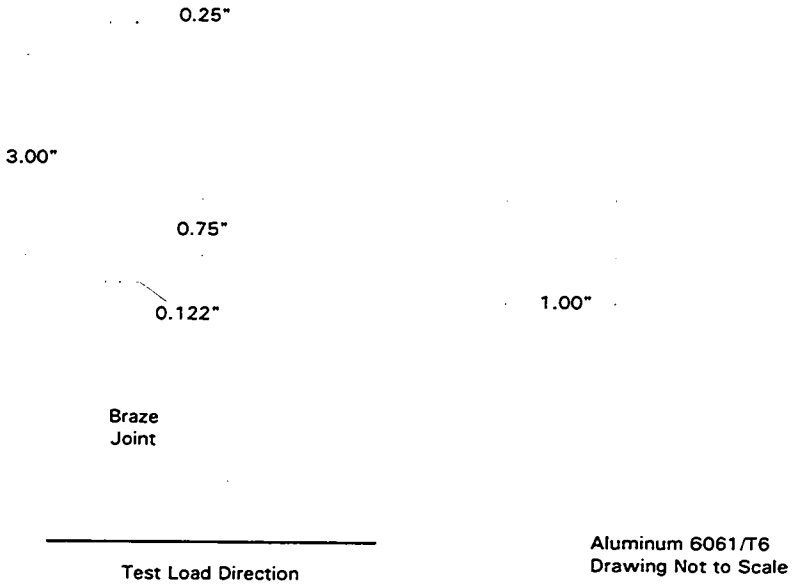

Figure 1: Shear Sample Specifications

Sample	Depth (in)	Width (in)	Thickness (in)	X-Section Area (in^2)	Braze Area (in^2)	Failure Load (lb)	Shear Stress (psi)	Tensile Stress (psi)
1	0.75	1.00	0.25	0.25	0.75	4500	6000	18000
2	0.75	1.00	0.25	0.25	0.75	4820	6427	19280
3	0.75	1.00	0.25	0.25	0.75	6350	8467	25400
4	0.75	1.00	0.25	0.25	0.75	4460	5947	17840
5	0.75	1.00	0.25	0.25	0.75	6020	8027	24080
				Average		5230	6973	20920
				Std Dev		891	1187	3562

Table 1a: Pylon #1 Qualification Samples

Sample	Depth (in)	Width (in)	Thickness (in)	X-Section Area (in^2)	Braze Area (in^2)	Failure Load (lb)	Shear Stress (psi)	Tensile Stress (psi)
1	0.75	1.00	0.25	0.25	0.75	5160	6880	20640
2	0.75	1.00	0.25	0.25	0.75	4290	5720	17160
3	0.75	1.00	0.25	0.25	0.75	5220	6960	20880
4	0.75	1.00	0.25	0.25	0.75	4770	6360	19080
5	0.75	1.00	0.25	0.25	0.75	4900	6533	19600
				Average		4868	6491	19472
				Std Dev		372	496	1488

Table 1b: Pylon #2 Qualification Samples

Sample	Depth (in)	Width (in)	Thickness (in)	X-Section Area (in^2)	Braze Area (in^2)	Failure Load (lb)	Shear Stress (psi)	Tensile Stress (psi)
1	0.75	1.00	0.25	0.25	0.75	4530	6040	1812-
2	0.75	1.00	0.25	0.25	0.75	4190	5587	16760
3	0.75	1.00	0.25	0.25	0.75	4890	6520	19560
4	0.75	1.00	0.25	0.25	0.75	5000	6667	20000
5	0.75	1.00	0.25	0.25	0.75	5170	6893	20680
				Average		4756	6341	19024
				Std Dev		394	525	1575

Table 1c: Pylon #3 Qualification Samples

Sample	Depth (in)	Width (in)	Thickness (in)	X-Section Area (in^2)	Braze Area (in^2)	Failure Load (lb)	Shear Stress (psi)	Tensile Stress (psi)
1	0.75	1.00	0.25	0.25	0.75	5920	7893	23680
2	0.75	1.00	0.25	0.25	0.75	4190	5587	16760
3	0.75	1.00	0.25	0.25	0.75	3460	4613	13840
4	0.75	1.00	0.25	0.25	0.75	4760	6347	19040
5	0.75	1.00	0.25	0.25	0.75	4310	5747	17240
				Average		4528	6037	18112
				Std Dev		907	1210	3630

Table 1d: Yoke Qualification Samples

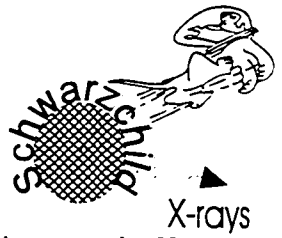

Astrogravity Note # 20
John Hanson
SLAC
March 14, 1996

USA Pylon Static Load Test

Introduction

The Unconventional Stellar Aspect Experiment (USA) is an X-ray detector that will be launched on an Air Force sponsored satellite called the Advanced Research and Global Observation Satellite (ARGOS). USA is a joint experiment between the Naval Research Laboratory (NRL) and the Stanford Linear Accelerator Center (SLAC).

Under the direction of Professor Elliott Bloom, SLAC has undertaken the design, fabrication and testing of the USA gimbal structure (Figure 1). This structure consists of two outer pylons that allow a yoke to pivot in the pitch axis between them. The proportional chambers are gimballed inside the yoke to allow motion in the yaw axis. In order to make an efficient design, extensive finite element modelling was used in the design process. Additionally, a process relatively new to the aerospace industry, called dip-brazing, was used to make the structure as light as possible. A prototype of the hot-side pylon was fabricated first and a static load test was performed. This test approximated the flight loads expected to be seen by the USA structure.

Static Load test Concept

The maximum static loads seen by the USA experiment are defined in USA ICD Table 1, repeated below.

	Axial (g's)	Lateral (g's)
Lift Off	+3.25/-0.26	+/- 4.00
Main Engine Cutoff	+7.1	+/- 0.13

Table 1: USA Acceleration Environment

The USA ICD also specifies that the design for any structural element that will not be subjected to a static load test use a factor of safety of 2.0 and provide positive margin in the worst case load. Any element tested to be 115% of the ICD loads need only be designed witha factor of safety of 1.5 and positive margin. All structural elements of USA were designed with a factor of safety of 2.0 and positive margin. The prototypepylon was the tested to 115% of the ICD loads. The resulting worst case stress conditions for the hot-side pylon are detailed in Table 2 and shown pictorially in Figures 2 through 5. Noting that the lift off condition has the highest peak stress, the static load test was performed for this load case only.

	Acceleration (in/s^2)			Max Stress
Load Case	a_x	a_y	a_z	Von Mises (psi)

Lift Off	-1444	-1750	309	1160
MECO	-3155	41	-41	485

Table 2: Worst Case Stress Conditions

These acceleration loads composed of two components:

1. A point load and moment at the motor/yoke interface due to the support load for the yoke/detector assembly and the acceleration load on the motor assembly.
2. A distributed load on the entire pylon due to self-loading in the acceleration environment.

Self-loading of the pylon was neglected during the static load test. the resulting point loads are given in Table 3. These loads act at the center of the pylon/motor interface ring.

		Force (lb)			Moment (in lb)		
	Node	F_x	F_y	F_z	M_x	M_y	M_z
Hub Load	13955	328	344	-183	-121	0	1830
Motor Load	00060	71	86	-15	0	0	0
Total Load	12857	399	430	-198	-274	0	1579

Table 3: Worst Case (-Y) Pylon Point Loads

Test Apparatus

The point load was applied to the test article by attaching two cables to the pylon and placing these cables in tension. Any desired force and moment combination can be generated by applying two different forces at two different locations. These loads and their points of application are given in Table 4. These are given relative to the center of the pylon/motor interface ring.

	Force (lb)			Location (in)		
	F_x	F_y	F_z	r_x	r_y	r_z
Load 1	223	0	-198	-1.53	-7.08	-1.72
Load 2	176	430	0	1.25	3.06	3.90
Total Load	399	430	-198			

Table 4: Test Case Maximum Applied Loads (at Node 12857)

Test Apparatus

The test apparatus consists of six components:

1. Test article: The prototype pylon

2. Aluminum mounting plate: 0.5" thick mounting plate to interface between the pylon and the workbench top.

3. Cable/motor interface assembly: Machined at SLAC and providing an interface for two separate loads to be applied simultaneously to the assembly.

4. Load cell: Two load cells borrowed from NASA/Ames Research Center. Each cell outputs a voltage proportional to the load acting along the sensitive axis of the cell. the voltage was recorded with a digital multimeter (DMM).

5. Turnbuckle assembly: Two assemblies purched from West Marine with working loads of 2000 lb.

6. Dial indicator: Five dial indicators will be arranged to measure the deflections of the motor/yoke interface.

The pylon was bolted to the aluminum plate which was bolted to a workbench top. The static load was applied by attaching the cable/motor interface assembly to the pylon with the cable assemblies arranged to apply two forces at two non-coincident points on the motor interface. A turnbuckle was placed on each cable to apply a desired load in the direction of the cable. A load cell on each cable measured the actual force applied. This is described pictorially in Figure 6.

Six dial indicators were used to measure the deflection of the pylon head relative to the aluminum mounting plate. These were arranged so that the three rotations and three deflections that describe the motion of the pylon head could be determined. Additionally, one dial indicator (#7) was used to measure the deflection of the baseplate relative to the workbench. The locations of the dial indicators are summarized in Table 5 and shown pictorially in Figure 7.

Measurement #	Measurement Direction	Location (in)		
		X	Y	Z
1	x	-3.65	0.05	4.57
2	x	-3.65	0.01	-4.38
3	-z	-1.98	-0.80	-4.93
4	y	-3.11	0.31	0.69
5	y	3.04	0.31	-1.97
6	y	2.60	0.31	1.96
7	y	21.13	17.75	-12.00

Table 5: Measurement Locations

Test Results

The static load test of the prototype pylon was performed in five separate cycles. Each cyle involved increasing the test load from 0% to 100% of the peak load (as given in Table 4) in increments of 10%. After reaching 100%, the test loads were decreased in decrements of 10% back to zero load. Each load was achieved as follows:

1. Tighten turnbuckles while reading the voltage output of each load cell through the DMM.
2. Read and record the measurments of each dial indicator as well as the voltage of each load cell.

The test loads and their corresponding load cell output voltages are summarized in Table 6. The measured deflections are attached. Note that five load cycles, each increments to 100% of the test load and the decremented to zeo load, did not result in any brittle fracture of the dip brazed joints or plastic deformation of the aluminum plates.

Analysis of Deflections

A finite element of the prototype pylon in the test configuration was analyzed with the IDEAS software package. The resulting stress distribution is shown in Figure 8 while the expected deflection is shown in Figure 9. Table 7 describes the expected deflections of the pylon head.

Component	Predicted Deflection (in)
ΔX	0.014
ΔY	0.049
ΔZ	-0.002

Component	Predicted Deflection (mrad)
$\Delta\Theta_x$	-0.0337
$\Delta\Theta_y$	-0.0926
$\Delta\Theta_z$	-2.218

Table 7: Predicted Pylon Head Deflections

If it is assumed that the pylon head undergoes small angle rigid body rotation and rigid body deflection, the deflections predicte by the finite element model can be related easily to the six measurements. The deflection of a point P' in such a body can be releted to the deflection of another point P in that body and the rotation of the body about P as follows:

$$\begin{Bmatrix} \Delta X \\ \Delta Y \\ \Delta Z \end{Bmatrix}_{P'} = \begin{Bmatrix} \Delta X \\ \Delta Y \\ \Delta Z \end{Bmatrix}_{P} + \begin{bmatrix} 0 & z & -y \\ -z & 0 & x \\ y & -x & 0 \end{bmatrix} \begin{Bmatrix} \Delta\Theta_x \\ \Delta\Theta_y \\ \Delta\Theta_z \end{Bmatrix}$$

where
(x, y, z) = location of P' relative to P
$(\Delta\Theta_x, \Delta\Theta_y, \Delta\theta_z)$ = rotation about P
$(\Delta X, \Delta Y, \Delta Z)_{P'}$ = deflection of P'
$(\Delta X, \Delta Y, \Delta Z)_P$ = deflection of P

The six deflections (each measured at a different point on the pylon head and in a different direction) are related to the three deflections and three rotations of the pylon head measured relative to the center of the pylon/motor interface ring as follows:

$$\begin{Bmatrix} \Delta M_1 \\ \Delta M_2 \\ -\Delta M_3 \\ \Delta M_4 \\ \Delta M_5 \\ \Delta M_6 \end{Bmatrix} = \begin{bmatrix} 1 & 0 & 0 \\ 1 & 0 & 0 \\ 0 & 0 & 1 \\ 0 & 1 & 0 \\ 0 & 1 & 0 \\ 0 & 1 & 0 \end{bmatrix} \begin{Bmatrix} \Delta X \\ \Delta Y \\ \Delta Z \end{Bmatrix}_P + \begin{bmatrix} 0 & 4.57 & -0.05 \\ 0 & -4.38 & -0.01 \\ -0.80 & 1.98 & 0 \\ -0.69 & 0 & -3.11 \\ 1.97 & 0 & 3.04 \\ -1.96 & 0 & 2.60 \end{bmatrix} \begin{Bmatrix} \Delta\Theta_x \\ \Delta\Theta_y \\ \Delta\Theta_z \end{Bmatrix}_P$$

The resulting predicted deflections at the measurement locations are given in Table 8 along with the measured peak deflections, averaged over the five load cycle tests. The final or "zero load" deflections are also shown.

Measurement	Peak Deflection (0.001")		Final Deflection (0.001")		Predicted Deflection (0.001")
#	Mean	Std Dev	Mean	Std Dev	Mean
1	14	1.0	1.0	1.3	15
2	6	0.6	0.4	0.6	14
3	2	0.2	0.1	0.2	2
4	68	3.7	3.0	4.1	56
5	36	2.1	1.8	2.4	42
6	42	2.3	1.7	2.5	43
7	-11	1.4	-2.2	1.4	0

Table 8: USA Pylon Test Results

The elastic nature ofthe deflections is shown in Figures 10 through 15.

Conclusions

The prototype pylon for the USA experiment was tested to 115% of the USA ICD flight loads in a static load test. The dip brazed joints did not undergo any brittle failure. the pylon did not undergo any plastic deformation. the measure deflections matched to expected deflections to within ten percent.

Appendix C: Pointing Feasibility Study - C Procedures

C.1 Sensitivity Study

```
#include <stdio.h>
#include <math.h>
main()
{
  int i,k,n;
  double brate,srate,SNR,P,Ps;
  double b,s,dt0,dt1,dt2,P0,P1,P2;
  double err;
  double psucc();
  printf("Enter source rate\n");
  scanf("%lf",&srate);
  Ps = 0.997;
  brate = 0.00185;
  n = 1;
  srate = srate*1296 + brate;
  P1 = 0.0;
  dt1 = 0.0;
  dt2 = 0.5;
  b = brate*dt2;
  s = srate*dt2;
  P2 = psucc(b,s,n);
  while (P2<Ps)
  {
```

```
    dt2 = dt2*2;
    b = brate*dt2;
    s = srate*dt2;
    P2 = psucc(b,s,n);
  }
  P0 = 0;
  err = fabs(P0-Ps);
  while(err>.0001)
  {
    dt0 = dt1 + (dt2-dt1)*(Ps-P1)/(P2-P1);
    b = brate*dt0;
    s = srate*dt0;
    P0 = psucc(b,s,n);
    if (P0 > Ps)
    {
      dt2 = dt0;
      P2 = P0;
    }
    else
    {
      dt1 = dt0;
      P1 = P0;
    }
    err = fabs(P0-Ps);
  }
  printf("SNR,dt,err,P = %lf %lf %lf %lf\n",SNR,dt0,err,P0);
}
```

```
#include <stdio.h>
#include <math.h>
double psucc(mub,mus,n)
double mub;
double mus;
int n;
{
  int i,k;
  double P,temp,dp,dpo;
  double term();
  P=0.0;
  k = 1;
  dpo = -1.0;
  dp = 1.0;
  while(dp>dpo)
  {
    temp = 0.0;
    for(i=0;i<k;i++)
      temp=temp + exp(-mub)*term(mub,i);
    dpo = dp;
    if(k==1) dpo = -1.0;
    dp = exp(-mus)*pow(temp,n)*term(mus,k);
    k = k+1;
    P = P + dp;
  }
```

```
  while(dp>.0001)
  {
    temp = 0.0;
    for(i=0;i<k;i++)
      temp = temp + exp(-mub)*term(mub,i);
    dp = exp(-mus)*pow(temp,n)*term(mus,k);
    k = k+1;
    P = P + dp;
  }
  return(P);
}
```

```
#include <math.h>
double term(x,n)
double x;
int n;
{
 double y;
 int i;
 y = 1.0;
 for(i=1;i<=n;i++)
  y = y*x/i;
 return(y);
}
```

C.2 X-ray Sky Survey

```
#include <stdio.h>
#include "xrstruct.h"
#include <math.h>
main()
{
  struct mapstruct stars[STARMAX];
  struct vehstruct sv;
  int nstars;
  int i,nv,l,flag,ngs;
  int gslist[100];
  FILE *fp;
  FILE *ip;
  float x,y,z,xs,ys,zs;
  float lat,lon,angle,halfangle;
  float phi,theta,dph,dth;
  float mangle,mrate,brate;
  int mnum;
  float tangle,trate;
  float sensor2an();
/* Define Environment Parameters */
  nstars = readcat(stars);
/* Define Vehicle Parameters */
  sv.psi = 0.0;
  printf("Enter sensor half angle:\n");
  scanf("%f",&halfangle);
```

```
    printf("Enter dth,dph:\n");
    scanf("%f %f",&dth,&dph);
    printf("Enter Total Background/bin:\n");
    scanf("%f",&brate);
    brate = brate*sin(halfangle)/(2*PI);
  /* Set-up Output Files */
    fp = fopen("survey.out","w");
    for(phi=-180.0;phi<180.0+dph;phi=phi+dph)
      fprintf(fp,"\t%.1f",phi);
    fprintf(fp,"\n");
    ip = fopen("stars.out","w");
    ngs = 0;
  /* Conduct Survey */
   for(theta=90.0;theta>-(90+dth);theta=theta-dth)
   {
    fprintf(fp,"%.1f",theta);
    sv.theta = theta*PI/180.0;
    for(phi=-180.0;phi<180.0+dph;phi=phi+dph)
    {
      mangle = 0.0;
      mrate = 0.0;
      mnum =0;
      sv.phi = phi*PI/180.0;
      for(i=0;i<nstars;i++)
      {
        latlon2eci(stars[i].lat,stars[i].lon,&x,&y,&z);
        eci2sensor(sv.phi,sv.theta,sv.psi,x,y,z,&xs,&ys,&zs);
        angle = sensor2an(xs,ys,zs)*180/PI;
        if(angle<halfangle)
        {
          tangle = angle*PI/180;
          trate = stars[i].rate*cos(tangle);
          if(trate>mrate)
          {
            mrate = trate;
            mangle = angle;
            mnum = i;
          }
        }
      }
      mrate = -log10(mrate)-2.345;
      fprintf(fp,"\t%.4f",mrate);
      flag = 0;
      for(l=0;l<ngs;l++)
            if(gslist[l] == mnum) flag = 1;
      if(flag == 0)
      {
        gslist[ngs] = mnum;
        ngs = ngs + 1;
      }
    }
    fprintf(fp,"\n");
  }
   fclose(fp);
```

```
  for(l=0;l<ngs;l++)
    fprintf(ip,"%d\t%f\t%f\n",gslist[l],stars[gslist[l]].lat,stars[gslist[l]].lon);
  fclose(ip);
}
```

```
#include "xrstruct.h"
#include <stdio.h>
int readcat(stars)
struct mapstruct stars[STARMAX];
{
  FILE *fp;
  int i,n;
  fp = fopen("data/x-raymap.dat","r");
  fscanf(fp,"%d",&n);
  for (i=0;i<n;i++)
    {
      fscanf(fp,"%s %f %f %f %f %f",&stars[i].name,&stars[i].ra,&stars[i].dec,
                          &stars[i].lon,&stars[i].lat,&stars[i].rate);
      stars[i].lat = stars[i].lat*PI/180.0;
      stars[i].lon = stars[i].lon*PI/180.0;
    }
 fclose(fp);
 return(n);
}
```

```
#include <math.h>
#include "xrstruct.h"
void eci2sensor(phi,theta,psi,x,y,z,xs,ys,zs)
float phi,theta,psi;
float x,y,z;
float *xs,*ys,*zs;
{
  float sp,st,ss;
  float cp,ct,cs;
  sp = sin(phi);
  st = sin(theta);
  ss = sin(psi);
  cp = cos(phi);
  ct = cos(theta);
  cs = cos(psi);
  *xs = (cs*cp+sp*ss*st)*x + (cp*ss*st-sp*cs)*y - ss*ct*z;
  *ys = (ct*sp)*x + (ct*cp)*y + st*z;
  *zs = (ss*cp-sp*cs*st)*x - (cp*cs*st+ss*sp)*y + cs*ct*z;
}
```

```
#include <math.h>
#include "xrstruct.h"
void latlon2eci(lat,lon,x,y,z)
float lat,lon;
float *x, *y, *z;
{
```

```
  *x = cos(lat)*sin(lon);
  *y = cos(lat)*cos(lon);
  *z = sin(lat);
}
```

```
#include <math.h>
float sensor2an(x,y,z)
float x;
float y;
float z;
{
  float angle;
  angle = acos(y);
  return(angle);
}
```

```
#define DETMAX  300
#define CAMAX   300
#define STARMAX 900
#define DECMAX  600
#define WIDTH   6
#define LENGTH  6
#define AREA    LENGTH*WIDTH
#define PI      3.1415926
struct detstruct
{
  float xstart;
  float xstop;
  float ystart;
  float ystop;
};
struct castruct
{
  float xstart;
  float xstop;
  float ystart;
  float ystop;
};
struct mapstruct
{
  char name[11];
  float ra;
  float dec;
  float lon;
  float lat;
  float rate;
};
struct imagestruct
{
  int source;
  int back;
  int error;
```

```
    int total;
 };
 struct vehstruct
 {
    float lat;
    float lon;
    float phi;
    float theta;
    float psi;
 };
 struct envirstruct
 {
    float backrate;
    float detrate;
    float bphi;
    float btheta;
 };
struct decstruct
{
   float angle;
   float counts;
   float flux;
   float chi;
   float scale;
};
```

Appendix D: Derivation of Equations Describing Collimator Transmission

D.1 Two Dimensional Collimators

The response of a one dimensional collimator can be described in terms of a single angle, α, as:

$$T_c = \left(1 - \frac{\tan|\alpha|}{\tan(\alpha_0)}\right)\cos(\alpha) \qquad \text{(D.1.1)}$$

Physically, the term in parentheses represents the shadowing of the detector surface by the sides of the collimator. The $\cos(\alpha)$ term represents the effect of projecting the detector area into the direction of the x-ray source, further reducing the effective detector area.

A two dimensional collimator can be manufactured by placing a rectangular shroud around the detector. The response of this collimator can then be described in

terms of two angles, α and ρ, that are the angles made by projecting the direction to the x-ray source onto the xz and yz planes respectively (Figure D.1), viz.:

$$T_c = \left(1 - \frac{\tan|\alpha|}{\tan(\alpha_0)}\right)\left(1 - \frac{\tan|\rho|}{\tan(\rho_0)}\right)\cos(\gamma) \qquad \text{(D.1.2)}$$

Note that the reduction in collimator response due to shadowing is described by functions of α and ρ. The $\cos(\gamma)$ term represents the projection of the detector area on the x-ray direction and is a function of α and ρ, viz.:

$$\cos(\gamma) = \frac{1}{\sqrt{1 + \tan^2(\alpha) + \tan^2(\rho)}} \qquad \text{(D.1.3)}$$

We would like to separate the collimator transmission into the product of the transmission of two one dimensional collimators acting independently and oriented orthogonally. To this end we can write the cos(g) term as.

$$\cos(\gamma) = \cos(\alpha)\cos(\rho)\frac{1}{\sqrt{\sin^2(\rho)\cos^2(\alpha) + \cos^2(\rho)}} \qquad \text{(D.1.4)}$$

The transmission of a two dimensional rectangular collimator can then be written as (using the fact that $\cos^2\alpha+\sin^2\alpha=1$):

$$T_c(\alpha,\rho) = T_c(\alpha)T_c(\rho)\frac{1}{\sqrt{1 - \sin^2(\rho)\sin^2(\alpha)}} \cong T_c(\alpha)T_c(\rho) \qquad \text{(D.1.5)}$$

For collimators with reasonably small fields of view, the $\frac{1}{\sqrt{1 - \sin^2(\rho)\sin^2(\alpha)}}$ term is going to be very nearly one. As an example, consider the HEAO-A1 Module 3 collimator in which the largest value of α is four degrees and the largest value of ρ is one degree. In this case, the error in the computed transmission caused by assuming this term is unity is $7.4(10^{-7})$.

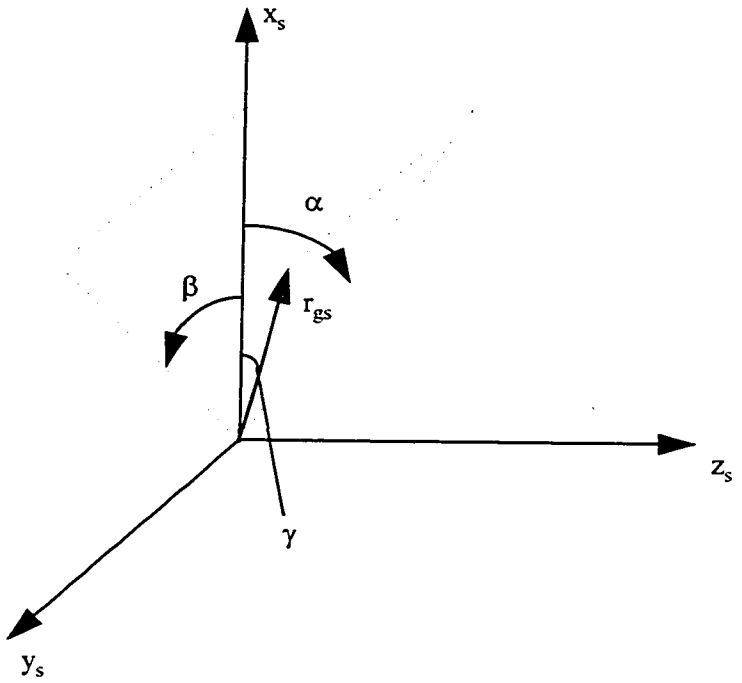

Figure D.1: Collimator Angle Definitions

Appendix E: First Order Star Scanner Model

E.1 Coordinate Systems

Celestial Coordinates - Inertially fixed frame. Denoted (X_c, Y_c, Z_c), the X_c axis points to galactic north while the Y_c axis is in the direction of the first point of Aries.

Guide Star Coordinates - Inertially fixed frame. A guide star is defined by its position in celestial coordinates. This position is given by the right ascension of the ascending node (RA) and the declination (DEC) of the star (Figure E.1). First, a rotation through RA about the X_c axis to a set of coordinates (X', Y', Z') is performed. A rotation through DEC about the Z' axis to the guide star coordinates (X, Y, Z) is then made. This places the Y axis pointing directly at the guide star. Derivation of all equations of motion will take place in the Guide Star inertial frame.

Spacecraft Coordinates - Body fixed frame. The spacecraft coordinates are in the principal directions of the inertia tensor. The z-axis is in direction of the principal axis with the maximum inertia and is in the nominal spin direction. This system is defined by the unit vectors (x,y,z).

Instrument Coordinates - Body fixed frame. The y_i-axis is in the direction of maximum instrument transmission. The x_i-axis defines the pitch axis of the instrument. The z_i-axis defines the roll axis of the instrument.

E.2 Spacecraft Orientation

The orientation of the spacecraft relative to guide star coordinates can be described by three Euler angles that represent the rotation of the spacecraft body fixed coordinate system in guide star coordinates. In this discussion these will be the yaw, pitch and roll angles (ψ,θ,ϕ) (Figure E.2).

Yaw is a rotation about the Y-axis to a coordinate system (x`, y`, z`):

$$\begin{aligned} x' &= X\cos\psi - Z\sin\psi \\ y' &= Y \\ z' &= X\sin\psi + Z\cos\psi \end{aligned} \qquad \text{(E.2.1)}$$

(E.2.1)

Pitch is a rotation about the x`-axis to a coordinate system (x``, y``, z``):

$$\begin{aligned} x'' &= x' \\ y'' &= y'\cos\theta + z'\sin\theta \\ z'' &= -y'\sin\theta + z'\cos\theta \end{aligned} \qquad \text{(E.2.2)}$$

Roll is a rotation about the z``-axis to the spacecraft coordinate system (x, y, z):

$$\begin{aligned} x &= x''\cos\phi + y''\sin\phi \\ y &= -x''\sin\phi + y''\cos\phi \\ z &= z'' \end{aligned} \qquad \text{(E.2.3)}$$

The transformation from spacecraft coordinates to guide star coordinates can be written as:

$$A_{sc2gs} = \begin{bmatrix} \cos\psi\cos\phi + \sin\psi\sin\theta\sin\phi & \cos\theta\sin\phi & -\sin\psi\cos\phi + \cos\psi\sin\theta\sin\phi \\ -\cos\psi\sin\phi + \sin\psi\sin\theta\cos\phi & \cos\theta\cos\phi & \sin\psi\sin\phi + \cos\psi\sin\theta\cos\phi \\ \sin\psi\cos\theta & -\sin\theta & \cos\psi\cos\theta \end{bmatrix} \quad \text{(E.2.4)}$$

Conversely, the transformation from guide star coordinates to spacecraft coordinates can be written as:

$$A_{gs2sc} = \begin{bmatrix} \cos\psi\cos\phi + \sin\psi\sin\theta\sin\phi & -\cos\psi\sin\phi + \sin\psi\sin\theta\cos\phi & \sin\psi\cos\theta \\ \cos\theta\sin\phi & \cos\theta\cos\phi & -\sin\theta \\ -\sin\psi\cos\phi + \cos\psi\sin\theta\sin\phi & \sin\psi\sin\phi + \cos\psi\sin\theta\cos\phi & \cos\psi\cos\theta \end{bmatrix} \quad \text{(E.2.5)}$$

E.3 Instrument Orientation

In some cases the instrument axes may not be perfectly oriented with the spacecraft axes. This may be due to the purposeful placement of the instrument or due to misalignments during manufacturing. The process of defining the instrument axes relative to the spacecraft axes in terms of euler angles is similar to that discussed in Section E.2. In this case, the euler angles are denoted (δ_x, δ_y, δ_z). In this case the rotations go (δ_z, δ_x, δ_y) (Figure E.3).

δ_z is a rotation about the z-axis to a coordinate system (x_i',y_i',z_i'):

$$\begin{aligned} x_i' &= x\cos\delta_x + y\sin\delta_x \\ y_i' &= -x\sin\delta_x + y\cos\delta_x \\ z_i' &= z \end{aligned} \quad \text{(E.3.1)}$$

δ_x is a rotation about the x_i'-axis to a coordinate system (x_i", y_i", z_i"):

$$\begin{aligned} x_i'' &= x' \\ y_i'' &= y_i' \cos\delta_x + z_i' \sin\delta_x \\ z_i'' &= -y_i' \sin\delta_x + z_i' \cos\delta_x \end{aligned} \qquad \text{(E.3.2)}$$

δ_y is a rotation about the y_i"-axis to the spacecraft coordinate system (x_i, y_i, z_i):

$$\begin{aligned} x_i &= x_i'' \cos\delta_y - z_i'' \sin\delta_y \\ y_i &= y_i'' \\ z_i &= x_i'' \sin\delta_y + z_i'' \cos\delta_y \end{aligned} \qquad \text{(E.3.3)}$$

The transformation from instrument coordinates to spacecraft coordinates can be written as:

$$A_{in2sc} = \begin{bmatrix} \cos\delta_y \cos\delta_z - \sin\delta_y \sin\delta_x \sin\delta_z & \cos\delta_y \sin\delta_z + \sin\delta_y \sin\delta_x \cos\delta_z & -\sin\delta_y \cos\delta_x \\ -\cos\delta_x \sin\delta_z & \cos\delta_x \cos\delta_z & \sin\delta_x \\ \sin\delta_y \cos\delta_z + \cos\delta_y \sin\delta_x \sin\delta_z & \sin\delta_y \sin\delta_z + \cos\delta_y \sin\delta_x \cos\delta_z & \cos\delta_y \cos\delta_x \end{bmatrix}$$

(E.3.4)

Conversely, the transformation from spacecraft coordinates to instrument coordinates can be written as:

$$A_{sc2in} = \begin{bmatrix} \cos\delta_y \cos\delta_z - \sin\delta_y \sin\delta_x \sin\delta_z & -\cos\delta_x \sin\delta_z & \sin\delta_y \cos\delta_z + \cos\delta_y \sin\delta_x \sin\delta_z \\ \cos\delta_y \sin\delta_z + \sin\delta_y \sin\delta_x \cos\delta_z & \cos\delta_x \cos\delta_z & \sin\delta_y \sin\delta_z + \cos\delta_y \sin\delta_x \cos\delta_z \\ -\sin\delta_y \cos\delta_x & \sin\delta_x & \cos\delta_y \cos\delta_x \end{bmatrix}$$

(E.3.5)

E.4 General Motion of the Spacecraft

The general motion of the spacecraft is governed by the Euler Equations:

$$\begin{aligned} T_{cx} + T_{dx} &= I_{xx}\dot{\omega}_x + (I_{zz} - I_{yy})\omega_y\omega_z \\ T_{cy} + T_{dy} &= I_{yy}\dot{\omega}_y + (I_{xx} - I_{zz})\omega_x\omega_z \\ T_{cz} + T_{dz} &= I_{zz}\dot{\omega}_z + (I_{yy} - I_{xx})\omega_y\omega_x \end{aligned} \tag{E.4.1}$$

E.4.1 Free Motion of the Spacecraft

Consider the torque free or polhode motion of the vehicle:

$$\begin{aligned} 0 &= I_{xx}\dot{\omega}_x + (I_{zz} - I_{yy})\omega_y\omega_z \\ 0 &= I_{yy}\dot{\omega}_y + (I_{xx} - I_{zz})\omega_x\omega_z \\ 0 &= I_{zz}\dot{\omega}_z + (I_{yy} - I_{xx})\omega_y\omega_x \end{aligned} \tag{E.4.2}$$

This can be linearized by assuming small perturbations about a large roll velocity:

$$\begin{aligned} \omega_x &= \omega_1 \\ \omega_y &= \omega_2 \\ \omega_z &= \Omega + \omega_3 \end{aligned} \tag{E.4.3}$$

$$\begin{aligned} 0 &= I_{xx}\dot{\omega}_1 + (I_{zz} - I_{yy})\Omega\omega_2 \\ 0 &= I_{yy}\dot{\omega}_2 + (I_{xx} - I_{zz})\Omega\omega_1 \\ 0 &= I_{zz}\dot{\omega}_3 \end{aligned} \tag{E.4.4}$$

This can be written in the LaPlace domain as:

$$\begin{bmatrix} I_{xx}s & (I_{zz} - I_{yy})\Omega & 0 \\ (I_{xx} - I_{zz})\Omega & I_{yy}s & 0 \\ 0 & 0 & I_{zz}s \end{bmatrix} \begin{Bmatrix} \omega_1 \\ \omega_2 \\ \omega_3 \end{Bmatrix} = \begin{Bmatrix} 0 \\ 0 \\ 0 \end{Bmatrix} \tag{E.4.5}$$

Note that the polhode motion of the satellite has been decoupled from the spinning motion about the z-axis. The general solution to these equations can be written as:

$$\begin{aligned}
\omega_1 &= \frac{\dot{\omega}_1(0)}{p}\sin(pt) + \omega_1(0)\cos(pt) \\
\omega_2 &= \frac{\dot{\omega}_2(0)}{p}\sin(pt) + \omega_2(0)\cos(pt) \\
\omega_3 &= \omega_3(t_0)
\end{aligned} \tag{E.4.6a}$$

where the polhode frequency, p, is:

$$p^2 = -\frac{(I_{zz} - I_{yy})(I_{xx} - I_{zz})}{I_{xx} I_{yy}}\Omega^2 \tag{E.4.6b}$$

The angular velocity of the satellite can be written in terms of the euler rates in the body axes as:

$$\begin{aligned}
\omega_x &= \dot{\psi}\cos\theta\sin\phi + \dot{\theta}\cos\phi \\
\omega_y &= \dot{\psi}\cos\theta\cos\phi - \dot{\phi}\sin\theta \\
\omega_z &= \dot{\phi} - \dot{\psi}\sin\theta
\end{aligned} \tag{E.4.7}$$

Alternately, the euler rates can be written in terms of the angular velocity:

$$\begin{aligned}
\dot{\phi} &= \omega_z + \left[\omega_x \sin\phi + \omega_y \cos\phi\right]\tan\theta \\
\dot{\theta} &= \omega_x \cos\phi - \omega_y \sin\phi \\
\dot{\psi} &= \frac{1}{\cos\theta}\left[\omega_x \sin\phi + \omega_y \cos\phi\right]
\end{aligned} \tag{E.4.8}$$

For the case of a vehicle designed to spin about its largest principal moment of inertia, the motion of the spin axis will be restricted to motion near the z-axis. That is, ψ and θ will be small. Furthermore, the roll rate can be assumed to be a perturbation about some large fixed rate, Ω. The roll angle can also be assumed to be some small perturbation about an initial roll angle, ϕ_0. The euler rate terms can then be rewritten as:

$$\begin{aligned}
\dot{\phi} &= \Omega + \omega_3 \\
\dot{\theta} &= \omega_1 \cos\phi_0 - \omega_2 \sin\phi_0 \\
\dot{\psi} &= \omega_1 \sin\phi_0 + \omega_2 \cos\phi_0
\end{aligned} \tag{E.4.9}$$

These equations can be used to related the initial conditions between the euler angles and the angular velocity in body coordinates:

$$\begin{aligned}
\omega_1(0) &= \dot{\psi}(0)\sin\phi_0 + \dot{\theta}(0)\cos\phi_0 \\
\omega_1(0) &= \dot{\psi}\,(0)\sin\phi_0 + \dot{\theta}\,(0)\cos\phi_0
\end{aligned} \tag{E.4.10a}$$

$$\begin{aligned}
\omega_2(0) &= \dot{\psi}(0)\cos\phi_0 - \dot{\theta}(0)\sin\phi_0 \\
\omega_2(0) &= \dot{\psi}\,(0)\cos\phi_0 - \dot{\theta}\,(0)\sin\phi_0
\end{aligned} \tag{E.4.10b}$$

$$\omega_3(0) = \dot{\phi}(0) - \Omega \tag{E.4.10c}$$

The differential equations for θ and ψ are first order linear differential equations that are coupled by the forcing terms ω_1 and ω_2. The roll angle, ϕ, is described by a single first order ordinary differential equation. Note that the polhode motion described by pitch and yaw is uncoupled from the rolling motion about the z-axis. The general form of their solutions will be:

$$\begin{aligned}
\theta(t) = \theta(0) + &\left(\frac{\dot{\omega}_1(0)}{p^2}\cos\phi_0 - \frac{\dot{\omega}_2(0)}{p^2}\sin\phi_0\right)(1-\cos(pt)) + \\
&\left(\frac{\omega_1(0)}{p}\cos\phi_0 - \frac{\omega_2(0)}{p}\sin\phi_0\right)\sin(pt)
\end{aligned}$$

$$\begin{aligned}
\psi(t) = \psi(0) + &\left(\frac{\dot{\omega}_1(0)}{p^2}\sin\phi_0 + \frac{\dot{\omega}_2(0)}{p^2}\cos\phi_0\right)(1-\cos(pt)) + \\
&\left(\frac{\omega_1(0)}{p}\sin\phi_0 + \frac{\omega_2(0)}{p}\cos\phi_0\right)\sin(pt)
\end{aligned} \tag{E.4.11}$$

$$\phi(t) = \phi(0) + \Omega t$$

Equations E.4.10 can be used to simplify Equation E.4.11, viz.:

$$\theta(t) = \theta(0) + \frac{\ddot{\theta}(0)}{p^2}(1 - \cos(pt)) + \frac{\dot{\theta}(0)}{p}\sin(pt)$$
$$\psi(t) = \psi(0) + \frac{\ddot{\psi}(0)}{p^2}(1 - \cos(pt)) + \frac{\dot{\psi}(0)}{p}\sin(pt) \qquad \text{(E.4.12)}$$
$$\phi(t) = \phi(0) + \Omega t$$

E.5 Guide Star Location in Instrument Frame

By the definition of the Guide Star Coordinates, the location of the guide star can be written in Guide Star Coordinates as,

$$\bar{R}_{gs} = \begin{bmatrix} 0 & 1 & 0 \end{bmatrix} \begin{Bmatrix} \hat{X} \\ \hat{Y} \\ \hat{Z} \end{Bmatrix} \qquad \text{(E.5.1)}$$

This can be transformed to the spacecraft body frame using the euler angles, viz.:

$$\bar{R}_{gs} = \begin{bmatrix} \cos(\theta)\sin(\phi) \\ \cos(\theta)\cos(\phi) \\ -\sin(\theta) \end{bmatrix}^T \begin{Bmatrix} \hat{x} \\ \hat{y} \\ \hat{z} \end{Bmatrix} \qquad \text{(E.5.2)}$$

In general, the instrument frame will not coincide exactly with the spacecraft frame. Using the transformation E.2.5 from above, the guide star location can be written in instrument coordinates as,

$$\bar{R}_{gs} = \begin{bmatrix} \cos(\theta)\sin(\phi) \\ \cos(\theta)\cos(\phi) \\ -\sin(\theta) \end{bmatrix}^T A_{sc2in} \begin{Bmatrix} \hat{x}_i \\ \hat{y}_i \\ \hat{z}_i \end{Bmatrix} \qquad \text{(E.5.3)}$$

In Appendix D, the two angles that define the transmission of the collimator were denoted α and ρ. The guide star vector can be written in terms of α and ρ, viz.:

$$\bar{R}_{gs} = \begin{bmatrix} -\dfrac{\tan(\rho)}{\sqrt{1+\tan^2(\alpha)+\tan^2(\rho)}} \\ \dfrac{1}{\sqrt{1+\tan^2(\alpha)+\tan^2(\rho)}} \\ \dfrac{\tan(\alpha)}{\sqrt{1+\tan^2(\alpha)+\tan^2(\rho)}} \end{bmatrix}^T \begin{Bmatrix} \hat{x}_i \\ \hat{y}_i \\ \hat{z}_i \end{Bmatrix} \qquad \text{(E.5.4)}$$

Equating the three terms in E.5.3 and E.5.4, we can solve for α and ρ in terms of both the known spacecraft attitude (ϕ, θ, ψ) and the orientation of the instrument in the spacecraft (δ_x, δ_y, δ_z). If this were to be done for a general case, we would have to solve this numerically. If, however, we assume that the instrument axes are close to the spacecraft axes and that the pitch and yaw euler angles are small and roll is small about some initial roll angle ϕ_0=0 (by definition of the guide star location), we can simplify the problem by making small angle approximations, viz.:

$$\begin{bmatrix} -\rho \\ 1 \\ \alpha \end{bmatrix}^T = \begin{bmatrix} \phi \\ 1 \\ -\theta \end{bmatrix}^T \begin{bmatrix} 1 & -\delta_z & \delta_y \\ \delta_z & 1 & -\delta_x \\ -\delta_y & \delta_x & 1 \end{bmatrix}$$

$$\begin{bmatrix} -\rho \\ 1 \\ \alpha \end{bmatrix}^T = \begin{bmatrix} \phi+\delta_z \\ 1 \\ -\delta_x-\theta \end{bmatrix}^T \qquad \text{(E.5.5)}$$

Or,

$$\rho = -(\phi+\delta_z)$$
$$\alpha = -(\theta+\delta_x) \qquad \text{(E.5.6)}$$

E.6 Motion of Guide Star in Instrument Frame

We can combine E.5.6 with E.4.12 to get an expression for the motion of the guide star in instrument coordinates, viz:

$$\rho = -(\phi(0) + \Omega t + \delta_z)$$

$$\alpha = -(\theta(0) + \frac{\dot{\theta}(0)}{p^2}(1 - \cos(pt)) + \frac{\ddot{\theta}(0)}{p}\sin(pt) + \delta_x) \qquad \text{(E.6.1)}$$

The initial roll angle $\phi(0)$ has been previously defined to be 0. If the polhode frequency, p, is small compared to the nominal roll rate, Ω, then pt will be second order small. Equation E.6.1 can be simplified, viz.:

$$\rho = -(\Omega t + \delta_z)$$

$$\alpha = -(\theta(0) + \delta_x) \qquad \text{(E.6.2)}$$

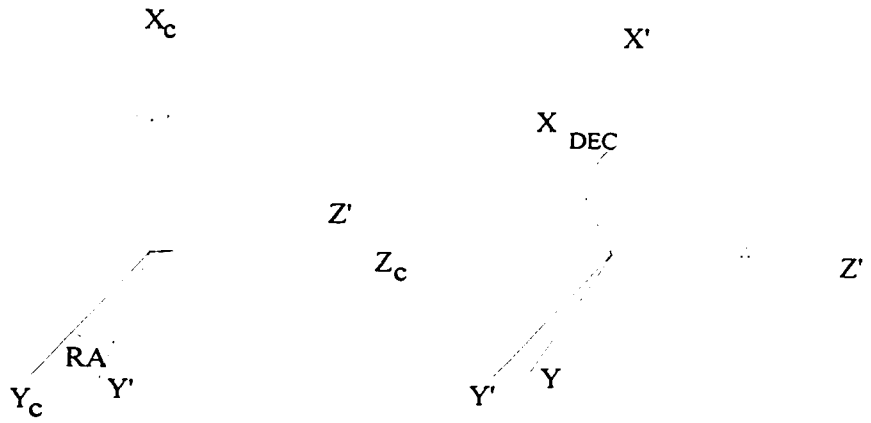

Figure E.1: Transformation from Celestial to Guide Star Coordinates

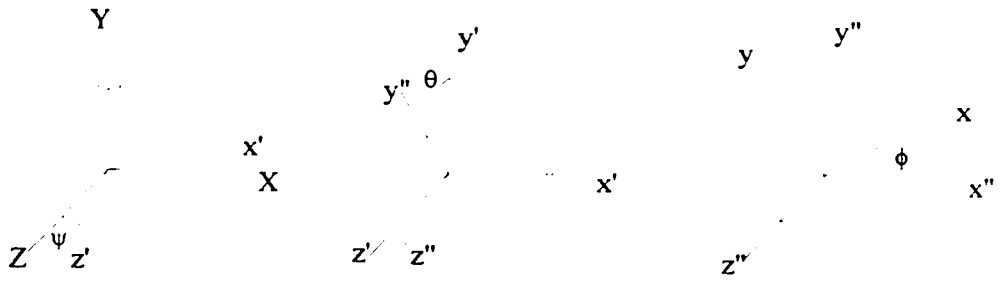

Figure E.2: Transformation from Guide Star to Spacecraft Coordinates

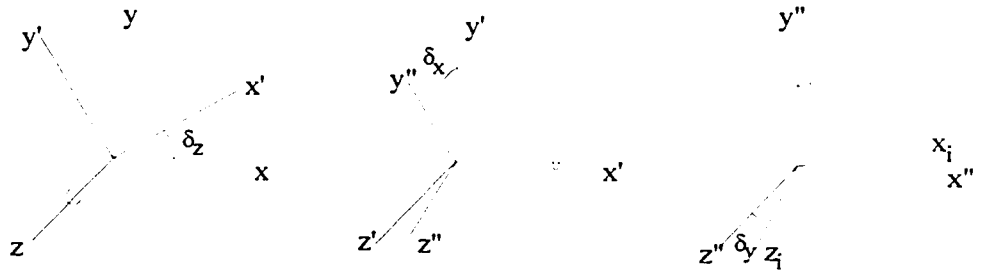

Figure E.3: Transformation from Spacecraft to Instrument Coordinates

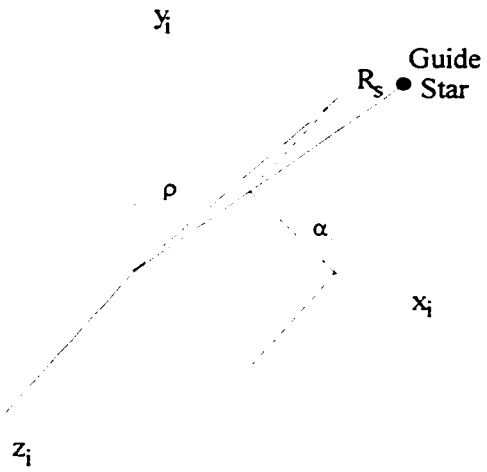

Figure E.4: Guide Star Location in Instrument Coordinates

Appendix F: Second Order Star Scanner Model

F.1 Introduction

In Appendix E it was shown that the operation of an x-ray star scanner can be described by a model that neglects any terms that are second order small and smaller. However, it may be helpful to include some of these terms. This may lead to improvements in the performance of the x-ray star scanner. In this Appendix, a second order star scanner model will be created by including the quadratic terms neglected in Appendix E. The derivation of this model will directly parallel the derivation of the first order model, using the same coordinate systems and terms.

F.2 Representation of Instrument Misalignments

The misalignment of the instrument in spacecraft coordinates can be modeled by assuming that the euler rotations that represent the instrument axes in the spacecraft frame (δ_x, δ_y, δ_z) have small errors associated with them. The actual euler rotations are

then ($\delta_x+\varepsilon_x$, $\delta_y+\varepsilon_y$, $\delta_z+\varepsilon_z$). Equation E.3.5 can be rewritten in terms of these new rotations, viz.:

$$A_{sc2in}(*,1)=\begin{bmatrix}\cos(\delta_y+\varepsilon_y)\cos(\delta_z+\varepsilon_z)-\sin(\delta_y+\varepsilon_y)\sin(\delta_x+\varepsilon_x)\sin(\delta_z+\varepsilon_z)\\ \cos(\delta_y+\varepsilon_y)\sin(\delta_z+\varepsilon_z)+\sin(\delta_y+\varepsilon_y)\sin(\delta_x+\varepsilon_x)\cos(\delta_z+\varepsilon_z)\\ -\sin(\delta_y+\varepsilon_y)\cos(\delta_x+\varepsilon_x)\end{bmatrix}$$

$$A_{sc2in}(*,2)=\begin{bmatrix}-\cos(\delta_x+\varepsilon_x)\sin(\delta_z+\varepsilon_z)\\ \cos(\delta_x+\varepsilon_x)\cos(\delta_z+\varepsilon_z)\\ \sin(\delta_x+\varepsilon_x)\end{bmatrix}$$

$$A_{sc2in}(*,3)=\begin{bmatrix}\sin(\delta_y+\varepsilon_y)\cos(\delta_z+\varepsilon_z)+\cos(\delta_y+\varepsilon_y)\sin(\delta_x+\varepsilon_y)\sin(\delta_z)\\ \sin(\delta_y+\varepsilon_y)\sin(\delta_z+\varepsilon_z)+\cos(\delta_y+\varepsilon_y)\sin(\delta_x+\varepsilon_x)\cos(\delta_z+\varepsilon_z)\\ \cos(\delta_y+\varepsilon_y)\cos(\delta_x+\varepsilon_x)\end{bmatrix}$$

(F.2.1)

Expanding the terms in F.2.1 by Taylor Series expansion yields a quadratic approximation to A_{sc2in}, viz.:

$$A_{sc2in}=\begin{bmatrix}1+\frac{(\delta_y+\varepsilon_y)^2}{2}+\frac{(\delta_z+\varepsilon_z)^2}{2} & -(\delta_z+\varepsilon_z) & (\delta_y+\varepsilon_y)+(\delta_x+\varepsilon_x)(\delta_z+\varepsilon_z)\\ (\delta_z+\varepsilon_z)+(\delta_x+\varepsilon_x)(\delta_y+\varepsilon_y) & 1+\frac{(\delta_x+\varepsilon_x)^2}{2}+\frac{(\delta_z+\varepsilon_z)^2}{2} & (\delta_x+\varepsilon_x)+(\delta_y+\varepsilon_y)(\delta_z+\varepsilon_z)\\ -(\delta_y+\varepsilon_y) & (\delta_x+\varepsilon_x) & 1+\frac{(\delta_x+\varepsilon_x)^2}{2}+\frac{(\delta_y+\varepsilon_y)^2}{2}\end{bmatrix}$$

(F.2.2)

F.3 Free Motion of the Spacecraft

The torque free motion of the vehicle can be represented by the euler equations, viz.:

$$\begin{aligned}0&=I_{xx}\dot{\omega}_x+(I_{zz}-I_{yy})\omega_y\omega_z\\ 0&=I_{yy}\dot{\omega}_y+(I_{xx}-I_{zz})\omega_x\omega_z\\ 0&=I_{zz}\dot{\omega}_z+(I_{yy}-I_{xx})\omega_y\omega_x\end{aligned}\qquad\text{(F.3.1)}$$

In this analysis, we will assume that the vehicle is nearly a body of rotation, viz.:

$$\begin{aligned} I_{xx} &= I_t \\ I_{yy} &= I_t + \delta I \\ I_{zz} &= I_a \end{aligned} \tag{F.3.2}$$

Again assuming that the vehicle is primarily spinning about the z-axis, the euler equations can be reduced to a quadratic model, viz.:

$$\begin{aligned} \omega_x &= \omega_1 \\ \omega_y &= \omega_2 \\ \omega_z &= \Omega + \omega_3 \end{aligned} \tag{F.3.3}$$

$$\begin{aligned} 0 &= I_t\dot{\omega}_1 + (I_a - I_t - \delta I)\Omega\omega_2 \\ 0 &= (I_t + \delta I)\dot{\omega}_2 + (I_t - I_a)\Omega\omega_1 \\ 0 &= I_a\dot{\omega}_3 \end{aligned} \tag{F.3.4}$$

This can be written in the LaPlace domain as:

$$\begin{bmatrix} I_t s & (I_a - I_t - \delta I)\Omega & 0 \\ (I_t - I_a)\Omega & (I_t + \delta I)s & 0 \\ 0 & 0 & I_a s \end{bmatrix} \begin{Bmatrix} \omega_1 \\ \omega_2 \\ \omega_3 \end{Bmatrix} = \begin{Bmatrix} 0 \\ 0 \\ 0 \end{Bmatrix} \tag{F.3.5}$$

Note that the polhode motion of the satellite has been decoupled from the spinning motion about the z-axis. The general solution to these equations can be written as:

$$\begin{aligned} \omega_1 &= \frac{\dot{\omega}_1(0)}{p}\sin(pt) + \omega_1(0)\cos(pt) \\ \omega_2 &= \frac{\dot{\omega}_2(0)}{p}\sin(pt) + \omega_2(0)\cos(pt) \\ \omega_3 &= 0 \end{aligned} \tag{F.3.6a}$$

where the polhode frequency, p, is:

$$p^2 = -\frac{(I_a - I_t - \delta I)(I_t - I_a)}{I_t(I_a + \delta I)}\Omega^2 \tag{F.3.6b}$$

Again, assuming that pt is small, F.3.6 can be reduced by neglecting terms smaller than second order, viz:

$$\begin{aligned}
\omega_x &= \dot{\omega}_1(0)t + \omega_1(0) \\
\omega_y &= \dot{\omega}_2(0)t + \omega_2(0) \\
\omega_z &= \Omega
\end{aligned} \tag{F.3.7}$$

From E.4.8, the euler rates can be written in terms of the angular velocity in the body axes, viz.:

$$\begin{aligned}
\dot{\phi} &= \omega_z + \left[\omega_x \sin\phi + \omega_y \cos\phi\right]\tan\theta \\
\dot{\theta} &= \omega_x \cos\phi - \omega_y \sin\phi \\
\dot{\psi} &= \frac{1}{\cos\theta}\left[\omega_x \sin\phi + \omega_y \cos\phi\right]
\end{aligned} \tag{F.3.8}$$

For the case of a vehicle designed to spin about its axis of largest principal moment of inertia, the motion of the spin axis will be restricted to motion near the z-axis. That is, ψ and θ will be small. Furthermore, the roll rate can be assumed to be a perturbation about some large fixed rate, Ω. The roll angle can also be assumed to be some small perturbation about an initial roll angle, ϕ_0. But by the definition of the guide star coordinate system, ϕ_0 is zero. Keeping the quadratic terms, the euler rate terms can then be rewritten as:

$$\begin{aligned}
\dot{\phi} &= \Omega + \omega_2\theta \\
\dot{\theta} &= \omega_1 - \omega_2\phi \\
\dot{\psi} &= \omega_2 + \omega_1\phi
\end{aligned} \tag{F.3.9}$$

Combining F.3.9 and F.3.7, we get the differential equations describing the polhode motion of the spinning vehicle to second order, viz.:

$$\begin{aligned}
\dot{\phi} - \omega_2(0)\theta &= \Omega \\
\dot{\theta} + \omega_2(0)\phi &= \dot{\omega}_1(0)t + \omega_1(0) \\
\dot{\psi} &= \omega_2 + \omega_1\phi
\end{aligned} \tag{F.3.10}$$

The general solution for these coupled equations can be written as,

$$\phi = \Omega t$$

$$\theta = \theta(0) + \dot{\theta}(0)t \qquad \text{(F.3.11)}$$

$$\psi = \psi(0) + \dot{\psi}(0)t - \Omega\theta(0)t$$

F.4 Guide Star Location in Instrument Frame

The location of the guide star can be written in spacecraft coordinates by E.4.2:

$$\bar{R}_{gs} = \begin{bmatrix} \cos(\theta)\sin(\phi) \\ \cos(\theta)\cos(\phi) \\ -\sin(\theta) \end{bmatrix}^T \begin{Bmatrix} \hat{x} \\ \hat{y} \\ \hat{z} \end{Bmatrix} \qquad \text{(F.4.1)}$$

This can be expanded by Taylor Series expansion, keeping the second order small terms, viz.:

$$\bar{R}_{gs} = \begin{bmatrix} \phi \\ 1 + \frac{\theta^2}{2} \\ 1 + \frac{\phi^2}{2} \\ -\theta \end{bmatrix}^T \begin{Bmatrix} \hat{x} \\ \hat{y} \\ \hat{z} \end{Bmatrix} \qquad \text{(F.4.2)}$$

The guide star location can be written in instrument coordinates, viz.:

$$\bar{R}_{gs} = \begin{bmatrix} \phi \\ 1 + \frac{\theta^2}{2} \\ 1 + \frac{\phi^2}{2} \\ -\theta \end{bmatrix}^T A_{sc2in} \begin{Bmatrix} \hat{x}_i \\ \hat{y}_i \\ \hat{z}_i \end{Bmatrix} \qquad \text{(F.4.3)}$$

Recalling equation E.4.5, this can also be written in terms of the collimator roll and itch angles, ρ and α, viz.:

$$\bar{R}_{gs} = \begin{bmatrix} -\dfrac{\tan(\rho)}{\sqrt{1+\tan^2(\alpha)+\tan^2(\rho)}} \\ \dfrac{1}{\sqrt{1+\tan^2(\alpha)+\tan^2(\rho)}} \\ \dfrac{\tan(\alpha)}{\sqrt{1+\tan^2(\alpha)+\tan^2(\rho)}} \end{bmatrix}^T \begin{Bmatrix} \hat{x}_i \\ \hat{y}_i \\ \hat{z}_i \end{Bmatrix} \qquad \text{(F.4.4)}$$

Substituting F.2.2 into F.4.3 and equating the result to F.4.4, we can write the collimator roll and pitch angles in terms of modelable parameters, viz:

$$\begin{aligned} \rho &= -(\phi + (\delta_x - \theta)\varepsilon_y + \delta_z + \varepsilon_z + \varepsilon_y\varepsilon_x) \\ \alpha &= -(\theta + \varepsilon_y(\phi + \varepsilon_z) + \delta_x + \varepsilon_x) \end{aligned} \qquad \text{(F.4.5)}$$

Substituting for the motion of the spacecraft as given by F.3.11 into F.4.5, we can describe the motion of the guide star in instrument coordinates, viz.:

$$\begin{aligned} \rho &= -(\Omega t + \delta_z + \varepsilon_z + (\theta(0) + \delta_x + \varepsilon_x)(\delta_y + \varepsilon_y)) \\ \alpha &= -(\theta(0) + \delta_x + \varepsilon_x) - \dot{\theta}(0)t + (\varepsilon_y + \delta_y)(\Omega t + \delta_z + \varepsilon_z) \end{aligned} \qquad \text{(F.4.6)}$$

Noting that two of the misalignment terms, ε_x and ε_z, are unobservable, the motion of the guide star can be modeled as,

$$\begin{aligned} \rho &= -(\Omega t + \delta_z + (\theta(0) + \delta_x)(\delta_y + \varepsilon_y)) \\ \alpha &= -(\theta(0) + \delta_x) - \dot{\theta}(0)t + (\varepsilon_y + \delta_y)(\Omega t + \delta_z)) \end{aligned} \qquad \text{(F.4.7)}$$

Appendix G: HEAO A1 Studies - IDL Procedures

G.1 General Files

```
function ASP2INST, Yr,Zr,Rr
; Convert from RA/DEC to Vectors
Y = transpose(rd2v(Yr(0),Yr(1)))
Z = transpose(rd2v(Zr(0),Zr(1)))
R = transpose(rd2v(Rr(0),Rr(1)))
 x = vecx(y,z)
L = dblarr(3,3)
L(0,*) = x
L(1,*) = y
L(2,*) = z
rsi = transpose(r)#transpose(L)
alpha = asin(rsi(2))
beta = atan(rsi(0),-rsi(1))
ran = [beta,alpha]
 return, ran
 end
```

```
FUNCTION RD2V, RA,DEC
 N=n_elements(RA)
r = dblarr(N,3)
 r(*,0) = cos(DEC)*cos(RA)
r(*,1) = cos(DEC)*sin(RA)
r(*,2) = sin(DEC)
 return, r
 end
```

```
function XMSSON, A,R,D_X,D_Z,F_X,F_Z
N_a = n_elements(A)
N_r = n_elements(R)
X = dblarr(N_r,N_a)
for i=0,N_r-1 do $
 for j=0,N_a-1 do begin
; Determine Roll & Pitch in Instrument Coords
   Ai = abs(A(j) - D_X)        ; Collimator Response is Symmetric
   Ri = abs(R(i) - D_Z)
; If Source is not in FOV, XMSSON = 0
   if (Ai gt F_X) or (Ri gt F_Z) then $
    X(i,j) = 0.d0  $
   else begin
; Source in FOV
    Xa = cos(Ai)*(1.d0 - tan(Ai)/tan(F_X))    ; Pitch Transmission
    Xr = cos(Ri)*(1.d0 - tan(Ri)/tan(F_Z))    ; Roll Transmission
    X(i,j) = Xa*Xr
   endelse
 end
return, X
end
```

```
FUNCTION VECX, R1,R2
r = dblarr(3)
r(0) = R1(1)*R2(2) - R2(1)*R1(2)
r(1) = R2(0)*R1(2) - R1(0)*R2(2)
r(2) = R1(0)*R2(1) - R2(0)*R1(1)
return, r
end
```

```
FUNCTION VECDOT, R1,R2
r = R1(0,*)*R2(0,*) + R1(1,*)*R2(1,*) + R1(2,*)*R2(2,*)
return, r
end
```

G.2 Single Detector Single Collimator - First Order Model

```
function ATT_MASTER, Sdata,SrcInt,Max_MJF,Max_Scan,Mode,Fdata,Nf
 COMMON Collcom, Coll1, Dt, R
; Read Data Files and Define Structures
N_Scan = Read_Data(Max_MJF,Max_Scan,Mode,'crab.idl',Sdata)
; Correct Data for Dead Time Effects
Td = .014        ; Dead Time is 14 microseconds
Sdata.cts = Sdata.cts/(1. - Sdata.cts*Td/320.)
Sdata.SrcInt = SrcInt
R = SrcInt
; Fill Collimator Properties
Coll1 = Collstr(4.*!dtor,1*!dtor)
Coll1.e_x = 0.0*!dtor
Coll1.e_z = 0.0
Coll1.Area = 1650
Coll1.Gain = 1.0
Dt = 0.320
```

```
  ; Loop Through Number of Scans
  for i = 0,N_Scan-1 do begin
    print, 'i= ',i
    plot, Sdata(i).cts
  ; Compute Spacecraft Attitude from Single Frame
    Bsv = findgen(Sdata(i).N_bin) + 1.d0
    attdet, Bsv,Sdata_i
  print,'Attitude Determined'
  ; Compute Actual Source Location in Instrument Coords
  if (Sdata(i).Fit_Err ne 1) then begin
    Bb = floor(Sdata(i).Bmax)
  print,'Bb = ',Bb
    Y_Asp = Sdata(i).Y_asp(*,Bb) + (Sdata(i).Bmax - Bb)* $
         (Sdata(i).Y_Asp(*,Bb+1)-Sdata(i).Y_Asp(*,Bb))
    Z_Asp = Sdata(i).Z_asp(*,Bb) + (Sdata(i).Bmax - Bb)* $
         (Sdata(i).Z_Asp(*,Bb+1)-Sdata(i).Z_Asp(*,Bb))
    Rr = [Sdata(i).SrcRA,Sdata(i).SrcDEC]
    Sdata(i).S_Asp(0:1) = asp2inst(Y_asp,Z_Asp,Rr)
    print,'Source Located'
    ; Compute Error in Roll Estimate
    B = SData(i).Bmax + Sdata(i).Spfit(2)
    Bf = floor(B)
    Rtmp = Sdata(i).Y_Asp(0,Bf) + (B-Bf)* $
      (Sdata(i).Y_Asp(0,Bf+1) - Sdata(i).Y_Asp(0,Bf))
    Sdata(i).R_Sig = abs(Sdata(i).S_Asp(0) - Rtmp)
    Sdata(i).A_Sig = Sdata(i).Spfit(4)
    ; Compute Spin Rate
    y1 = rd2v(Sdata(i).Y_Asp(0,Bf),Sdata(i).Y_Asp(1,Bf))
    y2 = rd2v(Sdata(i).Y_Asp(0,Bf+1),Sdata(i).Y_Asp(1,Bf+1))
    dth = acos(vecdot(transpose(y1),transpose(y2)))
    Sdata(i).S_Asp(2) = abs(dth/dt)
  endif
  end
  ; Compute Error in Attitude Solution
  Sdata.S_err(0) = Sdata.S_Asp(0) - Sdata.S_Est(0)
  Sdata.S_err(1) = abs(Sdata.S_Asp(1)) - Sdata.S_Est(1)
  Sdata.S_err(2) = Sdata.S_Asp(2) - Sdata.S_Est(2)
  print,'Error Computed'
  ; Filter out Fit Errors
  Fdata = Sdata
  Nf = 0
  for i=0,N_Scan-1 do $
    if (Sdata(i).Fit_Err eq 0) then begin
      Fdata(Nf) = Sdata(i)
      Nf = Nf + 1
    endif
  return, N_Scan
  end
```

```
pro ATTDET, Bsv,Data,ii
; Set Initial Parameters for Search
  ; Set Peak at Max Counts
Tn = Data(ii).N_bin
Tcts = Data(ii).Cts(1:Tn-2) + Data(ii).Cts(0:Tn-3) + Data(ii).Cts(2:Tn-1)
```

```
 Tmax = max(Tcts,Tbin)
 Mbin = Tbin + 1
 Cmax = Data(ii).Cts(Mbin)
 Alpha = 0.0              ; Start at zero angle
 Rho = Mbin               ; And peak source location
   ; Set Background to Average Count Rate
 B0 = Median(Data(ii).Cts(0:Data(ii).N_bin))
 Bf = B0
 Ws = 0.00272
 Pfit = [B0,Bf,Rho,Ws,Alpha]
 ; Fit Triangular Collimator Response Function
 N_free = float(Data(ii).N_bin - n_elements(Data(ii).Pfit))
 counts = Data(ii).Cts(0:Data(ii).N_Bin-1)
 Data(ii).Rchi = collfit(Bsv,Counts,Pfit,Yfit,Fit_Err,SPfit)/N_free
 Data(ii).Fit_Err = Fit_err
 Data(ii).Pfit = Pfit
 Data(ii).Yfit = Yfit
 Data(ii).Spfit = Spfit
 ; Determine Source Location in Instrument Coordinates
 Data(ii).Alpha = Pfit(4)
 Data(ii).Bmax = Pfit(2)
 if ((Data(ii).Bmax gt Data(ii).N_bin-1) or S
   (Data(ii).Bmax lt 0)) Then Data(ii).Fit_Err = 1
 ; Compute Source Location in Instrument Coordinates
  Data(ii).S_Est = [0.d0,Data(ii).Alpha,Pfit(3)]
  end
```

```
FUNCTION COLLFIT, X,Y,P,Yfit,E_Flag,SigP
 Npoints = n_elements(X)
Npar = n_elements(P)
 W = sqrt(1./Y)
Yfit = crv_fit(X,Y,W,P,E_FLAG,SigP,FUNCTION_NAME='collder')
 E = total(((Yfit-Y)^2)/Y)
 return, E
end
```

```
PRO COLLDER, X,P,F,PDER
 Npoints = n_elements(X)
Npar = n_elements(P)
PDER = dblarr(Npoints,Npar)
 B0 = P(0)
Bf = P(1)
Rho = P(2)
Ws = P(3)
Alpha = P(4)
E = collerr(X,F,B0,Bf,Rho,Ws,Alpha)
; Compute Derivatives Numerically
;   dF/dB0
eta = 1.001;
E = collerr(X,Fp,eta*B0,Bf,Rho,Ws,Alpha)
PDER(*,0) = (Fp-F)/((eta-1.0)*B0)
; Compute Derivatives Numerically
;   dF/dB0
eta = 1.001;
```

```
E = collerr(X,Fp,B0,eta*Bf,Rho,Ws,Alpha)
PDER(*,1) = (Fp-F)/((eta-1.0)*Bf)
;   dF/dRho
eta = 1.001
E = collerr(X,Fp,B0,Bf,eta*Rho,Ws,Alpha)
PDER(*,2) = (Fp-F)/((eta-1.0)*Rho)
;   dF/dWs
eta = 1.001
E = collerr(X,Fp,B0,Bf,Rho,eta*Ws,Alpha)
PDER(*,3) = (Fp-F)/((eta-1.0)*Ws)
;   dF/dAlpha
eta = 1.001
dAlpha = (eta - 1.0)*Alpha
if (dAlpha eq 0.0) then dAlpha = 0.001*!dtor
E = collerr(X,Fp,B0,Bf,Rho,Ws,Alpha+dAlpha)
PDER(*,4) = (Fp-F)/dAlpha
end
```

```
function COLLERR, Cts,Trn,B0,Bf,Rho,Ws,Alpha
 COMMON Collcom, Coll1, Dt, R     ; R = Source Intensity
N = n_elements(Cts)
Trn = dblarr(N)
Cresp = dblarr(N)
; Transform to managable paramters
theta = findgen(N)*Ws*Dt - Rho*Ws*Dt
; Determine Background Level
Back = findgen(N)*(Bf-B0)/N + B0
: Get Fitted Collimator Response
  Cresp = xmsson(Alpha,Theta,0.0,0.0,Coll1.xFOV,Coll1.zFOV)
 Trn = R*Cresp + Back
E = Trn - Cts
return, E
end
```

```
:              R        Attitude Determination Structure
:  ======================Att_Struct=========================
:  N_Mjf     :  Number of Major Frames, integer
:  N_Bin     :  Number of Bins in Scan, integer
:  Mjf       :  Array of Major Frame Numbers, lonarr(n_mjf)
;  Mode      :  Timing Mode of HEAO (320,5)
;  Module    :  Module Number (3,4,5,6,7)
;  SrcRA     :  Source RA (rad)
;  SrcDEC    :  Source DEC (rad)
;  SrcName   :  Source Name (string)
;  SrcInt    :  Source Mean Intensity in This Mode (double)
;  Cts       :  Array of Counts for Current Scan (intarr(n_bin))
;  Trn       :  Transmission Function from Aspect Solution
;  Y_Asp     :  Orientation of Y-axis (RA,DEC) for each bin
;  Z_Asp     :  Orientation of Z-axis (RA,DEC) for each bin
;  S_Asp     :  Location of the Source in Instrument Coordinates
;               (RA,DEC)
;  Y_Est     :  Estimated orientation of Y-axis (RA,DEC) for Peak Bin
;  Z_Est     :  Estimated orientation of Z-axis (RA,DEC) for Peak Bin
;  S_Est     :  Estimated Location off the Source in Instrument
```

```
;                Coordinates (RA,DEC)
;  Bmax      :  Bin Where Attitude Estimate Occurs
;  Yfit      :  Fit to Scan (double(N_Bin))
;  Alpha     :  Estimated Source Angle Off Vertical
;  Fit_Err   :  Flag Indicatinf Error in Fitting Process (1=error)
;  Rchi      :  Reduced Chi-Squared in Fit
;  Pfit      :  Fit Parameters (double(5))
;  Y_Err     :  Error in Estimate of Y-axis (RA,DEC) for Peak Bin
;  Z_Err     :  Error in Estimate of Z-axis (RA,DEC) for Peak Bin
;  S_Err     :  Error in Estimate of Source Location (RA,DEC)
```

G.3 Dual Detector Dual Collimator - First Order Model

```
function A35_INPUT, Max_MJF,Max_Scan,Mode,V3Data,V5Data
; Read Data Files and Define Structures
print,'Mod 3 Data'
N_Scan3 = Read_Data(Max_MJF,Max_Scan,Mode,pickfile(),S3data)
print,'Mod 5 Data'
N_Scan5 = Read_Data(Max_MJF,Max_Scan,Mode,pickfile(),S5data)
; Strip Out Appropriate Mod 5 Scans
V5data = replicate(S5Data(Max_Scan-1),7)
V3data = replicate(S3Data(Max_Scan-1),7)
Sel5 = [31,36,38,39,40,43,44]
Sel3 = intarr(7)
for i=0,n_elements(Sel5)-1 do begin
  V5data(i) = S5data(Sel5(i))
  ; Find Corresponding Mod3 Data
  Mjnum = V5data(i).Mjf
  for jj=0,N_Scan3-1 do $
    for kk=0,S3data(jj).N_Mjf-1 do $
      if (S3data(jj).Mjf(kk) eq Mjnum(0)) then begin
        V3data(i) = S3data(jj)
        Sel3(i) = jj
      endif
endfor
print,'Sel5 = ',Sel5
print,'Sel3 = ',Sel3
; Correct for Dead Time Effects
Td = 14.e-6
V3data.cts = V3data.cts/(1. - V3data.cts*Td/0.32)
V5data.cts = V5data.cts/(1. - V5data.cts*Td/0.32)
return, N_Scan3
end
```

```
pro A35_Mast, X3data,X5data,N
 COMMON COLLCOM, Coll1,Coll2,Dt
; Define Collimator Structures
; Collimator 1 - Mod 3
Coll1 = Collstr(8.*!dtor,2.*!dtor)
Coll1.e_x = 0.0*!dtor
Coll1.e_z = 0.0
Coll1.area = 1650.
Coll1.gain = 1.0
```

```
; Collimator 2 - Mod 5
coll2 = coll1
coll2.xFOV = 1.*!dtor
coll2.zFOV = 2.*!dtor
Coll2.e_x = 0.3333*!dtor
Coll2.e_z = 0.0
Coll2.Area = 1350.
Coll2.Gain = 1.
; Define Satellite Properties - HEAO
dt = 0.320   ; Timing: 320 ms Mode
ws = .00272  ; Spin Rate
; Call COLLSIM
C35sim, X3data,X5data,N,Ws
end
```

```
pro C35SIM, X3data,X5data,N_Scan,Ws
COMMON COLLCOM, Coll1,Coll2,Dt
; Loop Through Number of Scans
for i = 0,N_Scan-1 do begin
print, 'i = ',i
; Compute Spacecraft Attitude from Single Frame
  Bsv = findgen(X3data(i).N_bin)
print, 'Collsim, Bsv = ',Bsv(0),Bsv(X3data(i).N_bin-1)
  !p.multi = [0,1,2]
; plot, X3data(i).cts,psym=10
; plot, X5data(i).cts,psym=10
  attdet, Bsv,X3data,X5data,i,Ws
; Compute Actual Source Location in Instrument Coords
  Bb = floor(X3Data(i).Bmax)
  Y_Asp = X3data(i).Y_asp(*,Bb) + (X3data(i).Bmax - Bb)* S
      (X3data(i).Y_Asp(*,Bb+1)-X3data(i).Y_Asp(*,Bb))
  Z_Asp = X3data(i).Z_asp(*,Bb) + (X3data(i).Bmax - Bb)* S
      (X3data(i).Z_Asp(*,Bb+1)-X3data(i).Z_Asp(*,Bb))
  Rr = [X3data(i).SrcRA,X3data(i).SrcDEC]
  X3data(i).S_Asp(0:1) = asp2inst(Y_asp,Z_Asp,Rr)
  print,'Source Located'
  B = X3data(i).Bmax+X3data(i).Spfit(4)
  Bf = floor(B)
  print, 'Stats ',B,Bf
  Rtmp = X3data(i).Y_asp(0,Bf) + (B - Bf)* S
      (X3data(i).Y_Asp(0,Bf+1) - X3data(i).Y_Asp(0,Bf))
  X3data(i).R_Sig = abs(X3data(i).S_Asp(0) - Rtmp)
  X3data(i).A_Sig = X3data(i).Spfit(6)
  ; Compute Spin Rate
  y1 = rd2v(X3data(i).Y_Asp(0,Bf),X3data(i).Y_Asp(1,Bf))
  y2 = rd2v(X3data(i).Y_Asp(0,Bf+1),X3data(i).Y_Asp(1,Bf+1))
print,'y1 = ',y1
print,'y2 = ',y2
  dth = acos(vecdot(transpose(y1),transpose(y2)))
  X3data(i).S_Asp(2) = abs(dth/dt)
print,'dth,dt = ',dth,dt
  X3data(i).S_Est(2) = X3data(i).Pfit(5)
end
; Compute Error in Attitude Solution
```

```
X3data.S_err = X3data.S_Asp - X3data.S_Est
print,'Error Computed'
end
```

```
pro ATTDET, Bsv,X3Data,X5data,ii,Ws
COMMON Collcom, Coll1,Coll2,Dt
; Collimator 1
; Set Initial Parameters for Search
  ; Set Peak at Max Counts
Tn = X3Data(ii).N_bin
Tcts1 = X3Data(ii).Cts(1:Tn-2) + X3Data(ii).Cts(0:Tn-3) + X3Data(ii).Cts(2:Tn-1)
Tmax1 = max(Tcts1,Tbin1)
Tcts2 = X5Data(ii).Cts(1:Tn-2) + X5Data(ii).Cts(0:Tn-3) + X5Data(ii).Cts(2:Tn-1)
Tmax2 = max(Tcts1,Tbin2)
if (Tmax1 gt Tmax2) then $
  Mbin = Tbin1 + 1 $
else Mbin = Tbin2 + 1
Cmax1 = X3Data(ii).Cts(Mbin)
Cmax2 = X5Data(ii).Cts(Mbin)
Alpha = 0.0                ; Set Pitch Angle Guess
Rho = Mbin                 ; Set Roll Angle Guess
  ; Set Background to Average Count Rate
B01 = X3Data(ii).Cts(0)
B02 = X5Data(ii).Cts(0)
Bf1 = X3data(ii).Cts(X3data(ii).N_Bin-1)
Bf2 = X5data(ii).Cts(X5data(ii).N_Bin-1)
Ba1 = (B01+Bf1)/2.
Ba2 = (B02+Bf2)/2.
R = max([(Cmax1-Ba1)/Coll1.Area,(Cmax2-Ba2)/Coll2.Area]) ; Set Source Strength
Pfit = [B01,Bf1,B02,Bf2,Rho,Ws,Alpha,R]
print, 'Attdet, P = ',Pfit
; Fit Triangular Collimator Response Function
N_free = float(2*X3Data(ii).N_bin - n_elements(X3Data(ii).Pfit))
Counts1 = X3Data(ii).Cts(0:X3Data(ii).N_Bin-1)
Counts2 = X5Data(ii).Cts(0:X5Data(ii).N_Bin-1)
X3Data(ii).Rchi = s2fit(Bsv,Counts1,Counts2,Pfit,Yfit1,Yfit2, $
            Fit_Err,SPfit)/N_free
X3Data(ii).Fit_Err = Fit_err
X3Data(ii).Pfit = Pfit
X3Data(ii).Yfit = Yfit1
X5Data(ii).Yfit = Yfit2
X3Data(ii).Spfit = Spfit
; Determine Backgrounds & Ratios
X3Data(ii).Bmax = Pfit(4)
X3Data(ii).Back = Pfit(0) + (Pfit(1) - Pfit(0))*X3Data(ii).Bmax/X3Data(ii).N_Bin
X5Data(ii).Back = (Pfit(2) + (Pfit(3) - Pfit(2)) $
          *X3Data(ii).Bmax/X5Data(ii).N_Bin)
; Compute Source Location in Instrument Coordinates
X3Data(ii).Alpha = Pfit(6)
X3Data(ii).S_Est = [0.d0,X3Data(ii).Alpha]
; Try Other Side of Collimator - Store in X5Data
Alpha = Coll2.e_x + .2*!dtor
pfit = [B01,Bf1,B02,Bf2,Rho,Ws,Alpha,R]
print, 'Attdet2, P2 = ',Pfit
```

```
; Fit Triangular Collimator Response Function
X5Data(ii).Rchi = s2fit(Bsv,Counts1,Counts2,Pfit,Yfit1,Yfit2, S
          Fit_Err,SPfit)/N_free
X5Data(ii).Fit_Err = Fit_err
X5Data(ii).Pfit = Pfit
X5Data(ii).Yfit = Yfit2
X5Data(ii).Spfit = Spfit
X5Data(ii).Bmax = Pfit(4)
X5Data(ii).Back = Pfit(0) + (Pfit(1) - Pfit(0))*X5Data(ii).Bmax/X5Data(ii).N_Bin
X5Data(ii).Back = (Pfit(2) + (Pfit(3) - Pfit(2)) $
          *X3Data(ii).Bmax/X5Data(ii).N_Bin)
; Compute Source Location in Instrument Coordinates
X5Data(ii).Alpha = Pfit(6)
X5Data(ii).S_Est = [0.d0,X5Data(ii).Alpha]
end
```

```
FUNCTION S2FIT, X,Y1,Y2,P,Yfit1,Yfit2,E_Flag,SigP
Npoints = n_elements(X)
Npar = n_elements(P)
Yt = [Y1,Y2]
Xt = [X,X+Npoints]
W = sqrt(Yt)
Yfit = crv_fit(Xt,Yt,W,P,E_FLAG,SigP,FUNCTION_NAME='s2der')
Yfit1 = Yfit(0:Npoints-1)
Yfit2 = Yfit(Npoints:2*Npoints-1)
E = total(((Yfit-Yt)^2)/Yt)
return, E
end
```

```
PRO S2DER, X,P,F,PDER
Npoints = n_elements(X)
Npar = n_elements(P)
PDER = dblarr(Npoints,Npar)
print, 'P = ',P
B01 = P(0)
Bf1 = P(1)
B02 = P(2)
Bf2 = P(3)
Rho = P(4)
Ws = P(5)
Alpha = P(6)
R = P(7)
Tc = findgen(Npoints) + 1.
E = s2err(X,Tc,F,B01,Bf1,B02,Bf2,Rho,Ws,Alpha,R)
; Compute Derivatives Numerically
;   dF/dB01
eta = 1.01;
E = s2err(X,Tc,Fp,eta*B01,Bf1,B02,Bf2,Rho,Ws,Alpha,R)
PDER(*,0) = (Fp-F)/((eta-1.0)*B01)
; Compute Derivatives Numerically
;   dF/dBf1
eta = 1.01;
E = s2err(X,Tc,Fp,B01,eta*Bf1,B02,Bf2,Rho,Ws,Alpha,R)
PDER(*,1) = (Fp-F)/((eta-1.0)*Bf1)
```

```
;   dF/dB02
eta = 1.01;
E = s2err(X,Tc,Fp,B01,Bf1,eta*B02,Bf2,Rho,Ws,Alpha,R)
PDER(*,2) = (Fp-F)/((eta-1.0)*B02)
; Compute Derivatives Numerically
;   dF/dBf1
eta = 1.01;
E = s2err(X,Tc,Fp,B01,Bf1,B02,eta*Bf2,Rho,Ws,Alpha,R)
PDER(*,3) = (Fp-F)/((eta-1.0)*Bf2)
;   dF/dRho
dRho = 1.0
E = s2err(X,Tc,Fp,B01,Bf1,B02,Bf2,Rho+dRho,Ws,Alpha,R)
PDER(*,4) = (Fp-F)/double(dRho)
;   dF/dWs
eta = 1.01
E = s2err(X,Tc,Fp,B01,Bf1,B02,Bf2,Rho,eta*Ws,Alpha,R)
PDER(*,5) = (Fp-F)/((eta-1.0)*Ws)
;   dF/dAlpha
eta = 1.01
dAlpha = (eta - 1.0)*Alpha
if (dAlpha eq 0.0) then dAlpha = 0.01*!dtor
E = s2err(X,Tc,Fp,B01,Bf1,B02,Bf2,Rho,Ws,Alpha+dAlpha,R)
PDER(*,6) = (Fp-F)/dAlpha
;   dF/dR
eta = 1.01
E = s2err(X,Tc,Fp,B01,Bf2,B02,Bf2,Rho,Ws,Alpha,R*eta)
PDER(*,7) = (Fp-F)/((eta-1.0)*R)
end
```

```
function S2ERR, X,Cts,Trn,B01,Bf1,B02,Bf2,Rho,Ws,Alpha,R
COMMON Collcom, Coll1, Coll2, Dt
G = 1.0
Nt = n_elements(X)
N = Nt/2
Trn = dblarr(Nt)
; Transform to managable parameters
L1 = Rho - 0.5*Coll1.zFOV/(Ws*Dt)
L2 = Rho + 0.5*Coll1.zFOV/(Ws*Dt)
L3 = Rho - 0.5*Coll2.zFOV/(Ws*Dt)
L4 = Rho + 0.5*Coll2.zFOV/(Ws*Dt)
P1 = R*(1. - tan(abs(Alpha - Coll1.e_x))/tan(0.5*Coll1.xFOV))* S
     cos(abs(Alpha - Coll1.e_x))*Coll1.Area
P2 = R*(1 - tan(abs(Alpha - Coll2.e_x))/tan(0.5*Coll2.xFOV))* S
     cos(abs(Alpha - Coll2.e_x))*Coll2.Area
; Keep L1, L2 in acceptable bounds
if (L1 lt 1) then L1 = 1 S
else if (L1 gt N) then L1 = N
if (L2 lt L1) then L2 = L1 S
else if (L2 gt N) then L2 = N
if (L3 lt 1) then L3 = 1 S
else if (L3 gt N) then L3 = N
if (L4 lt L3) then L4 = L3 S
else if (L4 gt N) then L4 = N
for i=0,Nt-1 do S
```

```
    case 1 of
    (X(i) lt L1): begin   ; First Scan, To 1st Break
      Trn(i) = B01 + (Bf1-B01)*X(i)/(N-1)
             end
    (X(i) ge L1) and (X(i) lt Rho): begin   ; First Scan, 1st Side
      B = B01 + (Bf1-B01)*X(i)/(N-1)
      Trn(i) = B + 2*(X(i) - L1)*(P1)/(L2-L1)
             end
    (X(i) ge Rho) and (X(i) lt L2): begin   ; First Scan, 2nd Side
      B = B01 + (Bf1-B01)*X(i)/(N-1)
      Trn(i) = B + 2*(L2 - X(i))*(P1)/(L2-L1)
             end
    (X(i) ge L2) and (X(i) lt N): begin   ; First Scan, From 2nd Side
      B = B01 + (Bf1-B01)*X(i)/(N-1)
      Trn(i) = B
             end
    (X(i) ge N) and (X(i) lt N+L3): begin   ; 2nd Scan, To 1st Side
      Trn(i) = (B02 + (Bf2-B02)*(X(i)-N)/(N-1))
             end
    (X(i) ge N+L3) and (X(i) lt N+Rho): begin   ; 2nd Scan, 1st Side
      B = (B02 + (Bf2-B02)*(X(i)-N)/(N-1))
      Trn(i) = B + 2*(X(i) - N - L3)*(P2)/(L4-L3)
             end
    (X(i) ge N+Rho) and (X(i) lt N+L4): begin   ; 2nd Scan, 2nd Side
      B = (B02 + (Bf2-B02)*(X(i)-N)/(N-1))
      Trn(i) = B + 2*(L4 - X(i) + N)*(P2)/(L4-L3)
             end
    (X(i) ge N+L4) and (X(i) lt Nt): begin   ; 2nd Scan, End
      B = (B02 + (Bf2-B02)*(X(i)-N)/(N-1))
      Trn(i) = B
             end
    else: print, 'X has illegal value: ',i,X(i)
  endcase
  E = total(((Cts - Trn)^2)/Cts)
  return, E
  end
```

G.4 Dual Detector Dual Collimator - Second Order Model

```
pro ATTDET, Bsv,X3Data,X5data,ii,Ws
COMMON Collcom, Coll1,Coll2,Dt
;  Collimator 1
; Set Initial Parameters for Search
  ; Set Peak at Max Counts
Tn = X3Data(ii).N_bin
Tcts1 = X3Data(ii).Cts(1:Tn-2) + X3Data(ii).Cts(0:Tn-3) + X3Data(ii).Cts(2:Tn-1)
Tmax1 = max(Tcts1,Tbin1)
Tcts2 = X5Data(ii).Cts(1:Tn-2) + X5Data(ii).Cts(0:Tn-3) + X5Data(ii).Cts(2:Tn-1)
Tmax2 = max(Tcts1,Tbin2)
if (Tmax1 gt Tmax2) then S
  Mbin = Tbin1 + 1 S
else Mbin = Tbin2 + 1
Cmax1 = X3Data(ii).Cts(Mbin)
```

```
Cmax2 = X5Data(ii).Cts(Mbin)
Alpha = 0.0                ; Set Pitch Angle Guess
Rho = Mbin                 ; Set Roll Angle Guess
  ; Set Background to Average Count Rate
B01 = Median(X3Data(ii).Cts(0:X3Data(ii).N_bin-1))
B02 = Median(X5Data(ii).Cts(0:X5Data(ii).N_bin-1))
Bf1 = B01
Bf2 = B02
R = max([(Cmax1-B01)/Coll1.Area,(Cmax2-B02)/Coll2.Area]) ; Set Source Strength
E_y = 0.0
Alpha_Dot = 0.0
Pfit = [B01,Bf1,B02,Bf2,Rho,Ws,Alpha,R,E_y,Alpha_Dot]
print, 'Attdet, P = ',Pfit
; Fit Triangular Collimator Response Function
N_free = float(2*X3Data(ii).N_bin - n_elements(X3Data(ii).Pfit))
Counts1 = X3Data(ii).Cts(0:X3Data(ii).N_Bin-1)
Counts2 = X5Data(ii).Cts(0:X5Data(ii).N_Bin-1)
X3Data(ii).Rchi = s3fit(Bsv,Counts1,Counts2,Pfit,Yfit1,Yfit2, S
            Fit_Err,SPfit)/N_free
X3Data(ii).Fit_Err = Fit_err
X3Data(ii).Pfit = Pfit
X3Data(ii).Yfit = Yfit1
X5Data(ii).Yfit = Yfit2
X3Data(ii).Spfit = Spfit
; Determine Backgrounds & Ratios
X3Data(ii).Bmax = Pfit(4)
X3Data(ii).Back = Pfit(0) + (Pfit(1) - Pfit(0))*X3Data(ii).Bmax/X3Data(ii).N_Bin
X5Data(ii).Back = (Pfit(2) + (Pfit(3) - Pfit(2)) S
          *X3Data(ii).Bmax/X5Data(ii).N_Bin)
; Compute Source Location in Instrument Coordinates
X3Data(ii).Alpha = Pfit(6)
X3Data(ii).S_Est = [0.d0,X3Data(ii).Alpha]
; Try Other Side of Collimator - Store in X5Data
Alpha = Coll2.e_x + .2*!dtor
E_y = 0.0
Alpha_Dot = 0.0
pfit = [B01,Bf1,B02,Bf2,Rho,Ws,Alpha,R,E_y,Alpha_Dot]
print, 'Attdet2, P2 = ',Pfit
; Fit Triangular Collimator Response Function
X5Data(ii).Rchi = s3fit(Bsv,Counts1,Counts2,Pfit,Yfit1,Yfit2, S
            Fit_Err,SPfit)/N_free
X5Data(ii).Fit_Err = Fit_err
X5Data(ii).Pfit = Pfit
X5Data(ii).Yfit = Yfit2
X5Data(ii).Spfit = Spfit
X5Data(ii).Bmax = Pfit(4)
X5Data(ii).Back = Pfit(0) + (Pfit(1) - Pfit(0))*X5Data(ii).Bmax/X5Data(ii).N_Bin
X5Data(ii).Back = (Pfit(2) + (Pfit(3) - Pfit(2)) S
          *X3Data(ii).Bmax/X5Data(ii).N_Bin)
; Compute Source Location in Instrument Coordinates
X5Data(ii).Alpha = Pfit(6)
X5Data(ii).S_Est = [0.d0,X5Data(ii).Alpha]
end
```

```
FUNCTION S3FIT, X,Y1,Y2,P,Yfit1,Yfit2,E_Flag,SigP
Npoints = n_elements(X)
Npar = n_elements(P)
Yt = [Y1,Y2]
Xt = [X,X+Npoints]
W = sqrt(Yt)
Yfit = crv_fit(Xt,Yt,W,P,E_FLAG,SigP,FUNCTION_NAME='s3der')
Yfit1 = Yfit(0:Npoints-1)
Yfit2 = Yfit(Npoints:2*Npoints-1)
E = total(((Yfit-Yt)^2)/Yt)
return, E
end
```

```
PRO S3DER, X,P,F,PDER
Npoints = n_elements(X)
Npar = n_elements(P)
PDER = dblarr(Npoints,Npar)
;print, 'P = ',P
B01 = P(0)
Bf1 = P(1)
B02 = P(2)
Bf2 = P(3)
Rho = P(4)
Ws = P(5)
Alpha = P(6)
R = P(7)
E_y = P(8)
Alpha_Dot = P(9)
;Alpha_Dot = 0.0;
Tc = findgen(Npoints) + 1.
E = s3err(X,Tc,F,B01,Bf1,B02,Bf2,Rho,Ws,Alpha,R,E_y,Alpha_Dot)
; Compute Derivatives Numerically
;  dF/dB01
eta = 1.01;
E = s3err(X,Tc,Fp,eta*B01,Bf1,B02,Bf2,Rho,Ws,Alpha,R,E_y,Alpha_Dot)
PDER(*,0) = (Fp-F)/((eta-1.0)*B01)
; Compute Derivatives Numerically
;  dF/dBf1
eta = 1.01;
E = s3err(X,Tc,Fp,B01,eta*Bf1,B02,Bf2,Rho,Ws,Alpha,R,E_y,Alpha_Dot)
PDER(*,1) = (Fp-F)/((eta-1.0)*Bf1)
;  dF/dB02
eta = 1.01;
E = s3err(X,Tc,Fp,B01,Bf1,eta*B02,Bf2,Rho,Ws,Alpha,R,E_y,Alpha_Dot)
PDER(*,2) = (Fp-F)/((eta-1.0)*B02)
; Compute Derivatives Numerically
;  dF/dBf1
eta = 1.01;
E = s3err(X,Tc,Fp,B01,Bf1,B02,eta*Bf2,Rho,Ws,Alpha,R,E_y,Alpha_Dot)
PDER(*,3) = (Fp-F)/((eta-1.0)*Bf2)
;  dF/dRho
dRho = 1.0
E = s3err(X,Tc,Fp,B01,Bf1,B02,Bf2,Rho+dRho,Ws,Alpha,R,E_y,Alpha_Dot)
PDER(*,4) = (Fp-F)/double(dRho)
```

```
;   dF/dWs
eta = 1.01
E = s3err(X,Tc,Fp,B01,Bf1,B02,Bf2,Rho,eta*Ws,Alpha,R,E_y,Alpha_Dot)
PDER(*,5) = (Fp-F)/((eta-1.0)*Ws)
;   dF/dAlpha
eta = 1.01
dAlpha = (eta - 1.0)*Alpha
if (dAlpha eq 0.0) then dAlpha = 0.01*!dtor
E = s3err(X,Tc,Fp,B01,Bf1,B02,Bf2,Rho,Ws,Alpha+dAlpha,R,E_y,Alpha_Dot)
PDER(*,6) = (Fp-F)/dAlpha
;   dF/dR
eta = 1.01
E = s3err(X,Tc,Fp,B01,Bf2,B02,Bf2,Rho,Ws,Alpha,R*eta,E_y,Alpha_Dot)
PDER(*,7) = (Fp-F)/((eta-1.0)*R)
;   dF/dE_y
eta = 1.01
dE_y = (eta - 1.0)*E_y
if (dE_y eq 0.0) then dE_y = 0.01*!dtor
E = s3err(X,Tc,Fp,B01,Bf1,B02,Bf2,Rho,Ws,Alpha,R,E_y+dE_y,Alpha_Dot)
PDER(*,8) = (Fp-F)/dE_y
;   dF/dAlpha_Dot
eta = 1.01
dA_d = (eta  - 1.0)*Alpha_Dot
if (dA_d eq 0.0) then dA_d = 0.001*Ws
E = s3err(X,Tc,Fp,B01,Bf1,B02,Bf2,Rho,Ws,Alpha,R,E_y,Alpha_Dot+dA_d)
PDER(*,9) = (Fp-F)/dA_d
end
```

```
function S3ERR, X,Cts,Trn,B01,Bf1,B02,Bf2,Rho,Ws,Alpha,R,E_y,Alpha_Dot
COMMON Collcom, Coll1, Coll2, Dt
G = 1.0
Nt = n_elements(X)
N = Nt/2
Trn = dblarr(Nt)
Cresp = dblarr(Nt)
Back= dblarr(Nt)
thp = dblarr(Nt)
alp = dblarr(Nt)
; Transform to managable parameters
Ptemp = findgen(N)*Ws*Dt - rho*Ws*Dt
thp(0:N-1) = Ptemp + E_y*Alpha
thp(N:Nt-1) = Ptemp + $
          E_y*(Alpha-Coll2.E_x)
alp(0:N-1) = Alpha + (E_y - Alpha_Dot/Ws)*Ptemp
alp(N:Nt-1) = Alpha +(E_y-Alpha_Dot/Ws)*Ptemp - Coll2.E_x
;alp(0:N-1) = Alpha
;alp(N:Nt-1) = Alpha - Coll2.E_x
; Determine Background Level
Back(0:N-1) = findgen(N)*(Bf1-B01)/N + B01
Back(N:Nt-1) = findgen(N)*(Bf2-B02)/N + B02
; Get XMSSON function
for i=0,N-1 do $
  CResp(i) = xmsson(alp(i),thp(i),0.0,0.0,$
             Coll1.xFOV/2.,Coll1.zFOV/2.)*R*Coll1.Area
```

```
for i=N,Nt-1 do $
  CResp(i) = xmsson(alp(i),thp(i),0.0,0.0,$
             Coll2.xFOV/2.,Coll2.zFOV/2.)*R*Coll2.Area
Trn = Cresp + Back
E = total(((Cts - Trn)^2)/Cts)
return, E
end
```

```
;          R        Attitude Determination Structure
;  ======================Att_Struct=========================
;  N_Mjf     : Number of Major Frames, integer
;  N_Bin     : Number of Bins in Scan, integer
;  Mjf       : Array of Major Frame Numbers, lonarr(n_mjf)
;  Mode      : Timing Mode of HEAO (320,5)
;  Module    : Module Number (3,4,5,6,7)
;  SrcRA     : Source RA (rad)
;  SrcDEC    : Source DEC (rad)
;  SrcName   : Source Name (string)
;  SrcInt    : Source Mean Intensity in This Mode (double)
;  Cts       : Array of Counts for Current Scan (intarr(n_bin))
;  Trn       : Transmission Function from Aspect Solution
;  Y_Asp     : Orientation of Y-axis (RA,DEC) for each bin
;  Z_Asp     : Orientation of Z-axis (RA,DEC) for each bin
;  S_Asp     : Location of the Source in Instrument Coordinates
;              (RA,DEC)
;  Y_Est     : Estimated orientation of Y-axis (RA,DEC) for Peak Bin
;  Z_Est     : Estimated orientation of Z-axis (RA,DEC) for Peak Bin
;  S_Est     : Estimated Location off the Source in Instrument
;              Coordinates (RA,DEC)
;  Bmax      : Bin Where Attitude Estimate Occurs
;  Yfit      : Fit to Scan (double(N_Bin))
;  Alpha     : Estimated Source Angle Off Vertical
;  Fit_Err   : Flag Indicatinf Error in Fitting Process (1=error)
;  Rchi      : Reduced Chi-Squared in Fit
;  Pfit      : Fit Parameters (double(5))
;  Y_Err     : Error in Estimate of Y-axis (RA,DEC) for Peak Bin
;  Z_Err     : Error in Estimate of Z-axis (RA,DEC) for Peak Bin
;  S_Err     : Error in Estimate of Source Location (RA,DEC)
```

Appendix H: Phase Locked Loops

H.1 Phase Detectors

The simplest way to measure the relative phase of two signals is to use a quadrature multiplier. That is, we simply multiply the two signals together, viz.:

$$u_d = u_1(t)u_2(t) \tag{H.1.1}$$

Consider the case where u_1 and u_2 are sinusoidal, viz.:

$$u_1 = A_1 \sin(\theta_1) \tag{H.1.2}$$

$$u_2 = A_2 \cos(\theta_2) \tag{H.1.3}$$

If the phase error, θ_e, is defined as,

$$\theta_e = \theta_1 - \theta_2 \tag{H.1.4}$$

then the phase detector signal, u_d, can be written as follows:

$$u_d = A_1 A_2 \sin(\theta_1)\cos(\theta_1 - \theta_e) \quad \text{(H.1.5a)}$$

$$u_d = A_1 A_2 \sin(\theta_1)\left(\cos(\theta_1)\cos(\theta_e) + \sin(\theta_1)\sin(\theta_e)\right) \quad \text{(H.1.5b)}$$

$$u_d = \frac{A_1 A_2}{2}\left(\sin(2\theta_1)\cos(\theta_e) + (1 - \cos(2\theta_1))\sin(\theta_e)\right) \quad \text{(H.1.5c)}$$

$$u_d = \frac{A_1 A_2}{2}\sin(\theta_e) + \frac{A_1 A_2}{2}\sin(2\theta_1 - \theta_e) \quad \text{(H.1.5d)}$$

The first term of u_d is a steady term proportional to the phase error between u_1 and u_2. The second term is a sine wave at twice the reference frequency. A properly designed loop filter will attenuate signals at twice the reference frequency to reduce this term. The net effect is that the phase detector signal is proportional to the phase error with a small jitter on top of it. If the phase error is small, then the phase detector can be approximated by a linear model, viz.:

$$u_d \cong \frac{A_1 A_2}{2}\theta_e = K_{pd}\theta_e \quad \text{(H.1.6)}$$

H.2 Loop Filters

The three filters considered in this thesis are the constant gain filter, the active lag-lead filter and the proportional plus integral (PI) filter.

H.2.1 Constant Gain Filter

The differential equation governing the constant gain filter is,

$$u_f = K_f u_d \quad \text{(H.2.1a)}$$

In the LaPlace domain this can be represented as,

$$U_f(s) = K_f U_d(s) \quad \text{(H.2.1b)}$$

H.2.2 Active Lag-Lead Filter

The differential equation governing the active lag-lead filter is,

$$u_f + \tau_1 \dot{u}_f = K_f\left(u_d + \tau_2 \dot{u}_d\right) \tag{H.2.2a}$$

In the LaPlace domain this can be represented as,

$$U_f(s) = K_f \frac{1+\tau_2 s}{1+\tau_1 s} U_d(s) \tag{H.2.2b}$$

H.2.3 PI Filter

The differential equation governing the PI filter is,

$$\tau_1 \dot{u}_f = u_d + \tau_2 \dot{u}_d \tag{H.2.3a}$$

In the LaPlace domain this can be represented as,

$$U_f(s) = \frac{1+\tau_2 s}{\tau_1 s} U_d(s) \tag{H.2.3b}$$

H.3 Voltage Controlled Oscillator

The voltage controlled oscillator (VCO) is the local clock that will be used as a time reference. In this case the output of the VCO will be a sine wave. The frequency of the VCO signal is equal to the sum of a constant frequency, called the center frequency, and an offset frequency that is proportional to the input, viz.:

$$\omega_{vco}(t) = \omega_0 + K_{vco} u_f(t) \tag{H.3.1}$$

The phase of the VCO (θ_2), is just the integral of ω_{vco},

$$\theta_2(t) = \int_0^t \omega_{vco}(t)dt + \theta_2(0) \tag{H.3.2a}$$

This can be written in the LaPlace domain as,

$$\Theta_2(s) = \frac{K_{vco}}{s} U_f(s) \tag{H.3.2b}$$

The output of the VCO introduces a nonlinearity into the system, viz.:

$$u_2(t) = \cos(\theta_2(t)) \tag{H.3.3}$$

H.4 General Linearized Equations for the PLL

By using the linear model of the phase detector (H.1.6), a general transfer function for the PLL in the locked state can be derived, viz.:

$$H(s) = \frac{\Theta_2(s)}{\Theta_1(s)} = \frac{K_{vco}K_{pd}F_{lf}(s)}{s + K_{vco}K_{pd}F(s)} F_{pf}(s) \tag{H.4.1a}$$

$$H_e(s) = \frac{\Theta_e(s)}{\Theta_1(s)} = \frac{s}{s + K_{vco}K_{pd}F_{lf}(s)} F_{pf}(s) \tag{H.4.1b}$$

H.5 Simulation Prefilter - Butterworth Bandpass Design

Using the MATLAB rountine 'BUTTER', a butterworth bandpass filter was designed for the x-ray timing simulation. The state-space representation of this filter is given in equation H.5.1.

$$\Phi_{pf} = \begin{bmatrix} 5.1789e-1 & -4.7702e-2 & 7.7451e-1 & -2.4340e-2 \\ 4.7702e-2 & 5.8535e-1 & 2.4340e-2 & 8.0893e-1 \\ -7.7451e-1 & 2.4340e-2 & 6.0481e-1 & 1.2419e-1 \\ -2.4340e-2 & -8.0893e-1 & -1.2419e-2 & 5.8724e-1 \end{bmatrix} \quad \Gamma_{pf} = \begin{bmatrix} 8.5024e-2 \\ 2.6720e-3 \\ -4.3384e-2 \\ -1.3634e-3 \end{bmatrix}$$

$$H_{pf} = \begin{bmatrix} 1.6865e-2 & 5.6051e-1 & 8.6054e-3 & 2.8600e-1 \end{bmatrix} \quad J_{pf} = \begin{bmatrix} 9.4469e-4 \end{bmatrix}$$

(H.5.1)

The frequency response of this filter is shown in Figure H.1.

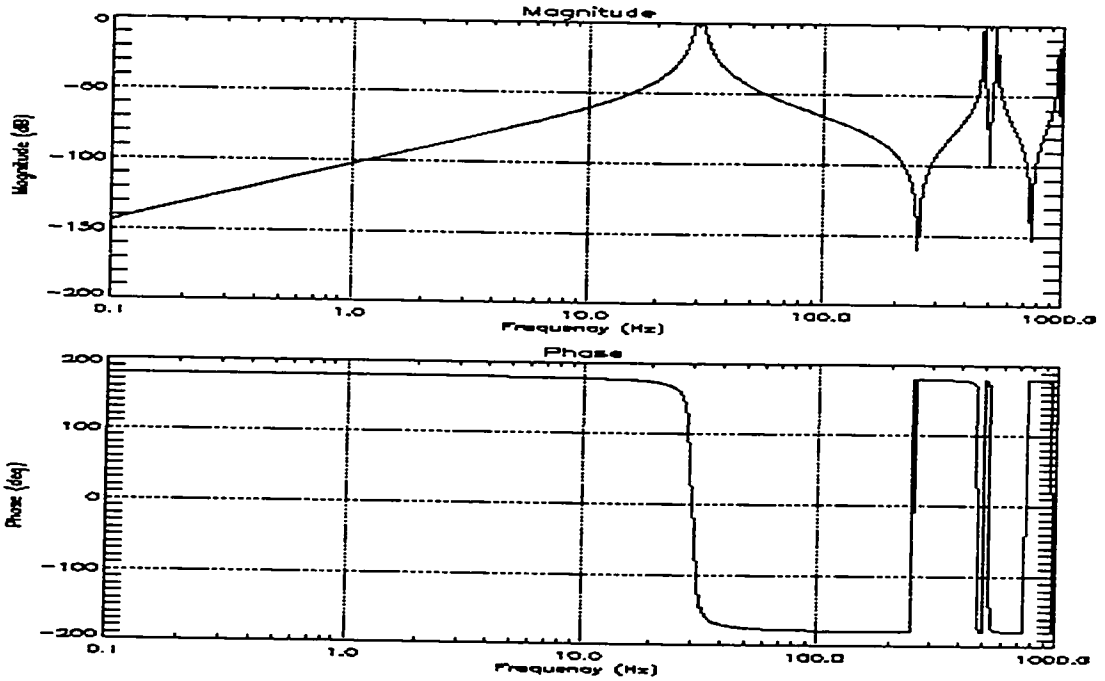

Figure H.1: Prefilter Frequency Response

Appendix I: Phase Locked Loop Simulation - IDL Procedures

```
function pllchyb, N,Floop,Dloop,Kloop,Evco,P0,Ebck,Kd,Mh1,Plcse
; Crab Parameters
Case Plcse of
  'chb2' : begin
           dt = 0.002
           phip = [[8.9521e-1,-2.9327e-2,3.6195e-1,-5.601e-3], S
                [2.9327e-2,9.2916e-1,5.6010e-3,3.6844e-1], S
                [-3.6195e-1,5.6010e-3,9.3087e-1,1.0697e-3], S
                [-5.6010e-3,-3.6844e-1,-1.0697e-3,9.2963e-1]]
           gamp = [[3.4911e-2],[5.4023e-4],[-6.6674e-3],[-1.0317e-4]]
           hp = [1.2053e-2,7.9287e-1,2.3020e-3,1.5142e-1]
           jp = [2.2203e-4]
          end
  'chb5' : begin
           dt = 0.005
           phip = [[4.9296d-1,-7.2029d-2,7.6179d-1,-3.6753d-2], S
                [7.2029d-2,5.8338d-1,3.6753d-2,8.0792d-1], S
                [-7.6179d-1,3.6753d-2,6.1130d-1,1.8753d-2], S
                [-3.6753d-2,-8.0792d-1,-1.8753d-2,5.8776d-1]]
           gamp = [[8.3628d-2],[4.0347d-3],[-4.2671d-2],[-2.0587d-3]]
           hp = [3.8205d-2,8.3905d-1,1.9494d-2,4.2854d-1]
           jp = [2.1401d-3]
          end
  'btt2' : begin
           dt = 0.002
```

```
            phip = [[8.9564d-1,-2.3823d-2,3.6200d-1,-4.5493d-3], $
                 [2.3823d-2,9.2933d-1,4.5493d-3,3.6844d-1], $
                 [-3.6200d-1,4.5493d-3,9.3087d-1,8.6876-4], $
                 [-4.5493e-3,-3.6844d-1,-8.6876d-4,9.2964d-1]]
            gamp = [[3.4919d-2],[4.3883d-4],[-6.6683d-3],[-8.3801d-5]]
            hp = [8.4228d-3,6.8212d-1,1.6084d-3,1.3026d-1]
            jp = [1.5515d-4]
           end
   'btt5' : begin
            dt = 0.005
            phip = [[5.1789d-1,-4.7702d-2,7.7451d-1,-2.4340d-2], $
                 [4.7702d-2,5.8535d-1,2.4340d-2,8.0893d-1], $
                 [-7.7451d-1,2.4340d-2,6.0481d-1,1.2419d-2], $
                 [-2.4340d-2,-8.0893d-1,-1.2419d-2,5.8724d-1]]
            gamp = [[8.5024d-2],[2.6720d-3],[-4.3384d-2],[-1.3634d-3]]
            hp = [1.6865d-2,5.6051d-1,8.6054d-3,2.8600d-1]
            jp = [9.4469d-4]
           end
   else : print,'No Filter Specified'
endcase
h0 = 0.95*2171*Dt/.32
h1 = Mh1*h0*.0905/.95
Tf = .03328
wcrab = 2*!pi/Tf
print, N,Dt,h0,h1
Cdat = gencrab(N,Dt,h0,h1)
t = Cdat(*,0)
u0 = Cdat(*,3) - h0*(1.+ Ebck)
; PLL Design Variables
w0 = (1. + Evco)*2*!dpi/Tf
;  Bode plot of pre-filter
print,'dt = ',dt
w = 10^(findgen(200)/50. - 1.d0)
Bp = dbode_ss(phip,gamp,hp,jp,w,dt)
;  Design active lag loop filter
Ka = 1.d0
pllf_alag, Floop,Dloop,Kloop,Dt,Phif,Gamf,Hf,Jf,Dwh,Dwl,Tl,Bl
K0 = Kloop/Ka
print,'Hold Range = ',Dwh,' Hz'
print,'Lock Range = ',Dwl,' Hz'
print,'Lock Time = ',Tl,' s'
print,'Noise Bandwidth = ',Bl,' Hz'
Fvco = (1.d0 + Evco)/Tf
; Prefilter Data
u1 = dblarr(N)
xlo = [0.,0.,0.,0.]
for i=1L, long(N)-1L do begin
  ; Prefilter - Band pass
 u1(i) = filter_ss (xln,xlo,[u0(i-1)],phip,gamp,hp,jp)
 xlo = xln
endfor
; Simulate Phase Locked Loop
R = pllsim(u1,Kd,Phif,Gamf,Hf,Jf,Dt,Fvco,K0,P0)
X = fltarr(N,11)
```

```
X(*,1,3) = Cdat
X(*,4) = t1
X(*,5,5) = R
X(*,1,1) = X(*,1) - X(*,5)
return, X
end
```

```
function gencrab, N, dt, h0, h1
; X(*,0) = time of measurement
; X(*,1) = clean signal phase (rad)
; X(*,2) = clean signal
; X(*,3) = noisy signal
x = dblarr(N,4)
x(*,0) = findgen(N)*dt
; Fill Crab Array
Nci = 1000L
cc = filcrab(Nci,dt,h0,h1)
print,'gencrab = ',h0,h1
; Interpolate to Find Count Rate
t = x(*,0) - long(x(*,0)/.03328)*.03328
t = t*Nci/.03328
t1 = long(t)
t2 = t1 + 1L
x(*,2) = cc(t1) + (cc(t2)-cc(t1))*(t - t1)
x(*,1) = x(*,0)*2.*!dpi/.03328
X(*,3) = poidev(X(*,2))
return, x
end
```

```
pro PLLF_ALAG, Fn,Damp,K,Dt,Phi,Gam,H,J,Dwh,Dwl,Tl,Bl
wn = 2.d0*!dpi*Fn
Ka = 1.0
tau2 = 2*Damp/wn - 1./K
tau1 = K/wn^2
print,tau1,tau2,damp,wn
if ((tau1 gt 0.0) and (tau2 gt 0.0)) then begin
  c1ss_alag, Ka,tau1,tau2,A,B,C,D
  c2d_ss, A,B,C,D,Phi,Gam,H,J,Dt,'prewarp',wn
endif else S
  print,'Improper Loop Specifications'
; Compute Loop Performance Paramters
Dwh = K/(2.d0*!dpi)
Dwl = K*(tau2/tau1)/(2.d0*!dpi)
Tl = 1.d0/Fn
Bl = (Fn/2.d0)*(Damp + 0.25/Damp)
end
```

```
function filter_ss, x,x0,u,phi,gam,h,j
; x(k+1) = phi*x(k) + gam*u(k)
; y(k) = h*x(k) + j*u(k)
x = x0#phi + u#gam
y = x#h + u#j
return, y
```

```
end
```

```
function pllsim, U1,Kd,Phif,Gamf,Hf,Jf,Dt,Fvco,K0,P0
; PLL Design Variables
w0 = Fvco*2.d0*!dpi
; Set Initial Conditions
N = long(n_elements(u1))
ud = dblarr(N)
uf = dblarr(N)
wv = dblarr(N)
th2= dblarr(N)
u2 = dblarr(N)
ud(0) = 0.0
uf(0) = 0.0
wv(0) = w0
th2(0) = P0
u2(0) = cos(th2(0))
xfo = [0.0,0.0]
; PLL Main Loop
for i=1L, long(N)-1L do begin
  ; Phase Detector
  ud(i) = Kd*u1(i-1)*u2(i-1)
  ; Loop Filter
  uf(i) = filter_ss (xfn,xfo,[ud(i-1)],phif,gamf,hf,jf)
  xfo = xfn
  ; VCO
  wv(i) = w0 + K0*uf(i)
  if (wv(i) lt 0.0) then wv(i) = 0.0
  th2(i) = th2(i-1) + dt*wv(i)
  u2(i) = cos(th2(i))
endfor
; Fill final time step
wv(N-1L) = w0 + K0*uf(N-1L)
ud(N-1L) = Kd*u1(N-1L)*u2(N-1L)
X = fltarr(N,5)
X(*,0) = ud
X(*,1) = uf
X(*,2) = wv
X(*,3) = th2
X(*,4) = u2
return, X
end
```

References

Aluminum Association. Aluminum Brazing Handbook, 4th ed. Washington, D.C.: Aluminum Association, 1990.

Best, Roland E. Phase Locked Loops: Theory, Design and Applications. New York: McGraw Hill, Inc., 1993.

Bevington, Philip R. and D. Keith Robinson. Data Reduction and Error Analysis for the Physical Sciences. New York: McGraw Hill, Inc., 1992.

Black, Harold D. "Early Development of Transit, The Navy Navigation Satellite System." Journal of Guidance, Navigation and Control. 13:577-585, 1990.

Blanchard, Alain. Phase-Locked Loops: Application to Coherent Receiver Design. New York: John Wiley & Sons, Inc., 1976.

Bradt, Hale V.D., et al. "X-ray Astronomy Missions". Annual Review of Astronomy and Astrophysics. 30:391-427, 1992.

Byard, Kevin. "On Self-Supporting Coded Aperture Arrays." Nuclear Instruments and Methods in Physics Research. A322:97-100, 1992.

Cohen, Clark E. et al. "Space Flight Tests of Attitude Determination Using GPS." International Journal of Satellite Communications. 12:427-33, 1994.

Crerie, Jeffrey. Phase-Lock roll Control of Inertially Pointing Spacecraft. Unpublished PhD Thesis, Stanford University, Stanford, Ca., 1993.

Dicke, R.H. "Scatter-Hole Cameras for X-rays and Gamma Rays." Astrophysical Journal. 153:L101-L106, 1968.

Fabian, A.C. and X Barcons. "The Origin of the X-ray Background". Annual Review of Astronomy and Astrophysics. 30:429-456, 1992.

Fenimore, E. E. and T. M. Cannon. "Coded Aperture Imaging with Uniformly Redundant Arrays." Applied Optics. 17:337-347, 1978.

Forman, W. et al. "The Fourth Uhuru Catalog of X-ray Sources." The Astrophysical Journal Supplement Series. 38:357-412, 1978.

Gardner, Floyd M. Phaselock Techniques. New York: John Wiley & Sons, 1966.

Gardner, Floyd M. Phaselock Techniques. New York: John Wiley & Sons, 1979.

Hammersley, Andrew et al. "Reconstruction of Images from a Coded-Aperture Box Camera." Nuclear Instruments and Methods in Physics Research. A311:585-594, 1992.

Hanson, John E. "USA Structure Test Program." Internal report. Astrogravity Note #17. Stanford Linear Accelerator Center, Stanford, Ca.

Hanson, John E. "USA Dip Brazing Manufacturing Qualification." Internal report. Astrogravity Note #18. Stanford Linear Accelerator Center, Stanford, Ca.

Hanson, John E. "USA Structure Quality Assurance Testing." Internal report. Astrogravity Note #19. Stanford Linear Accelerator Center, Stanford, Ca.

Hanson, John E. "USA Pylon Static Load Test." Internal report. Astrogravity Note #20. Stanford Linear Accelerator Center, Stanford, Ca.

Harnden, F. R. and F.D. Seward. "Einstein Observations and the Crab Nebula Pulsar." The Astrophysical Journal. 283:279-285, 1984.

Hoech, Robert, et al. "Design, Capabilities and Performance of a Miniaturized Airborne GPS Receiver for Space Applications." Paper presented at IEEE 1994 Position Location and Navigation Symposium. New York, NY. 1994.

Kau, S.P. et al. "Autonomous Satellite Orbit Navigation Using Known and Unknown Earth Landmarks." Paper presented at AIAA Guidance and Control Conference. Boston, Mass. Aug 20-22, 1975.

Massen, Robert. "Sensors with Coded Apertures." Journal of Physics E: Scientific Instruments. 20:595-600, 1987.

The Math Works, Inc. Control System Toolbox For Use with MATLAB. Natick, Mass.: The Math Works, Inc. 1992.

The Math Works, Inc. MATLAB Reference Guide. Natick, Ma.: The Math Works, Inc. 1992.

Mendel, Jerry M. Maximum Likelihood Deconvolution. New York: Springer-Verlag, 1990.

Ponman, Trevor et al. "Error Analysis for a Noncyclic Imaging System." Nuclear Instruments and Methods in Physics Research. A262:419-429, 1987.

Research Systems, Inc. IDL User's Guide. Boulder, Co.: Research Systems, Inc. 1994.

Research Systems, Inc. IDL Reference Guide. Boulder, Co.: Research Systems, Inc. 1994.

Skinner, G.K. "Imaging with Coded-Aperture Masks." Nuclear Instruments and Methods in Physics Research. A221:33-40, 1984.

Staff of the Space Department, Johns Hopkins University APL, and Staff of the Guidance and Control Laboratory, Stanford University. "A Satellite Freed of all but Gravitational Forces: 'TRIAD I'." Journal of Spacecraft and Rockets. 11: 637-644, 1974.

Stanley, William D., et al. Digital Signal Processing. Reston, Va.: Reston Publishing Co., Inc., 1984.

Taylor, Fred J. Digital Filter Design Handbook. New York: Marcel Dekker, Inc., 1983.

Van Bezooijen, Roelof W.H. "Star Sensors for Autonomous Attitude Control and Navigation." Optical Technologies in Aerospace Sensing, 1992.

Vessot, Robert F.C. "Experimental Techniques with Highly Stable Clocks." Paper presented at XIVth Moriond Workshop on Dark Matters in Cosmology, Clocks and tests of Fundamental Laws. Villars-Sur-Ollon, Switzerland. January 21, 1995.

Wen, Han. "Determining Dead Time." Internal report. Astrogravity Note #14. Stanford Linear Accelerator Center, Stanford, Ca.

Wertz, James R., ed. Spacecraft Attitude Determination and Control. Boston, Ma: Kluwer Academic Publishers, 1978.

White, Robert L. et al. "Autonomous Satellite Navigation Using Observations of Starlight Atmospheric Refraction." Navigation. 32:317-333, 1985-86.

White, R. L. et al. "Use of Known Landmarks for Satellite Navigation" Paper presented at AIAA Guidance and Control Conference, Boston, Mass. Aug 20-22, 1975.

White, N.E. et al. "The Properties of X-ray Binaries." In X-ray Binaries, edited by Walter H.G. Lewin et al. Cambridge, UK: Cambridge University Press, 1995:1-57.

Wood, K.S. et al. "The HEAO A-1 X-ray Source Catalog". The Astrophysical Journal Supplement Series. 56: 507-649, 1984.

Wood, K.S. "Navigation Studies Utilizing the NRL-801 Experiment and the ARGOS Satellite." Preprint, 1993.